ORNL/TM-2022/2428

Reactor Physics Simulations of the High Flux Isotope Reactor Permanent Beryllium Reflector Number 5 Design

David Chandler
Jorge Navarro

July 2022

DOCUMENT AVAILABILITY

Reports produced after January 1, 1996, are generally available free via US Department of Energy (DOE) SciTech Connect.

Website www.osti.gov

Reports produced before January 1, 1996, may be purchased by members of the public from the following source:

National Technical Information Service
5285 Port Royal Road
Springfield, VA 22161
Telephone 703-605-6000 (1-800-553-6847)
TDD 703-487-4639
Fax 703-605-6900
E-mail info@ntis.gov
Website http://classic.ntis.gov/

Reports are available to DOE employees, DOE contractors, Energy Technology Data Exchange representatives, and International Nuclear Information System representatives from the following source:

Office of Scientific and Technical Information
PO Box 62
Oak Ridge, TN 37831
Telephone 865-576-8401
Fax 865-576-5728
E-mail reports@osti.gov
Website https://www.osti.gov/

This report was prepared as an account of work sponsored by an agency of the United States Government. Neither the United States Government nor any agency thereof, nor any of their employees, makes any warranty, express or implied, or assumes any legal liability or responsibility for the accuracy, completeness, or usefulness of any information, apparatus, product, or process disclosed, or represents that its use would not infringe privately owned rights. Reference herein to any specific commercial product, process, or service by trade name, trademark, manufacturer, or otherwise, does not necessarily constitute or imply its endorsement, recommendation, or favoring by the United States Government or any agency thereof. The views and opinions of authors expressed herein do not necessarily state or reflect those of the United States Government or any agency thereof.

ORNL/TM-2022/2428

Nuclear Energy and Fuel Cycle Division

REACTOR PHYSICS SIMULATIONS OF THE HIGH FLUX ISOTOPE REACTOR PERMANENT BERYLLIUM REFLECTOR NUMBER 5 DESIGN

David Chandler
Jorge Navarro

July 2022

Prepared by
OAK RIDGE NATIONAL LABORATORY
Oak Ridge, TN 37831-6283
managed by
UT-BATTELLE LLC
for the
US DEPARTMENT OF ENERGY
under contract DE-AC05-00OR22725

CONTENTS

Section **Page**

LIST OF FIGURES

LIST OF TABLES

Table **Page**

ABSTRACT

This study evaluates reactor physics aspects of the proposed High Flux Isotope Reactor (HFIR) permanent beryllium reflector number 5 design. HFIR is a pressurized, light water–cooled, and beryllium reflected research reactor that operates at 85 MW for cycle lengths of approximately 24 to 26 days. A new permanent reflector design is highly desirable for increased versatility in irradiation experiments, to arrange the vertical experiment facilities (VXFs) to minimize their impact on neutron scattering if loaded with neutron-absorbing experiments, to enhance reflector thermal-structural-hydraulic performance, and to simplify the complex fabrication process. The current number 4 and concept number 5 reflectors have 22 and 28 VXFs, respectively, and are modeled and analyzed in this study with the MCNP5 and SCALE 6.1.3 nuclear simulation codes.

A high-fidelity model of the current reflector design was developed, with a typical configuration loaded with no irradiation experiments (i.e., *experimentless*), including water and stainless steel (SST) liners in the small VXFs and dummy Be plugs in the large VXFs. A finer reflector cell–based mesh was developed, and the coolant hole features were explicitly modeled. The newly designed concept reflector, with modified VXF and coolant hole layouts, was then generated and modeled with bounding experimentless VXF loadings (e.g., Be plugs, Al plugs, water/SST liners). Core safety and performance physics metrics were calculated for the concept reflector design and compared to those for the current reflector design. The concept reflector itself has no adverse impacts on reactor physics safety metrics (e.g., core fission rate distribution, shutdown margin) or performance (e.g., cycle length, fluxes to experiments); however, the choice of the VXF contents can have small positive or adverse impacts on performance. The concept design—with Be plugs in five inner small and all large VXFs, and the remainder of the VXFs containing water/SST liners—yields physics results equivalent to those of the current reflector number 4 reference case.

A maximum heat deposition rate of 7.38 W/cm^3 was calculated for use in follow-on thermal-structural-hydraulic evaluations. For the various configurations analyzed, a peak fast ($E_n > 1$ MeV) fluence of 1.22×10^{22} n/cm^2 was predicted. Maximum ^{3}H, ^{3}He, ^{4}He, and ^{6}Li concentrations of 0.25 mg/cm^3, 1.11 μg/cm^3, 2.40 mg/cm^3 (0.29 at. %), and 3.03 μg/cm^3 were respectively estimated assuming a 279,000 MWd end of life, 85 MW operations, 25 day irradiation cycles, and 25 day decay periods.

1. INTRODUCTION AND PURPOSE OF STUDY

The purpose of this study is to evaluate reactor physics aspects of the proposed High Flux Isotope Reactor (HFIR) permanent beryllium (PB) reflector number 5 design, which is typically referred to as the *concept design* throughout this report. A new PB reflector design is highly desired for several reasons, primarily the following:

i. to increase the versatility of the reflector for irradiation experiments,
ii. to increase the potential heat source PuO_2 production capability,
iii. to arrange the vertical experiment facilities (VXF) in a layout to maintain or increase neutron fluxes down the horizontal beam tubes for neutron scattering,
iv. to enhance its thermal-structural-hydraulic performance, and
v. to simplify the fabrication/machining process, where possible, to reduce machining time, cost, and associated risk.

The current and concept PB reflector designs are illustrated in Figure 1.1 and Figure 1.2, respectively. The primary differences between the two designs are the number and layout of the VXFs and coolant holes. The concept design has 28 VXFs, and the current design has 22. More details regarding HFIR, the current reflector design, the concept reflector design, and the purpose of this study are provided in Sections 1.1, 1.2, 1.3, and 1.4. Study assumptions, calculation methods, analyses, and conclusions are documented in Sections 2, 3, 4, and 5.

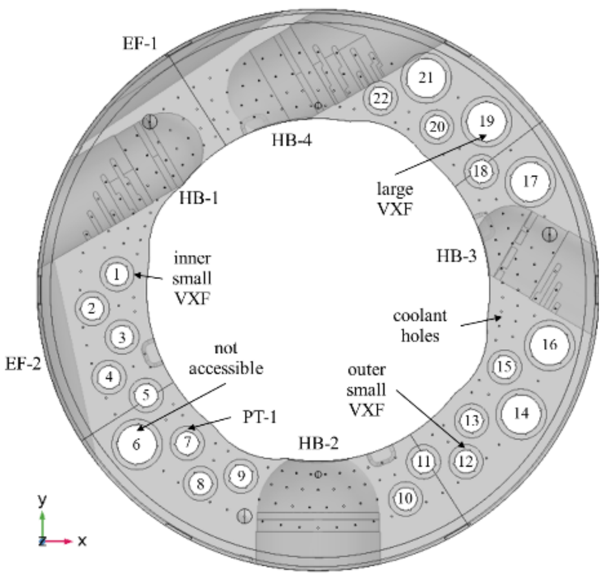

Figure 1.1. Current PB reflector no. 4 design (Chandler 2019).

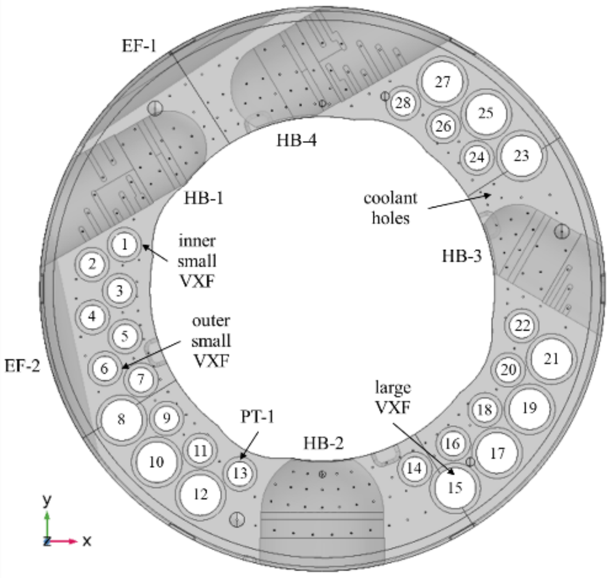

Figure 1.2. Concept PB reflector no. 5 design (Chandler 2019).

1.1 HIGH FLUX ISOTOPE REACTOR DESCRIPTION

HFIR is a US Department of Energy (DOE) Office of Science research reactor that is operated at Oak Ridge National Laboratory. It is a pressurized, light water–cooled and moderated reactor that operates at a steady-state thermal power of 85 MW for cycle lengths of approximately 24 to 26 days. HFIR is a versatile, high-performance reactor with multiple scientific missions and capabilities, including cold and thermal neutron scattering research, isotope production, fuel and material irradiation research, neutron activation analysis, nuclear nonproliferation research, and nuclear physics research.

The core assembly consists of a series of concentric annular regions—each approximately 24 in. (60.96 cm) in height—including a flux trap target region, an inner fuel element (IFE), an outer fuel element (OFE), a control element region, and a Be reflector region. The core is surrounded by light water and is contained within a steel pressure vessel, which itself is in a pool of water. Figure 1.3 illustrates the core assembly model of HFIR on the core horizontal midplane.

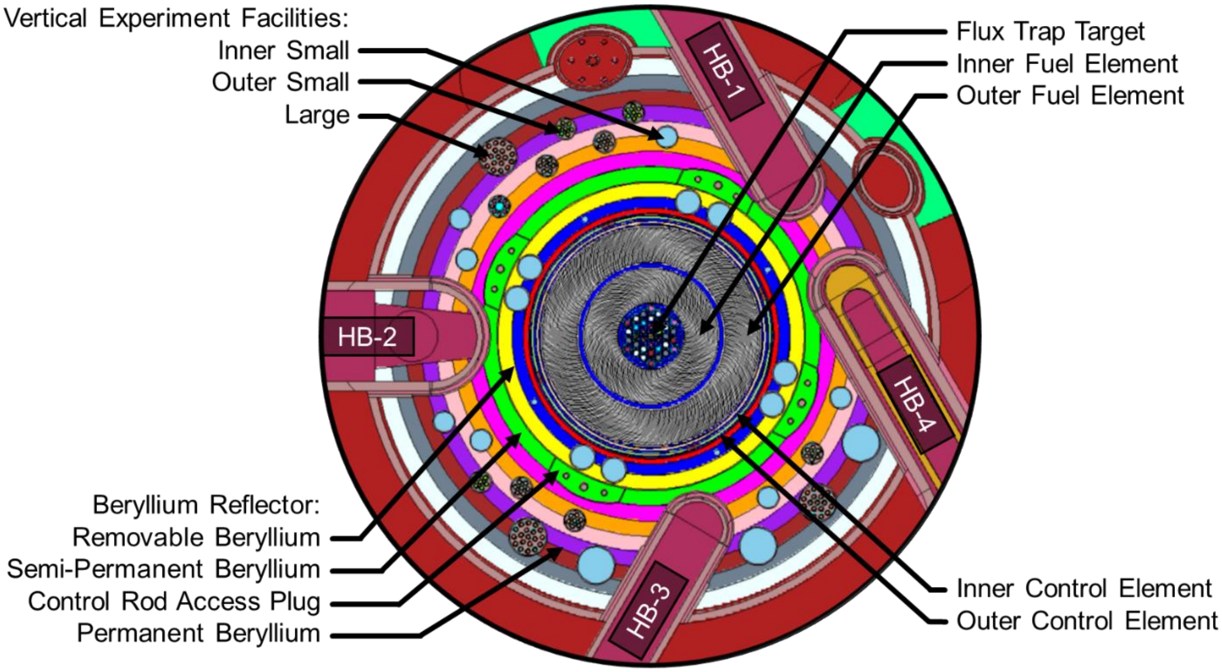

Figure 1.3. HFIR core assembly model with components labeled.

The central flux trap target region is surrounded by the fuel assembly. This design promotes neutron leakage from the fuel into the flux trap, and thus the highest accessible fluxes exist in the flux trap for materials irradiation and isotope production purposes. The flux trap contains 37 vertical irradiation positions, including 30 interior positions, 6 peripheral positions, and a hydraulic tube.

The fuel assembly consists of an integral two element assembly, where the inner element is nested within the outer element. The inner and outer fuel elements are loaded with 171 and 369 involute-shaped fuel plates, respectively, and each fuel plate contains a fuel region and an Al filler region encapsulated in Al clad. A total of 2.6 and 6.8 kg of ^{235}U in the form of U_3O_8-Al dispersion highly enriched uranium fuel is loaded into the inner and outer elements, respectively. The fuel is contoured along the arc of the involute to minimize the peak to average power density ratio. Additionally, about 2.7 g of ^{10}B is loaded in the inner element to reduce radial edge power peaking and for reactivity hold-down purposes.

Two concentric control elements are located in the small water annulus between the fuel assembly and the Be reflector. The inner control element consists of four control plates welded together that are used for reactivity control. The outer control element consists of four separate safety/control plates that are used for reactivity control and fast scram purposes. Each of the eight plates contains Al, Ta-Al, and Eu_2O_3-Al regions, which have trivial, moderate, and strong neutron absorption capabilities, respectively. The control elements are axially withdrawn during the cycle by moving the absorber regions away from the core horizontal midplane to compensate for reactivity change caused by fuel depletion, fission product generation, and boron depletion. The inner and outer control elements are withdrawn downward and upward, respectively, during the cycle.

The large Be reflector is subdivided into removable, semi-permanent, and permanent reflector regions, which are named based on the frequency at which they are replaced due to radiation damage. The removable reflector is closest to the core centerline and contains eight large and four small irradiation facilities. The region between the removable and permanent reflector contains four semi-permanent reflector quadrants and four control rod access plugs. Each control rod access plug houses two small irradiation facilities. Section 1.2 provides a detailed description of the PB reflector.

Refer to the reports by Chandler et al. (2020) and Ilas et al. (2015) for more detailed descriptions of HFIR.

1.2 PERMANENT BERYLLIUM REFLECTOR DESCRIPTION

The PB reflector is contained in the reactor vessel radially outward of the removable and semi-permanent reflectors and serves multiple purposes. These purposes include, but are not limited to, moderating/reflecting neutrons for increased core reactivity, housing in-vessel experiment facilities, and moderating neutrons for enhanced irradiation and neutron scattering experiments. The Be reflector is described in Section 4.2.2.3, “Beryllium Reflector,” and Section 3.9.5.1 “Design arrangements,” of the Safety Analysis Report (SAR), and the reflector design criteria and requirements are discussed in Section 4.2.3.2.4, “Reflector,” of that document (SAR 2021).

The PB reflector’s inner diameter, outer diameter, and height are 26.25, 43.00, and 24.00 in., respectively. It is supported underneath by the reflector pedestal that is bolted to the reflector support and sleeve assembly, which itself is bolted to the lower part of the pressure vessel. The reflector is clamped between the reflector pedestal and outer shroud by external tie plates. The outer shroud is located above the reflector and is designed to provide proper distribution of coolant flow to the reflector.

Four horizontal beam (HB-1, -2, -3, and -4) tubes penetrate the PB reflector and terminate at instruments in the beam room and guide hall, where thermal and cold neutron scattering experiments are performed. Two slant engineering facilities (EF-1 and EF-2) pierce the outer radial edge of the reflector and extend downward at an angle of 41°. Two pneumatic tubes, PT-1 and PT-2, located in the reflector are used for neutron activation analysis activities. PT-1 is in inner small VXF-7, and its piping system extending above the beryllium reflector is oriented such that it is directly above large VXF-6, rendering it unusable. PT-2 is located in EF-2.

VXFs accommodate irradiation targets for fuels/materials irradiation and isotope production activities. The current PB reflector is penetrated by 22 VXFs that are located concentric with the core on three circles of radii. Sixteen of the VXFs are small VXFs and have an outer diameter of 1.75 in. Eleven small VXFs are located on the inner concentric ring with an approximate 30.88 in. diameter and are referred to as *inner small VXFs*. The remaining five small VXFs, referred to as *outer small VXFs*, are located on a concentric ring with an approximate 34.69 in. diameter. Six large VXFs, each with an outer diameter of 3.00 in., are located on the outermost concentric ring with an approximate 36.44 in. diameter. The small and large VXFs have Al liners with inner diameters of about 1.58 and 2.83 in., respectively. The angle of separation between adjacent VXFs on the same bolt circle is 18°.

The permanent reflector is cooled by water that flows axially downward through ~0.13 in. diameter holes and grooves. The cooling holes are located on four bolt circles concentric with the core, each containing holes spaced on 4.5° intervals, except where they would interfere with experiment facilities. Where the cooling holes intersect beam tube cut-outs, Al liners are present to direct the flow around the periphery of the cut-outs. The bolt circle diameters for the four concentric circles are about 28.25, 30.61, 33.32, and 36.44 in. There are 58, 47, 36, and 57 (198 total) coolant holes located on the four concentric circles from the innermost to outermost circles, respectively. There are 83 cooling grooves cut into the walls of the 22 VXFs, which correspond roughly with the array of cooling holes. The inner small, outer small, and large VXF hole walls have 4, 3, and 4 grooves cut into them, respectively ($4 \times 11 + 3 \times 5 + 4 \times 6 = 83$).

The permanent reflector is replaced when necessary due to radiation damage, but due to its location with respect to the core and lower fast neutron flux with respect to other beryllium components, it is replaced less often than the removable reflector, semi-PB reflector, and the control rod access plugs. Per [SAR, 2021] Section 4.5.4, “Component Lifetimes,” the PB reflector has an approximate lifetime of 279 GWd (~131–132 cycles consisting of 25 effective full power days operating at 85 MW). The permanent reflector was upgraded following the October 2000 planned shutdown under design change memo HFIR-197M-1 (DCM 2002) to accommodate larger beam tubes and to remove two engineering slant facility tubes (EF-3 and EF-4 adjacent to HB-2). The in-vessel diameters of HB-1 and HB-3 were unchanged, but the diameters of HB-2 and HB-4 were increased for enhanced performance and to incorporate the cold source within HB-4. HFIR was restarted in December 2001; however, HB-2 and HB-4 were not installed into the reflector until 2002 and 2006, respectively.

1.3 CONCEPT BERYLLIUM REFLECTOR DESIGN DESCRIPTION

The basis for acceptance of the new reflector design is a configuration with no unique irradiation experiments (i.e., *experimentless*); however, design studies considering ^{238}Pu production targets were performed by Chandler et al. (2019) to optimize the reflector design for ^{238}Pu production while considering a set of predefined design and performance constraints. The two primary performance constraints, considering ^{238}Pu targets, included a maximum cycle length reduction of 12 hours and a maximum beam tube flux degradation of 5% (e.g., reduced cold/thermal flux and increased fast flux). The concept reflector was designed to provide cycle lengths and beam tube fluxes that are equivalent to or better than the current reflector design when considering reflectors unoccupied by experiments.

The neutronics studies performed by Chandler et al. (2019) considered ^{238}Pu production targets to optimize the VXF layout for ^{238}Pu production while ensuring the two performance constraints were met. The studies primarily included heat source PuO_2 production estimates, cycle length reduction estimates, and beam tube flux sensitivity assessments. Heat source PuO_2 production studies were performed to estimate potential yield increases with respect to the number of VXFs, the number of targets per VXF, and the feed material form (cermet or oxide). Sensitivity of the target efficiency and product quality to the number of VXFs and feed material form was also studied in the production assessment. Cycle length reduction calculations were performed for several cases involving various VXF layouts, number of VXFs loaded with targets, and material type. Beam tube flux sensitivity studies were performed in parallel with the production and cycle length studies to help guide the design. Perturbations to the VXF layout, proximity of the VXFs to their neighboring beam tubes, and VXF content (e.g., water/SST liners, Be plugs, cermet targets, or oxide targets) were made to determine optimal configurations that would not violate the 5% beam tube flux degradation constraint.

The location of the VXFs with respect to the beam tubes were selected to minimize their impact to the beamline fluxes. The concept design beamline fluxes will be equivalent to or better than those of the existing reflector design. Experiments in VXFs adjacent to HB-2 and HB-3 may have small-to-negligible impacts on their beamline fluxes, but the VXF layout of the concept reflector was designed to minimize the impact to beam tube fluxes even if they are filled with neutron absorbing targets. The VXF layout of the concept design is more optimized than the existing design when considering an experimentless reflector or one loaded with irradiation experiment targets.

Detailed 3D COMSOL Multiphysics (COMSOL 2017) thermal-structural studies were also performed in Chandler et al. (2019) to optimize the coolant hole layout and other features to significantly improve the thermal-structural performance of the reflector relative to the current design. Specifically, improvements with respect to (1) reducing features causing stress risers (e.g., thin walls of Be between hollow features) and (2) improving the thermal stress distribution were made.

The PB reflector concept design was developed by carefully considering HFIR design and performance constraints and requirements. The total number of VXFs increases from 22 (current design) to 28 (concept design); 15 are inner small VXFs (11 in current design), three are outer small VXFs (five in current design), and 10 are large VXFs (six in current design). The VXFs are located concentric with the core on three circles, and the inner small VXF bolt circle diameter is the same as that of the existing design; the outer small VXF and outer large VXF bolt circle diameters are slightly greater than those of the existing design to enhance the thermal-structural-hydraulic performance. The VXF hole diameters are slightly increased with respect to the current reflector because the coolant grooves are being moved from the periphery of the VXF holes in the Be material to the periphery of the Al liners, thereby reducing Be machining processes and maintaining the same VXF liner inner diameters as the current design, and thus the same VXF experiment dimensions. The angle of separation between adjacent VXFs on the same bolt circle is 13.1°.

The concept reflector is cooled by water that flows axially downward through ~0.13 in. diameter holes in the beryllium and grooves machined in the aluminum VXF liners. The coolant holes are located on four bolt circles that are concentric with the core and spaced evenly between the permanent reflector’s inner and outer diameters. The coolant holes use the same 4.5° spacing along the bolt circles as the current design. The bolt circle diameters of the first three circles are unchanged from the current design, but the last circle diameter was increased by a little more than an inch. The four diameters were selected to subdivide the permanent reflector into five radial regions with equal heat deposition based on the preliminary heat deposition calculations documented by Chandler et al. (2019). Also, it was desired to move the outermost coolant holes radially outward relative to their diameter in the current reflector to enhance the thermal-structural-hydraulic performance of the reflector. As illustrated in Fig. 7 in the report by Chandler et al. (2019), COMSOL thermal-structural calculations indicated that the inner region of the reflector is being overcooled, and the outer region is being undercooled—thus causing undesired temperature and stress distributions across the reflector. There are 53, 47, 36, and 46 (182 total) coolant holes located on the four concentric circles from the innermost to outermost circles, respectively. Currently, it is anticipated that there will be 3 and 5 grooves cut into the small and large VXF liners, respectively, for a total of 104 grooves ($3\times18 + 5\times10 = 104$).

1.4 PURPOSE AND SCOPE OF STUDY

The purpose of this study is to evaluate pertinent safety and performance physics aspects of the concept reflector design and to ensure its operations are enveloped by the HFIR SAR and pertinent design criteria. The concept reflector design is to be analyzed and approved assuming the reflector is unoccupied by experiments. Upon acceptance of the concept reflector and its subsequent insertion into the reactor vessel, experiments will be qualified, as necessary, via formal safety basis calculations and experiment authorization and safety-related processes. However, it is important to note that most safety analyses performed on experiments inserted into the current reflector will still be bounded if inserted into the concept reflector. Also, the new reflector design will have no impact on irradiation targets qualified for irradiation in the flux trap region because, as shown in Section 4.3, the reflector design changes have no impact on the flux trap fluxes.

A direct, one-to-one comparison between the current and concept designs cannot be performed for all physics parameters because the physics are highly dependent on the contents in the VXFs. The approach taken includes developing a reference case with a high-fidelity model of the current reflector design and comparing its results to those for the concept design with bounding experimentless VXF loadings (e.g., Be plugs, water/SST liners, Al plugs). The goal of this evaluation is to prove that the only physics differences between the two designs arise from the contents in the VXFs, which is a decision made by the Research Reactors Division (RRD) personnel who operate HFIR, and that the concept PB no. 5 design itself has no impact on physics performance.

Beginning-of-cycle (BOC) and end-of-cycle (EOC) calculations are performed to bound typical HFIR cycle conditions, and various VXF loadings are modeled to bound potential, hypothetical configurations without specific experiments (e.g., ^{238}Pu production targets, ^{252}Cf production targets, materials research targets) loaded into the permanent reflector VXFs. The calculations in this report assess Be reflector physics (e.g., heat generation rates, neutron fluxes, cross sections, reaction rates, gas and poison buildup, decay heat), core physics (e.g., reactivity, fission rate distributions, absorption rates by region), and performance physics (e.g., neutron flux distributions). Details regarding the matrix of cases analyzed and the results evaluated are detailed in Section 3 and 4 of this report.

2. STUDY ASSUMPTIONS

Final design drawings for the concept reflector no. 5 and mating components were incomplete at the time this study was being performed. Therefore, some assumptions on the components' design were necessary to complete this study. The modeling assumptions made in this study and the corresponding justifications are provided below.

Assumption 1:

> At the time this study was performed, the concept design drawings were not complete. Therefore, the check print drawings were used. It is assumed that these drawings accurately represent the data required for this study.

Justification of Assumption 1:

> It is currently anticipated that the final drawings will be revisions to the current reflector design drawings. The design is not expected to change; however, small changes to the drawings will likely not affect the models, evaluations, and results documented in this report. Any changes made to the design will be communicated to the preparer of this report to assess whether the calculations remain valid or require revision.

Assumption 2:

> Coolant grooves run down the length of the Be in the current reflector design VXF holes. It is assumed that these grooves will be removed in the concept design and moved to the VXF Al liners (see Section 1.3).

Justification of Assumption 2:

> As discussed in Section 1.3, coolant grooves will be machined down the length of the Al VXF liners rather than down the radius of the Be metal to reduce the number of stress riser features, to reduce the fabrication complexity, and consequently reduce the cost of the machining work and risk associated with the task. No drawings or sketches have been generated for the concept design VXF liners, so assumptions must be made with regard to their geometry (see Assumption 3).

Assumption 3:

> It is assumed that the inner radius of the concept design VXF liners are the same as those in the current design, and the outer radius is assumed to be the same as the VXF hole radius. It is also assumed that each small VXF (inner and outer) liner will have three grooves, and each large VXF liner will have five grooves. Each groove is assumed to have the same dimensions as the grooves cut down the axial length of the Be holes in the current design.

Justification of Assumption 3:

> No drawings or sketches have been generated for the concept design VXF liners. Thus, assumptions must be made regarding the geometry of the liners. Per Section 1.3, the volume available in the small and large VXFs for experiments is to be conserved with respect to the current reflector design; therefore, the inner radius of the current and concept VXF liners must be equal. The outer radius of the concept design VXF is assumed to be equal to the hole radius because the liners are tightly fit into the hole. Three and five grooves of the same dimensions as those for the current design are assumed for the small and large VXFs, respectively, based on communication with the thermal-structural engineer and preliminary thermal-structural calculations. The grooves are modeled in MCNP as small annular gaps between the liner and Be by conserving the volumes of the materials. Small changes to these assumptions will have trivial impacts on the evaluations performed in this calculation.

Assumption 4:

It is assumed that small changes to the coolant holes and grooves will have trivial impacts on the evaluations performed in this calculation. Changes include the number, layout, and dimensions.

Justification of Assumption 4:

Small changes to the coolant holes/grooves (number, layout, and/or dimensions) will have trivial impacts to the evaluations performed in this calculation because they are not large volume regions of water. This study is the first in which coolant holes are explicitly modeled in the PB reflector. In the past, the water coolant was homogenized with the Be material, which is a valid modeling approximation. Small changes to the coolant holes/grooves could occur during or following the thermal-structural-hydraulic safety evaluation, resulting in more optimal thermal and stress distributions. The approach taken to bound the reference case (current design) with various hypothetical VXF loadings (concept design with perturbed loadings) will still be bounding if small changes are made to the layout and number of the coolant holes/grooves.

Assumption 5:

The inner and outer radii of the SST liners modeled in the large VXFs, for the case later referred to as the *water/SST liner case*, are assumed based on the dimensions of the small VXF liner dimensions. The same small VXF SST liner thickness and Δr between the Al liners and SST liners are assumed.

Justification of Assumption 5:

No drawings exist for large VXF SST liners. Therefore, these dimensions must be assumed. It is appropriate to assume that these dimensions are based on the small VXFs. Per SAR (2021), an empty large VXF may contain an orifice with no plug. However, per the RRD Experiment Guide Number 2 (EG-2) **(**EG-2 2007), the large VXFs should contain a Be plug when not being utilized. It is not desired to have water-filled large VXFs because water acts as a neutron poison in a thermal neutron environment (as shown in Section 4); this is why EG-2 specifies that a Be plug should be loaded when not in use. However, since the SAR states that a large VXF may contain an orifice with no plug, it was assumed that modeling water/SST liners in the large VXFs would provide a bounding case in this study. Changes to the SST liner as-modeled dimensions will have negligible impacts on the calculations performed and documented in this report because most of the volume within the large VXF is water for this case.

Assumption 6:

It is assumed that no water gaps exist between the Be or Al plugs and the Al VXF liners. Furthermore, it is assumed that neglecting the small water gaps has no impact on the reported results.

Justification of Assumption 6:

Modeling no water gap between the Be or Al plugs and the Al VXF liners is consistent with all previous models by Ilas et al. (2015) and Chandler et al. (2020) because the gap is very small and the additional small water volume will have trivial impacts on the reactor physics results. The modeling approach is consistent between the reference (current design) and the perturbed (concept design) models.

Assumption 7:

It is assumed that the PT-1 neutron activation analysis facility will be relocated to VXF-13 in the concept reflector.

Justification of Assumption 7:

The PT-1 facility is foreseen to be loaded into either VXF-9 or VXF-13 of the concept reflector. Placement of PT-1 in VXF-9 provides a location close to that of the existing reflector design’s VXF-7, thus requiring fewer changes to the piping system extending above the reflector. This VXF-9 location would likely render outer large VXF-8 unusable due to the route required for the piping between the pressure vessel head and the experiment facility. Placement of PT-1 in the concept reflector VXF-13 position would require more effort because of the plumbing changes, including entering the pressure vessel through a different location. However, relocating PT-1 to VXF-13 is advantageous because neutron-absorbing experiments could only be potentially loaded in facilities on one side of it (compared to three if loaded in VXF-9), and the plumbing system could be routed above the reflector so as not to interfere with any other VXF. Thus, it is assumed that PT-1 will be in concept reflector VXF-13. Relocation of PT-1 into another VXF within the concept reflector will not affect the safety conclusions of this report.

3. CALCULATION METHODS

This section describes the software, models, inputs, and scripts employed to perform the analyses documented in this report. All calculations were performed using RRD Quality Assurance controlled software.

3.1 DEVELOPMENT OF THE REFERENCE MCNP MODEL

The development of the reference Monte Carlo N-Particle 5 (MCNP5) (MCNP 2003) model is described in this section and is based on the homogenized representative model documented by Chandler et al. (2020). The BOC inputs were developed based on the VESTA (Haeck 2009) depletion input file, which contains the BOC MCNP input underneath the VESTA input block. The PB reflector model was enhanced primarily by generating a finer cell-based mesh and explicitly modeling the coolant holes. Approved RRD drawings were used to model the current Be reflector design, including the VXFs and coolant holes.

ENDF/B-VII.0 neutron cross section data (Chadwick 2006) were used in the transport calculations. The modified ^{27}Al cross section developed and detailed by Chandler et al. (2012), 13027.77c, is used in this study. This modified cross section is based on the ENDF/B-VII.0 data and was modified only to enable the generation and subsequent transportation of the 1.7791 MeV decay gamma coming from the short-lived ^{28}Al isotope that is produced via thermal neutron capture in ^{27}Al. The use of these data results in a more accurate calculation of heat deposition rates in the reactor because many core components are fabricated with Al materials.

The prompt KCODE calculations discussed in Section 4 made use of 200,000 particles per cycle, 50 skipped cycles, and 2,500 active cycles. Thus, a total of 500 million active particles were simulated to yield sufficient statistical precision. The core-delayed fixed-source gamma calculations discussed in Section 4 simulated 1 billion active particles, which also resulted in very low statistical uncertainties.

3.1.1 Reference Model Permanent Reflector Mesh

The permanent reflector documented by Chandler et al. (2020) is modeled with a seven radial by one axial cell mesh, which is adequate for most core physics analyses. A finer 13 radial by 21 axial mesh (273 cells) was used in the analyses documented in this report to calculate the reflector heat generation rates on a fine mesh for use in the follow-on COMSOL thermal-structural calculations. The radial discretization is based on preliminary heat generation rate calculations performed by Chandler et al. (2019). A mesh consisting of 13 radial regions was created based on guidelines, in which N total radial regions are modeled with the first region's Δr being ~1 cm, the Nth region's Δr being <3 cm, and approximately the same amount of heat is deposited in each radial region. The axial mesh was developed by defining a 1 cm Δz region about the core horizontal midplane (i.e., ±0.5 cm) to capture the peak heat deposition rates and 3 cm Δz regions elsewhere less the axial extremes (i.e., the uppermost and lowermost axial regions), which were defined as 2.98 cm Δz regions. The radial and axial boundaries used to define the cell-based mesh, and their corresponding surface numbers are provided in Table 3.1.

Table 3.1. Permanent reflector r-z cell-based mesh.

No.	r (cm)	Δr (cm)	z (cm)	Δz (cm)
0	33.3375	—	30.48	—
1	34.2875	0.95	27.50	2.98
2	35.2875	1.00	24.50	3.00
3	36.3375	1.05	21.50	3.00
4	37.4375	1.10	18.50	3.00
5	38.6375	1.20	15.50	3.00
6	39.9375	1.30	12.50	3.00
7	41.3875	1.45	9.50	3.00
8	42.9875	1.60	6.50	3.00
9	44.7875	1.80	3.50	3.00
10	46.7875	2.00	0.50	3.00
11	49.0875	2.30	−0.50	1.00
12	51.6875	2.60	−3.50	3.00
13	54.6100	2.92	−6.50	3.00
14			−9.50	3.00
15			−12.50	3.00
16			−15.50	3.00
17			−18.50	3.00
18			−21.50	3.00
19			−24.50	3.00
20			−27.50	3.00
21			−30.48	2.98

3.1.2 Reference Model Permanent Reflector Materials

One unique material was defined for each radial region. Thus, each of the 21 axial regions within the same radial boundaries makes use of the same Be material card. The material composition data for the PB reflector, as used in the studies performed by Ilas et al. (2015) and Chandler et al. (2020), is based on homogenizing the Be reflector material (~98 vol. %) with the coolant channel water (~2 vol. %). The Be material composition by element, as provided in the fabrication file for reflector no. 4, is listed in Table 3.2.

Table 3.3 lists the atom density data used for the current PB reflector no. 4 calculations. Isotopic makeup and atomic weight data from the National Institute of Standards and Technology (NIST) (NIST 2018) were used along with the fabrication file density (1.8514 g/cm^3) to calculate the total and isotope-dependent atom densities.

Table 3.2. Elemental composition data for current permanent reflector no. 4.

element	at. no.	provided[a] wt. %	normalized[b] wt. %
Be[c]	4	98.8243	99.1117
C	6	0.11	0.1103
O[c]	8	0.5757	0.5774
Mg	12	0.03	0.0301
Al	13	0.04	0.0401
Si	14	0.03	0.0301
Fe	26	0.1	0.1003
Sum		99.71	100.00

a) Provided weight percent reflects values listed in fabrication file
b) Normalized weight percent reflects values after normalizing total weight % to 100
c) Be and BeO listed as 98.5 and 0.9, respectively

Table 3.3. Atom density data for current permanent reflector no. 4.

element	isotope	atomic wt.	wt. %	g/cm^3	at/b-cm
Be	9	9.012183	99.1117	1.83495E+00	1.22616E-01
O	16	15.9994	0.5774	1.06897E-02	4.02359E-04
C	12	12.01074	0.1103	2.04246E-03	1.02408E-04
Al	27	26.98154	0.0401	7.42714E-04	1.65770E-05
Mg	24	23.98504	0.0235	4.34209E-04	1.09021E-05
Mg	25	24.98584	0.0031	5.72638E-05	1.38018E-06
Mg	26	25.98259	0.0035	6.55626E-05	1.51958E-06
Si	28	27.97693	0.0276	5.11729E-04	1.10152E-05
Si	29	28.97649	0.0015	2.69250E-05	5.59579E-07
Si	30	29.97377	0.0010	1.83815E-05	3.69310E-07
Fe	54	53.93961	0.0057	1.04826E-04	1.17034E-06
Fe	56	55.93494	0.0922	1.70641E-03	1.83718E-05
Fe	57	56.93539	0.0022	4.01134E-05	4.24285E-07
Fe	58	57.93327	0.0003	5.43192E-06	5.64646E-08
		sum	100.00	1.85140E+00	1.23183E-01

3.1.3 Reference Model Permanent Reflector VXF Geometry

The origins of the 22 VXFs are listed in Table 3.4. Of the 22 VXFs, 11 are inner small VXFs, 5 are outer small VXFs, and 6 are large VXFs. Refer to Section 1.2 for more details regarding the current reflector design's VXFs.

The reference model input consists of Be plugs in all the large VXFs and water/SST liners in all the small VXFs because this is considered the typical loading when no unique irradiation experiments are loaded in the permanent reflector. Descriptions of the water/SST liner geometry used for the small VXFs are provided in Table 3.5.

Table 3.4. Summary of current PB reflector VXFs.

region	VXF	row	size	location (degree)[a)]
between HB-1 and HB-2	1	inner	small	85.50
	2	outer	small	94.50
	3	inner	small	103.50
	4	outer	small	112.50
	5	inner	small	121.50
	6	outer	large	130.50
	7	inner	small	139.50
	8	outer	small	148.50
	9	inner	small	157.50
between HB-2 and HB-3	10	outer	small	202.50
	11	inner	small	211.50
	12	outer	small	220.50
	13	inner	small	229.50
	14	outer	large	238.50
	15	inner	small	247.50
	16	outer	large	256.50
between HB-3 and HB-4	17	outer	large	297.00
	18	inner	small	306.00
	19	outer	large	315.00
	20	inner	small	324.00
	21	outer	large	333.00
	22	inner	small	342.00

a) Degree with HB-2 centerline defined as 180°

Table 3.5. Description of the current design small VXF water/SST liner geometry.

r_o (cm)	r_i (cm)	material/description
2.244 (inner VXF) 2.239 (outer VXF)	2.223	water gap between Be and Al liner
2.223	2.012	Al liner
2.012	1.902	water between Al and SST liners
1.902	1.778	SST liner
1.778	0.000	water inside SST liner

The outer radius of the small (inner and outer) VXFs was slightly increased from their ~2.223 cm radius to incorporate a small water-filled annular gap between the Al liner and the Be reflector. There are four and three grooves cut down the inner and outer small VXF hole walls, respectively. Rather than explicitly modeling these grooves (Figure 3.1), a small annular gap between the Be and the Al liner was modeled to account for the coolant water.

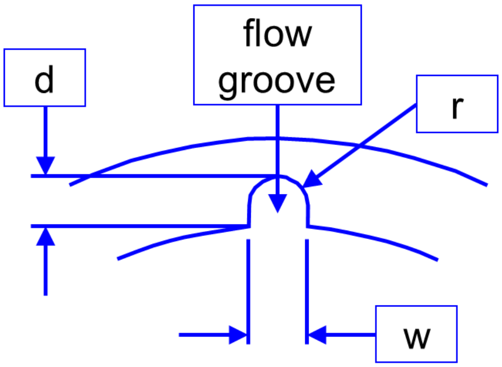

Figure 3.1. Flow groove detail.

The area of a single groove is estimated to be:

$$A = w(d - r) + 0.5\pi r^2 = 0.0755 \text{ cm}^2$$

Then, the equivalent outer radius can be calculated as follows:

$$r_o = \sqrt{\frac{nA}{\pi} + r_i^2}$$

where r_o, n, and r_i are the outer radius of the water gap, the number of grooves per VXF, and the inner radius of the coolant gap (outer radius of the VXF liner), respectively. Outer radii of approximately 2.244 and 2.239 cm are computed for the inner and outer small VXFs, respectively.

Descriptions of the Be plug geometry used in all large VXFs are provided in Table 3.6. The outer radius of the large VXFs was slightly increased from their ~3.81 cm radius to incorporate a small water-filled annular gap between the Al liner and the Be reflector. There are four grooves cut down the large VXF hole walls. Employing the same groove area calculations as described previously for the small VXFs, an equivalent large VXF outer radius of about 3.823 cm is calculated.

Table 3.6. Description of the current design large VXF Be plug geometry.

r_o (cm)	r_i (cm)	material/description
3.823	3.810	water gap between Be and Al liner
3.810	3.599	Al liner
3.599	0.000	Be plug

3.1.4 Reference Model Permanent Reflector Coolant Holes

The 198 coolant channels in the permanent reflector were explicitly modeled in this study primarily to remove the water/Be homogenization assumption detailed in the report by Ilas et al. (2015) to enable more precise heat deposition and reactivity worth estimates. The locations of the permanent reflector coolant holes are provided in Table 3.7. The MCNP geometry uses East as the datum, with angles increasing in the counterclockwise direction; thus, the HB-2 centerline represents 180°.

Table 3.7. Current permanent reflector coolant hole locations.

BCR (cm)	**35.87**	**38.88**	**42.32**	**46.28**
coolant hole no.	**coolant hole location (degree)[a)]**			
1	2.25	0.00	2.25	0.00
2	6.75	4.50	6.75	4.50
3	11.25	9.00	11.25	9.00
4	15.75	13.50	15.75	13.50
5	20.25	18.00	20.25	18.00
6	24.75	22.50	24.75	22.50
7	29.25	27.00	29.25	27.00
8	33.75	31.50	33.75	31.50
9	38.25	36.00	38.25	36.00
10	42.75	40.50	42.75	40.50
11	47.25	45.00	47.25	45.00
12	51.75	49.50	51.75	49.50
13	56.25	54.00	56.25	54.00
14	60.75	58.50	60.75	58.50
15	65.25	63.00	65.25	63.00
16	69.75	67.50	69.75	67.50
17	74.25	72.00	74.25	72.00
18	78.75	76.50	78.75	76.50
19	92.25	94.50	164.25	81.00
20	96.75	112.50	168.75	85.50
21	110.25	130.50	173.25	90.00
22	114.75	148.50	177.75	99.00
23	128.25	166.50	182.25	103.50
24	132.75	171.00	186.75	108.00
25	146.25	175.50	191.25	117.00
26	150.75	180.00	195.75	121.50
27	164.25	184.50	263.25	139.50
28	168.75	189.00	267.75	144.00
29	173.25	193.50	272.25	153.00
30	177.75	198.00	276.75	157.50
31	182.25	202.50	281.25	162.00
32	186.75	220.50	285.75	166.50
33	191.25	238.50	290.25	171.00
34	195.75	256.50	348.75	175.50
35	200.25	261.00	353.25	180.00
36	204.75	265.50	357.75	184.50
37	218.25	270.00		189.00
38	222.75	274.50		193.50

BCR (cm)	**35.87**	**38.88**	**42.32**	**46.28**
coolant hole no.	**coolant hole location (degree)[a)]**			
39	236.25	279.00		198.00
40	240.75	283.50		207.00
41	254.25	288.00		211.50
42	258.75	292.50		216.00
43	263.25	297.00		225.00
44	267.75	315.00		229.50
45	272.25	333.00		247.50
46	276.75	351.00		265.50
47	281.25	355.50		270.00
48	285.75			274.50
49	290.25			279.00
50	294.75			283.50
51	299.25			288.00
52	312.75			306.00
53	317.25			324.00
54	330.75			342.00
55	335.25			346.50
56	348.75			351.00
57	353.25			355.50
58	357.75			

a) Degree with HB-2 centerline defined as 180°

3.1.5 Reference Model MCNP Illustrations

Illustrations of the reference case MCNP model are provided in Figure 3.2 (x-y cross section) and Figure 3.3 (x-z cross section). The x-y cross section shows the permanent reflector radial mesh, coolant channel modeling, and VXF modeling discussed in the previous sections. The x-z cross section plot illustrates the permanent reflector radial and axial mesh, as well as the HB-2 and HB-4 beam tubes in the reflector.

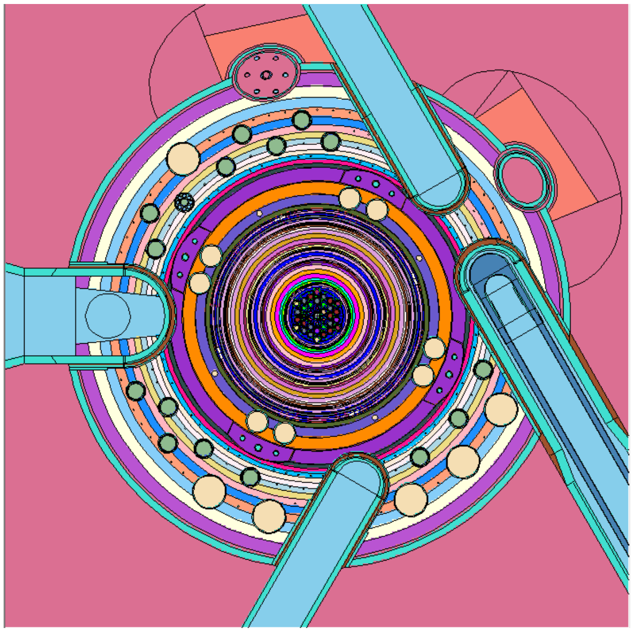

Figure 3.2. X-Y cross section of the reference case MCNP model on the core horizontal midplane.

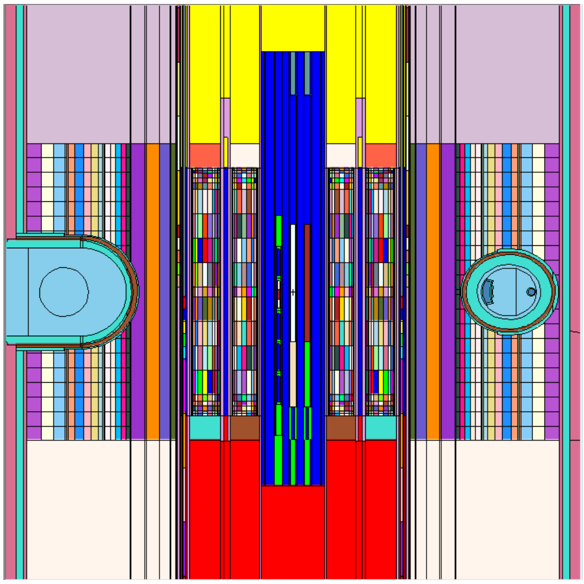

Figure 3.3. X-Z cross section of the reference case MCNP model.

3.2 DEVELOPMENT OF THE CONCEPT DESIGN MCNP MODEL

The concept models developed in this calculation were created by modifying the reference permanent reflector model (1) Be materials; (2) VXF layout, geometry, and contents; and (3) coolant hole layout. The concept models made use of the same radial and axial mesh as that described in Section 3.1.1 for the reference model. As discussed in Section 2, official drawings for the concept PB reflector design have not been produced and approved at this writing; however, check print drawings have been generated and were used as the basis for this study. The design changes with respect to the current design are based mostly on iterative calculations, including the reactor physics and thermal-structural evaluations performed by Chandler et al. (2019).

3.2.1 Concept Model Permanent Reflector Materials

The material composition data for PB reflector no. 5 used to generate the atom densities in the concept models were taken from the certificate of analysis. The Be material composition by element is listed in Table 3.8. Table 3.9 lists the atom density data used for the concept reflector calculations. The measured density (1.8555 g/cm^3) and NIST-based isotopic makeup and atomic weight data (NIST 2018) were used to calculate the total and isotope-dependent atom densities.

Table 3.8. Elemental composition data for concept permanent reflector no. 5.

element	at. no.	provided[a)] wt. %	normalized[b)] wt. %
Be[c)]	4	99.3883	99.1899
C	6	0.07	0.0699
O[c)]	8	0.5117	0.5107
Mg	12	0.03	0.0299
Al	13	0.05	0.0499
Si	14	0.03	0.0299
Fe	26	0.12	0.1198
Sum		100.20	100.00

a) Provided weight percent reflects values listed in fabrication file

b) Normalized weight percent reflects values after normalizing total weight % to 100

c) Be and BeO listed as 99.1 and 0.8, respectively

Table 3.9. Atom density data for concept permanent reflector no. 5.

element	isotope	atomic wt.	wt. %	g/cm^3	at/b-cm
Be	9	9.012183	99.1899	1.84047E+00	1.22984E-01
O	16	15.9994	0.5107	9.47645E-03	3.56692E-04
C	12	12.01074	0.0699	1.29626E-03	6.49939E-05
Al	27	26.98154	0.0499	9.25898E-04	2.06656E-05
Mg	24	23.98504	0.0233	4.33043E-04	1.08728E-05
Mg	25	24.98584	0.0031	5.71100E-05	1.37648E-06
Mg	26	25.98259	0.0035	6.53864E-05	1.51550E-06
Si	28	27.97693	0.0275	5.10354E-04	1.09856E-05
Si	29	28.97649	0.0014	2.68527E-05	5.58075E-07
Si	30	29.97377	0.0010	1.83321E-05	3.68318E-07
Fe	54	53.93961	0.0068	1.25453E-04	1.40063E-06
Fe	56	55.93494	0.1101	2.04220E-03	2.19869E-05
Fe	57	56.93539	0.0026	4.80068E-05	5.07774E-07
Fe	58	57.93327	0.0004	6.50079E-06	6.75755E-08
		sum	100.00	1.85550E+00	1.23476E-01

3.2.2 Concept Model Permanent Reflector VXF Geometry

The locations of the 28 VXFs explicitly modeled in MCNP are illustrated in Figure 1.2. Of the 28 VXFs, 15 are inner small VXFs, three are outer small VXFs, and 10 are large VXFs. Refer to Section 1.3 for more details regarding the concept design's VXFs.

Per SAR Sections 10.2.4.4, "Small vertical experiment facilities," and 10.2.4.5, "Large vertical experiment facilities," a VXF (small or large) may contain a Be plug, an Al plug, or an orifice with no plug when not in use. Per EG-2, the inner and outer small VXFs may contain any of the following, where special experiment capsules and liners require a completed safety review per Experiment Guide Number 1 (EG-1) (EG-1 2013):

- 1.75 in. Be Plug
- Empty Orificed Liner
- Special Experiment Capsule (with a STANDARD liner)
- Special Experiment Capsule (with a SPECIAL liner)
- Special Experiment Capsule (with NO liner)
- Four-Hole Specimen Holder in Short Liner (completely filled with four installed plugs/capsules)
- Four-Hole Specimen Holder in Long Liner (completely filled with four installed plugs/capsules)

Also, per EG-2, the large VXFs may contain the following:

- 3.00 in. Be Plug
- Special Experiment Capsule requiring a completed safety review per EG-1

Various VXF loadings are modeled in the concept design to bound potential, hypothetical configurations without specific experiments loaded into the VXFs. Based on the configurations discussed above, the VXFs of the concept model were modeled with Be plugs, Al plugs, or water/SST liners. Descriptions of the configuration geometries modeled in the small VXFs are provided in Table 3.10 and Table 3.11, respectively.

Table 3.10. Description of the concept design small VXF water/SST liner geometry.

r_o (cm)	r_i (cm)	material/description
2.388	2.372	water gap between Be and Al liner
2.372	2.012	Al liner
2.012	1.902	water between Al and SST liners
1.902	1.778	SST liner
1.778	0.000	water inside SST liner

Table 3.11. Description of the concept design small VXF Be plug and Al plug geometry.

r_o (cm)	r_i (cm)	material/description
2.388	2.372	water gap between Be and Al liner
2.372	2.012	Al liner
2.012	0.000	Be plug or Al plug

The VXF holes in the concept design are slightly larger than those in the current design because the coolant grooves will be machined into the Al liners rather than in the Be walls. The inner radius of the Al liner and the plug/liner dimensions are unchanged from the current design. Per discussion with the principal thermal-structural analyst, it is anticipated that three grooves with the same dimensions as discussed in Section 3.1.3

will be machined down the length of the small VXF Al liners. The small VXF hole outer radius is about 2.388 cm, and thus the equivalent outer radius of the Al liner (inner radius of the water gap) is:

$$r_{o,Al} = \sqrt{r_{o,Be}^2 - \frac{nA}{\pi}} = 2.372\ cm$$

Descriptions of the water/SST liner and Be plug/Al plug geometries modeled in the large VXFs are provided in Table 3.12 and Table 3.13, respectively. The inner radius of the Al liner and the plug dimensions are unchanged from the current design. For the water/SST liner geometry, the same small VXF SST liner thickness (~0.124 cm) and Δr between the Al liner and SST liner (~0.109 cm) are assumed. Per discussion with the thermal-structural analyst, it is anticipated that five grooves will be machined down the length of the large VXF Al liners. The large VXF hole outer radius is about 3.975 cm, and thus the equivalent outer radius of the Al liner is about 3.960 cm.

Table 3.12. Description of the concept design large VXF water/SST liner geometry.

r_o (cm)	r_i (cm)	material/description
3.975	3.960	water gap between Be and Al liner
3.960	3.599	Al liner
3.599	3.490	water between Al and SST liners
3.490	3.366	SST liner
3.366	0.000	water inside SST liner

Table 3.13. Description of the concept design large VXF Be plug and Al plug geometry.

$_{ro}$ (cm)	r_i (cm)	material/description
3.975	3.960	water gap between Be and Al liner
3.960	3.599	Al liner
3.599	0.000	Be plug or Al plug

3.2.3 Concept Model Permanent Reflector Coolant Holes

The 182 coolant channels in the concept permanent reflector were explicitly modeled. The locations of the coolant holes are illustrated in Figure 1.2. Refer to Section 1.3 for more details regarding the concept design's coolant holes.

3.2.4 Concept Model MCNP Illustration

An illustration of the concept reflector case MCNP model is provided in Figure 3.4. This x-y cross section shows the permanent reflector radial mesh, coolant channel modeling, and VXF modeling discussed in the previous sections. The concept model provided in Figure 3.4 illustrates the configuration later referred to as the *equivalent loading case*.

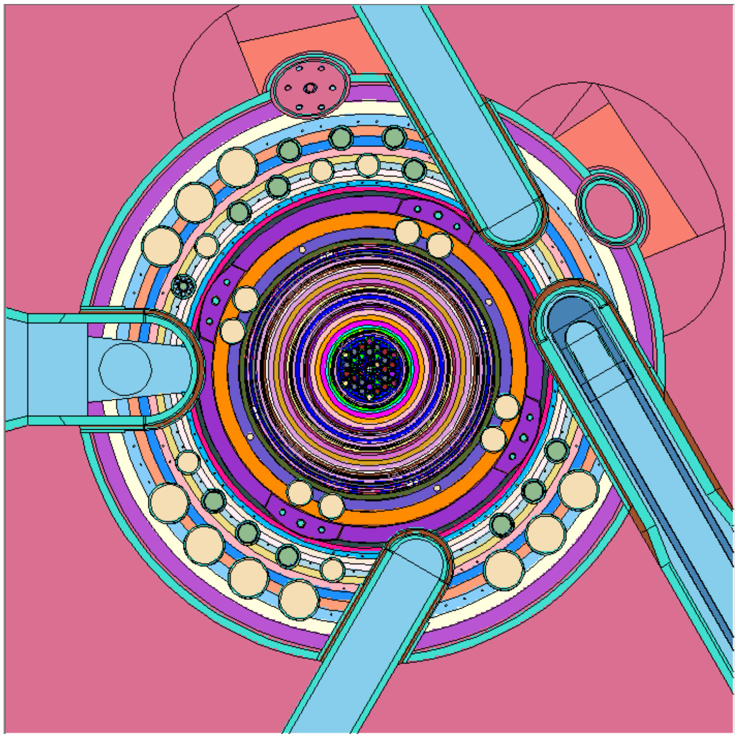

Figure 3.4. X-Y cross section of the concept reflector MCNP model on the core horizontal midplane.

3.3 END-OF-CYCLE MODEL DEVELOPMENT

The EOC inputs were created by modifying the BOC inputs discussed in the previous sections. A total of 443 materials were depleted in the homogeneous representative model VESTA fuel cycle simulation documented by Chandler et al. (2020), including the IFE materials (209 materials), the OFE materials (209 materials), the control element absorber materials (20 materials), the Cm targets (1 material) in the flux trap region, the tungsten target (1 material) in the flux trap region, and the ^{238}Pu production targets (3 materials) in the reflector VXFs. The ^{238}Pu production targets were removed from the BOC reference and concept inputs because, as stated previously, no unique irradiation targets were modeled in the VXFs for this study.

The BOC material cards for all depletion materials were replaced with the material cards provided in the Chandler (2020) MCNP input file that corresponds to EOC. The total atom densities of the 440 materials present in the MCNP cards were also updated. Lastly, the control element axial withdrawn positions that are defined on the tr100 and tr200 cards were changed to fully withdrawn (68.58 cm) to represent EOC conditions. The Python script named boc_to_eoc_input.py was developed and employed to perform the operations discussed above.

3.4 CORE DELAYED GAMMA SOURCES

The core-delayed gamma source cards used in the fixed-source gamma calculations to estimate dose rates and the heat deposition in the Be reflector from core-delayed gammas are based on the ORIGEN (SCALE 2011) source term calculations performed and documented by Chandler et al. (2020) for the explicit representative model. The day 1 and EOC sources are used in this study for the BOC and EOC delayed gamma calculations, respectively. Day 0 results are not used for the BOC calculations because the gamma source estimated at day 0 is for a fresh, unirradiated core with no fission products. Thus, the day 1 gamma source is more appropriate for use in the BOC simulations.

The day 1 and EOC total delayed gamma sources are 2.726 and 2.960 × 10^{19} gammas/second. Illustrations of the gamma source distributions provided in the report by Chandler et al. (2020) are replicated below in Figure 3.5 and Figure 3.6. The delayed gamma source spectrums were resolved in a 57-energy group structure.

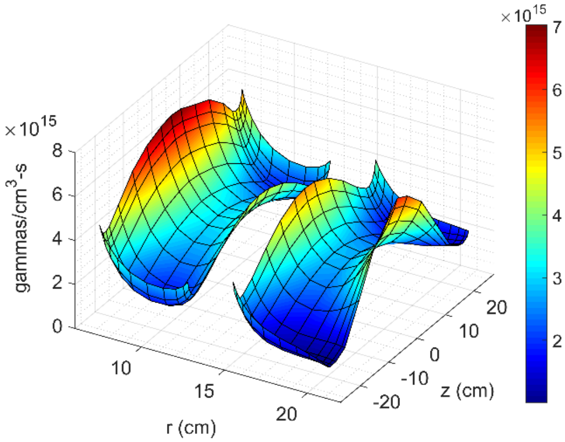

Figure 3.5. Day 1 core delayed gamma source distribution (Chandler 2020)

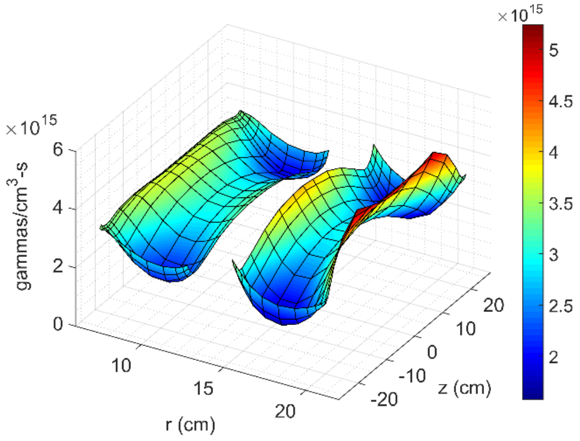

Figure 3.6. EOC core delayed gamma source distribution (Chandler 2020)

3.5 SOURCE NORMALIZATION AND REACTIVITY ASSESSMENTS

MCNP tallies calculated in KCODE mode are normalized per starting particle (i.e., per source fission neutron); therefore, the tally results must be multiplied by the fission neutron source strength. The fission neutron source strength is defined as follows:

$$Sn\left(\frac{fission\ neutrons}{second}\right) = \frac{P(W) \times \bar{\upsilon}(n/fission)}{e(J/MeV) \times Q(MeV/fission) \times k_{eff}},$$

where P is the reactor power in watts, $\bar{\upsilon}$ is the average number of neutrons produced per fission reaction, e is a unit conversion factor, Q is the average recoverable energy released per fission reaction, and k_{eff} is the effective multiplication factor. The multiplication factor and $\bar{\upsilon}$ values calculated and reported in the KCODE run output file are used in the above equation. Physics constants including P, e, and Q are provided in Table 3.14.

Table 3.14. Physics constants for source and reactivity calculations.

parameter	value	units	reference
P	85 × 10^6	W	—
e	1.60218 × 10^{-13}	J/MeV	—
Q_{BOC}	200.51	MeV/fission	(Davidson 2017)
Q_{EOC}	200.92	MeV/fission	(Davidson 2017)
$B_{eff,BOC}$	0.00745	—	(Davidson 2017)
$B_{eff,EOC}$	0.00734	—	(Davidson 2017)
$S_{dg,day1}$	2.726111 × 10^{19}	delayed γ/s	(Chandler 2020)
$S_{dg,EOC}$	2.959758 × 10^{19}	delayed γ/s	(Chandler 2020)

Track length estimate of energy deposition tallies (type 6) are used in the KCODE simulations to calculate Be heating due to neutrons and fission products (F6:N) and prompt+capture photons (F6:P). The typical units corresponding to the F6 tally are MeV/g-fission_neutron; however, the sd card is used in the tallies to assign each tally cell a mass of 1 g because MCNP is not able to calculate the volume/mass of the geometrically complex cells. The cell volumes are calculated in a separate MCNP stochastic ray tracing calculation. The desired prompt heat deposition, H_p, units are W/cm^3, so the prompt tally results, T_p, are modified as follows:

$$H_p\left(\frac{W}{cm^3}\right) = T_p\left(\frac{MeV}{n}\right)\frac{1}{V(cm^3)}\left[\frac{P(W) \times \bar{\upsilon}(n/fission)}{Q(MeV/fission) \times k_{eff}}\right].$$

The result within the hard brackets is the prompt heating multiplier, M_p.

Decay gammas are not included in MCNP photon production cross sections, so fixed-source gamma calculations are performed to estimate heating from core decay gammas. Track length estimates of energy deposition tallies (type 6) are used to calculate the decay gamma heat deposition in the Be cells. The typical units corresponding to the F6 tally are MeV/g-source_gamma; however, the sd card is used in the tallies to assign each tally cell a mass of 1 g. The desired delayed gamma heat deposition, H_{dg}, units are W/cm^3, so the tally results, T_{dg}, are modified as follows:

$$H_{dg}\left(\frac{W}{cm^3}\right) = T_{dg}\left(\frac{MeV}{\gamma}\right)\frac{1}{V(cm^3)}\left[S_{dg}(\gamma/s) \times e(J/MeV)\right].$$

The result within the hard brackets is the delayed gamma heating multiplier, M_d.

Changes in core reactivity are calculated by perturbing the system (i.e., perturbations to the PB reflector) and comparing the multiplication factors of the reference and perturbed cases. The reactivity difference, $\Delta\rho$, between a reference and perturbed case is calculated as:

$$\Delta\rho(¢) = \frac{100}{\beta_{eff}}\left(\frac{k_{per} - k_{ref}}{k_{per}k_{ref}}\right),$$

where β_{eff} is the effective delayed neutron fraction, k_{ref} is the effective multiplication factor calculated for the reference case, k_{per} is the effective multiplication factor calculated for the perturbed case, and 100 is used to convert the reactivity worth from dollars to cents. The standard deviation of the reactivity difference, $\sigma_{\Delta\rho}$, is calculated using error propagation:

$$\sigma^2_{\Delta\rho} = \left(\frac{\partial\Delta\rho}{\partial k_{ref}}\right)^2 \sigma^2_{k_{ref}} + \left(\frac{\partial\Delta\rho}{\partial k_{per}}\right)^2 \sigma^2_{k_{per}},$$

where

$$\left(\frac{\partial\Delta\rho}{\partial k_{ref}}\right) = \frac{100}{\beta_{eff}\, k^2_{ref}} \text{ and } \left(\frac{\partial\Delta\rho}{\partial k_{per}}\right) = -\frac{100}{\beta_{eff}\, k^2_{per}},$$

And thus

$$\sigma_{\Delta\rho}(¢) = \frac{100}{\beta_{eff}}\sqrt{\frac{\sigma^2_{k_{ref}}}{k^4_{ref}} + \frac{\sigma^2_{k_{per}}}{k^4_{per}}}.$$

3.6 ORIGEN ACTIVATION CALCULATIONS

The disadvantage of using Be as a moderator/reflector is the buildup of gases and neutron poisons that lead to swelling, degraded mechanical properties, and increased neutron absorption rates. When ^{9}Be is irradiated by neutrons above ~1 MeV, it undergoes (n,α) and (n,2n) reactions. Beryllium can also undergo (n,γ) reactions when irradiated by thermal neutrons. The main type of reaction that causes Be poisoning is the Be(n,α) reaction that leads to the buildup of ^{6}Li and ^{3}He, two isotopes that have very large thermal absorption cross sections. The primary Be nuclear reaction chain equations that govern the transmutations resulting in gas and neutron poison generation are listed below:

$$^{9}_{4}\mathrm{Be} + ^{1}_{0}n \rightarrow ^{6}_{2}\mathrm{He} + ^{4}_{2}\mathrm{He}$$

$$^{9}_{4}\mathrm{Be} + ^{1}_{0}n \rightarrow 2\,^{4}_{2}\mathrm{He} + 2\,^{1}_{0}n$$

$$^{6}_{2}\mathrm{He} \xrightarrow{0.8\,s} ^{6}_{3}\mathrm{Li} + \beta^{-}$$

$$^{6}_{3}\mathrm{Li} + ^{1}_{0}n \rightarrow ^{4}_{2}\mathrm{He} + ^{3}_{1}\mathrm{H}$$

$$^{3}_{1}\mathrm{H} \xrightarrow{12.3\,yr} ^{3}_{2}\mathrm{He} + \beta^{-}$$

$$^{3}_{2}\mathrm{He} + ^{1}_{0}n \rightarrow ^{3}_{1}\mathrm{H} + ^{1}_{1}p$$

Helium-6 is the result of the ^{9}Be(n,α) reaction and decays quickly into ^{6}Li. The relatively large capture cross section of ^{6}Li, along with the abundance of thermal neutrons in the Be reflector, support the production of tritium (^{3}H), a radioactive isotope of hydrogen that has a half-life of 12.32 years (NNDC 2018). The daughter product of ^{3}H is ^{3}He, which is produced and depleted during reactor operation. During operation, ^{3}He is produced by the decay of ^{3}H and is depleted according to the ^{3}He(n,p) nuclear reaction. However, in a no flux environment (i.e., an outage), the ^{3}He concentration significantly increases because there is no destruction mechanism. This phenomenon must be considered—especially during long outage periods—to account for its reactivity effects on the startup of the reactor.

Beryllium activation studies were performed in this study to assess how the various configurations analyzed impact gas (e.g., ^{3}H, ^{3}He, and ^{4}He) and neutron poison (e.g., ^{3}He and ^{6}Li) buildup. The SCALE 6.1.3 suite (SCALE 2011) was used to perform activation, decay, and source term calculations. The Python script documented in a paper by Chandler et al. (2016) used to activate ^{238}Pu production target materials was modified for use in this evaluation to activate the PB reflector materials.

The method performed in this study consisted of calculating 44-energy group neutron fluxes and nuclide-specific cross sections for the Be cells located on the core horizontal midplane at one state point (i.e., BOC or EOC) with MCNP and then activating them with their respective fluxes and cross sections. A higher fidelity simulation may be performed later by considering flux and cross section changes that occur during a cycle and the life of the reflector to account for control element withdrawal and material evolutions. This type of higher fidelity study was performed by Chandler et al. for ^{238}Pu production studies; however, the ^{238}Pu targets are only irradiated for 2–3 cycles, whereas the reflector is irradiated for ~132 cycles. The employed method will provide a consistent approach to compare results for several reflector configurations.

The COUPLE and ORIGEN modules were used to perform the Be activation calculations. The COUPLE code, utilizing the BOC or EOC 44-energy group neutron flux spectrum as cross section weighting data, was used to collapse the 44-group AMPX neutron activation cross sections into one-group format as required by ORIGEN. User-input cross sections for Be(n,2n), Be(n,α), Li(n,t), and He(n,p) were calculated with MCNP and provided to COUPLE to override the flux-weighted cross sections.

For the ORIGEN calculations, 25 d fuel cycles were modeled with 25 d decay periods between cycles, which are typical to operations. A total of 132 cycles at 85 MW were simulated to effectively bound the life of a typical permanent reflector because the lifetime of the reflector is 279,000 MWd and this simulation covers 280,500 MWd. The volumes calculated from MCNP ray tracing calculations and the densities/material compositions listed in Sections 3.1.2 and 3.2.1 were used to calculate the element-dependent masses to define as the initial inventory to activate. All the above operations were performed with the pb_2_origen.py Python script.

3.7 PYTHON EXECUTION AND POST-PROCESSING SCRIPTS

Several Python scripts were developed in this study to help set up, execute, and post-process the MCNP and ORIGEN calculations. Brief descriptions of the implemented scripts are provided in Table 3.15.

Table 3.15. Descriptions of the implemented Python scripts.

Python script	Description
mcnp_exe.py	Generates the MCNP file describing the nodes/cores to run on, sets up the MCNP executable line, and runs MCNP
boc_to_eoc_input.py	Converts the BOC inputs to EOC inputs by modifying the depletion materials' material cards and total atom densities and updating the control element positions
calc_extraction.py	Provides the required input data pointing to the MCNP files to post-process and executes the post-processing scripts described below
calc_meshtal_extraction.py	Post-processing script called from calc_extraction.py that extracts the results from the MCNP mesh tally files (meshtal), normalizes the results, organizes the results, and writes the results to easy to read and interpret text files
calc_output_extraction.py	Post-processing script called from calc_extraction.py that extracts the results from the MCNP prompt, delayed, and volume output files; normalizes the results; organizes the results; and writes the results to easy to read and interpret text files
calc_comparisons.py	Script to read in the organized, processed results text files and generate plots that compare the reference results to the perturbed results
run_origen.py	Provides the input data and pointers required by the pb_2_origen.py script and then executes the pb_2_origen.py script
pb_2_origen.py	Script called from run_origen.py to write the COUPLE/ORIGEN inputs, execute the inputs, post-process the pertinent nuclide and decay heat results, and write the results to easy to read and interpret text files
nuclide_comps.py	Reads in the nuclides text files and compares the results of the reference case to those of the perturbed cases
decay_heat_comps.py	Reads in the decay heat text files and compares the results of the reference case to those of the perturbed cases

4. COMPUTATIONS AND ANALYSES

This section describes the computations and analyses performed in this study. The models and methods employed in this section are described in Section 3. Various configurations were modeled for bounding analyses. Six cases were modeled, each at BOC and EOC, and are described in Table 4.1. The reference input, which may be denoted as "ref," is the current Be reflector no. 4 design with water/SST liners in all small VXFs and Be plugs in all large VXFs. Case "mat," for material change, is identical to the reference case except for the Be reflector material density and composition. The reference no. 4 properties were changed to the no. 5 properties to evaluate the impact of the slightly different density and composition before characterizing differences in reflector geometries and VXF loadings. Four cases were modeled with the concept permanent reflector design; the only differences were the geometry and materials within the VXFs. The "ber," "wat," and "alu" cases model Be plugs, water/SST liners, and Al plugs, respectively, in all concept reflector VXFs. Lastly, the equivalent concept case, "equ," models nine inner small VXFs and all three outer small VXFs with water/SST liners, and it models five inner small VXFs and all ten large VXFs with Be plugs. This case results in a reactivity equivalent to that of the reference case.

Table 4.1. Matrix of cases and configurations analyzed.

case ID	reflector	VXF loading[a)]	notes
ref	current	water/SST liners in all small VXFs Be plugs in all large VXFs	typical, current configuration when no experiments are loaded in the VXFs
mat	current	same as ref	only change to ref includes density and composition change from no. 4 to no. 5 properties
ber	concept	Be plugs in all VXFs	most desirable loading from a core and neutron scattering perspective
wat	concept	water/SST liners in all VXFs	least desirable loading from a core and neutron scattering perspective
alu	concept	Al plugs in all VXFs	an alternative loading with Al plugs
equ	concept	water/SST liners in 9 inner small VXFs and all 3 outer small VXFs Be plugs in 5 small VXFs and all large VXFs	loading that is equivalent to ref in terms of reactivity worth

a) PT-1 modeled in current reflector VXF-7 and concept reflector VXF-13

4.1 CORE REACTOR PHYSICS

This section documents the computations and analyses performed for core reactor physics. Calculations and results detailed in the following subsections largely include reactivity worth estimates, impacts on core fission rate distributions, and region-dependent neutron absorption rates. Previous safety analyses have indicated that minor asymmetries in the PB reflector have negligible impacts on core physics. Additionally, a calculated change in eigenvalue due to a perturbation, such as the VXF layout and contents, can be a useful indicator of potential changes in core physics, including cycle length, shutdown margin, and power distribution. Per Section 4.3.1.3, "Reactivity and power distribution control," of the reference SAR document (2021), minor asymmetries in the PB reflector—such as the beam tubes or experiments in the irradiation facilities—have been found to have negligible effect on the core power peaking. The following is excerpted from an evaluation by Bucholz (1997), which is the neutronics safety–related calculation performed in support of the HB-2 enlargement introduced in permanent reflector no. 4.

Calculated changes in eigenvalues as a result of changing the reflector design can (approximately) quantify or bound the following potential operational and safety impacts on the reactor:

a) *Operating cycle length. The impact on the operating cycle length is directly related to the change in calculated eigenvalue at nominal "EOC" conditions.*
b) *Shutdown margin. The operational shutdown margin, i.e. the scram worth of the safety plates with the reactor critical, could be decreased due to a reduction in permanent reflector albedo (e.g. due to increased beam tube size). This effect would be most apparent in the rods-out eigenvalue. Since the eigenvalue with safety plates in is little affected by reflection, a change in the calculated rods-out eigenvalue resulting from changes in the reflector design is a reasonable and (slightly) conservative upper bound for the impact on scram worth.*
c) *Power distribution. The core power distribution can be impacted by changes in neutron reflection, as for example with strong neutron absorbers located in RB irradiation facilities. Since the effect on power distribution resulting from the change in reflector design, if any, is a result of locally reduced neutron reflection which also causes an eigenvalue reduction, a change in the calculated rods-out eigenvalue is a sensitive indicator of the potential for a local power shape distortion. Prior experience [1][*] shows that the eigenvalue perturbation can be calculated with greater precision than the accompanying small local power shape distortions.*

[*] *[sic]*

4.1.1 Reactivity Worth

The effective multiplication factors, average number of neutrons produced per fission, and multipliers calculated for the BOC and EOC cases are respectively provided in Table 4.2 and Table 4.3. The metrics provided in these tables are used to appropriately normalize the results throughout Section 4.

Table 4.2. BOC eigenvalues and multipliers.

metric	units	ref.	mat.	ber.	wat.	alu.	equ.
k_{eff}	—	1.00121	1.00124	1.00230	1.00054	1.00092	1.00123
σ_{keff}	—	0.00004	0.00004	0.00004	0.00004	0.00004	0.00004
$\bar{\upsilon}$	n/fiss.	2.440	2.440	2.440	2.440	2.440	2.440
S_n	#/s	6.44817E+18	6.44797E+18	6.44115E+18	6.45248E+18	6.45003E+18	6.44804E+18
M_p	W/MeV	1.03311E+06	1.03308E+06	1.03199E+06	1.03380E+06	1.03341E+06	1.03309E+06
M_d	W/MeV	4.36772E+06	4.36772E+06	4.36772E+06	4.36772E+06	4.36772E+06	4.36772E+06

Table 4.3. EOC eigenvalues and multipliers.

metric	units	ref.	mat.	ber.	wat.	alu.	equ.
k_{eff}	—	1.00054	1.00061	1.00307	0.99879	0.99959	1.00045
σ_{keff}	—	0.00004	0.00004	0.00004	0.00004	0.00004	0.00004
$\bar{\upsilon}$	n/fiss.	2.441	2.441	2.441	2.441	2.441	2.441
S_n	#/s	6.44196E+18	6.44151E+18	6.42571E+18	6.45324E+18	6.44808E+18	6.44254E+18
M_p	W/MeV	1.03212E+06	1.03205E+06	1.02951E+06	1.03393E+06	1.03310E+06	1.03221E+06
M_d	W/MeV	4.74207E+06	4.74207E+06	4.74207E+06	4.74207E+06	4.74207E+06	4.74207E+06

The reactivity worth of the five perturbed cases relative to the reference case—as calculated with the MCNP-calculated effective multiplication factors and the methods described in Section 3.5—are provided in Table 4.4. The reactivity worths at EOC are approximately 2–3 times greater than those at BOC because the control elements withdraw during the cycle, and the reflector's influence on reactivity is greatest at EOC, when the control elements are fully withdrawn. The material and equivalent cases have statistically equivalent reactivities relative to the reference case (i.e., within 1–2 standard deviations). The concept Be plug case results in a notable reactivity increase because of the increase in Be material, whereas the concept water/SST liner case results in a notable reactivity decrease because of the increase in water and steel in the reflector. Although Al has a trivial capture cross section, a negative reactivity worth is calculated for the Al plug case because neutrons interacting with Al are not reflected into the core. Thus, reactivity differences are dependent on the VXF contents.

Table 4.4. Reactivity worth relative to reference case.

case	**beginning-of-cycle**		**end-of-cycle**	
	ρ (¢)	**σ_ρ (¢)**	**ρ (¢)**	**σ_ρ (¢)**
mat.	0.40	0.76	0.95	0.77
ber.	14.58	0.76	34.34	0.77
wat.	−8.98	0.76	−23.86	0.77
alu.	−3.88	0.76	−12.94	0.77
equ.	0.27	0.76	−1.22	0.77

The range of reactivity worth differences calculated for all cases analyzed is −24 to +35 cents. These values may not be considered negligible; however, they are considered small relative to previously irradiated experiments and cycle-to-cycle variations in selected reactor components' compositions. A few examples are provided below.

1. The EOC reactivity worth of the RB-19J experiment that was irradiated in a large removable Be reflector experiment facility in 2016 was approximately −85¢ (Daily 2016).
2. Per the BOC estimated symmetrical critical control element procedure (SBP 2021), the worth attributed to ^{182}Ta buildup in the inner control element could be as large as 0.55 in. Using a typical, generic differential rod worth of $2.90/in. (Chandler 2020), which corresponds to 18.0 inches withdrawn, the ^{182}Ta worth could be as large as ±$1.54.
3. The worth attributed to ^{182}Ta buildup in the outer control elements could be as large as 0.45 in. [SBP, 2021]. Thus, the ^{182}Ta worth could be as large as ±$1.31, assuming a rod worth of $2.90/in.
4. The worth attributed to ^{6}Li buildup in the removable reflector, which is exposed to a much greater flux than the permanent reflector, could be as large as 0.24 in. following replacement (SBP 2021). The ^{6}Li worth could thus be as large as ±70¢ assuming a rod worth of $2.90/in.
5. The worth attributed to ^{3}He buildup in the removable reflector can typically be as large as ~0.17 inches assuming adjacent 15 d and 50 d outages (SBP 2021), which are typical of short and long outages. A typical upper bound ^{3}He worth is thus ±48¢ assuming a rod worth of $2.90/in.

Bounding contents were modeled, and the reactivity differences were proven to be small relative to typical cycle-to-cycle reactivity variations. The concept PB no. 5 itself has no impact on core reactivity; however, the contents of the VXFs can have a small reactivity impact. Thus, it is concluded that the concept reflector design will have no significant impact on cycle length, safety margin, core reactivity coefficients, or differential/integral rod worths. The choice of the VXF contents is ultimately up to RRD personnel, and if a slightly longer cycle is desired, more Be plugs could be loaded into the inner small VXFs to enhance neutron reflection.

4.1.2 Fission Rate Distribution

Understanding the core fission rate distribution is critical to HFIR safety and operations because it is the key input to the safety basis steady-state and transient thermal-hydraulic analyses documented in the SAR. The local fission rate density (flux, power, etc.) perturbation, also referred to as a *flux tilt* in SAR, caused by the presence of all experiments is limited to 9%. This 9% flux tilt factor combined with a 10% power distribution uncertainty factor makeup U_3 ($1.09 \times 1.10 = 1.199$), which is an uncertainty factor implemented in the HFIR safety basis thermal-hydraulic analyses.

The 2D (r-z) and 3D (r-z-θ) fission rate density distributions are calculated for these bounding cases and are compared to those of the reference case to determine the maximum increases in local fission rate density. Fission rate densities in the IFE and OFE are computed via F4:N FMESH tallies and the appropriate fission rate multipliers. The radial and axial boundaries of the superimposed mesh correspond to the homogenized model's cell-based mesh, which is 11 radial by 19 axial, for each the IFE and OFE. The 3D mesh tally subdivides each r-z mesh into 24 azimuthal segments, each with an arc angle of 15°.

The impact of the concept design with Be plugs, water/SST liners, and an equivalent loading on EOC fission rate density distributions are illustrated in Figure 4.1, Figure 4.2, and Figure 4.3, respectively. EOC results are shown because the impact of the changes is greatest at EOC when the control elements are fully withdrawn. Conclusions drawn from the BOC results are similar to those at EOC, but the magnitude of the changes are slightly greater at EOC. As shown in these figures, the perturbations analyzed have small-to-negligible impacts. The Be plugs case results in a fission rate density increase of ~1% on the outer edge of the outer fuel element for the r-z distribution, and a max local r-z-θ increase of ~2.5%. For the water/SST case, the fission rate density is slightly depressed at the outer edge of the OFE relative to the reference case, but no notable increases were observed. The reference and equivalent loading cases yield essentially statistically equivalent r-z and r-z-θ distributions. When evaluating these figures, it is very important to consider the statistical uncertainties, especially for the r-z-θ results, because small mesh cells can result in undesirable statistical uncertainties for ratios so close to unity. Thus, some engineering judgement is required to correctly interpret the results.

ber-to-ref r-z fission rate density ratios

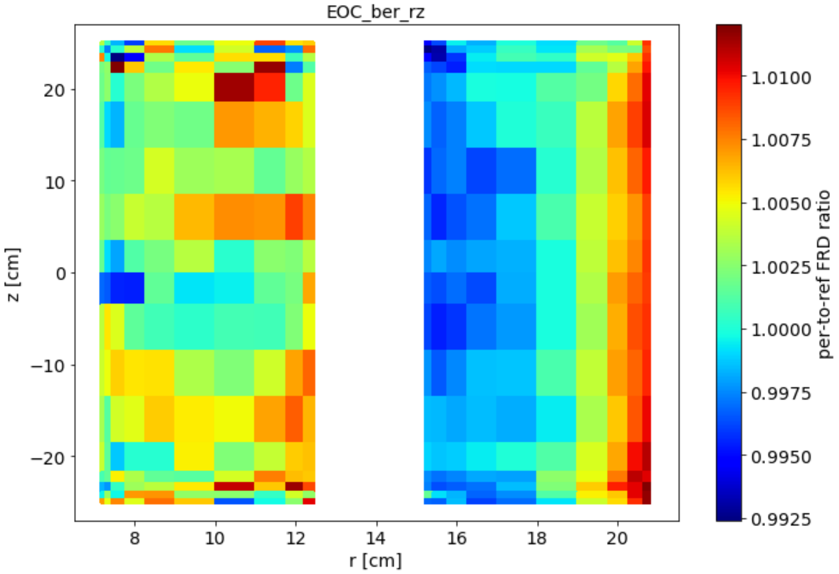

ber-to-ref max(r-z-θ) fission rate density ratios

ber-to-ref max(r-z-θ) fission rate density ratio percent uncertainties

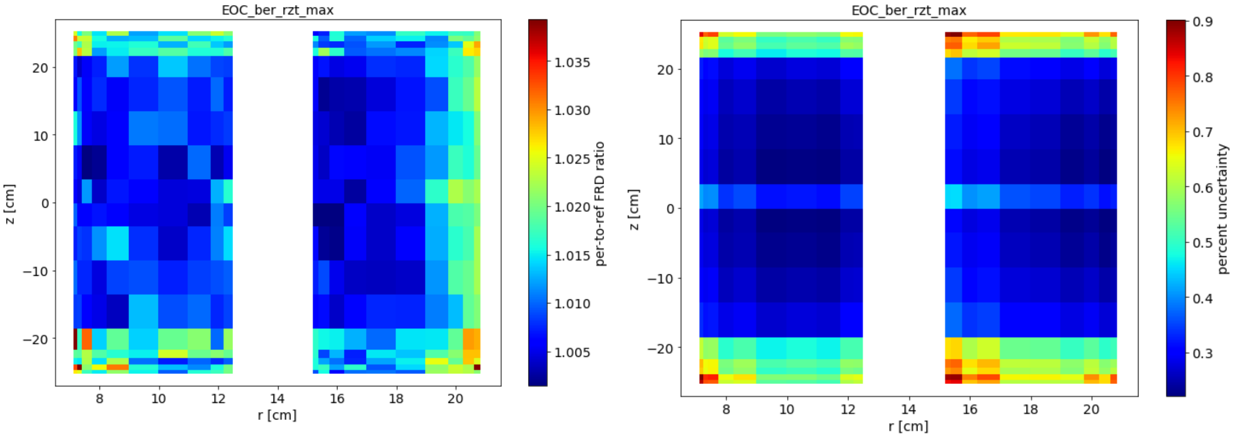

Figure 4.1. Impact of concept design with Be plugs on fission rate density.

wat-to-ref r-z fission rate density ratios

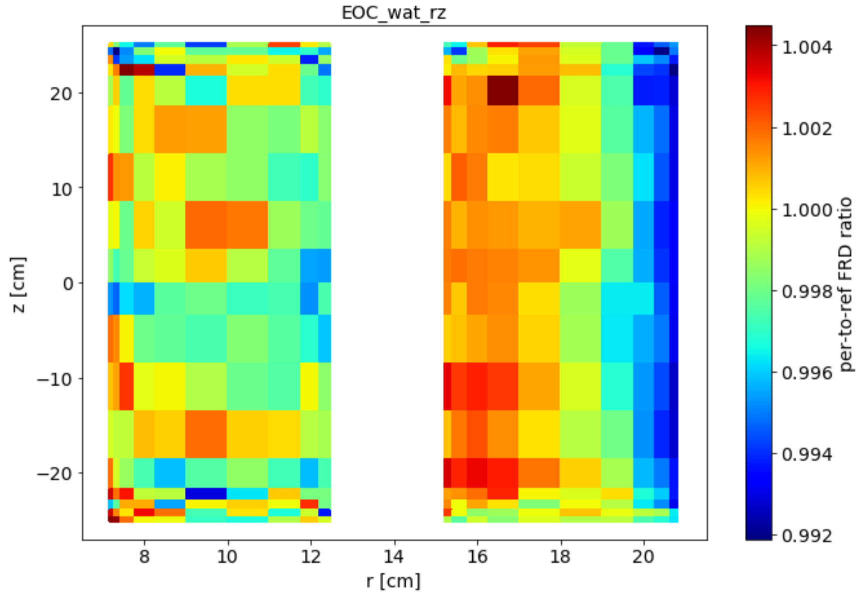

wat-to-ref max(r-z-θ) fission rate density ratios

wat-to-ref max(r-z-θ) fission rate density ratio percent uncertainties

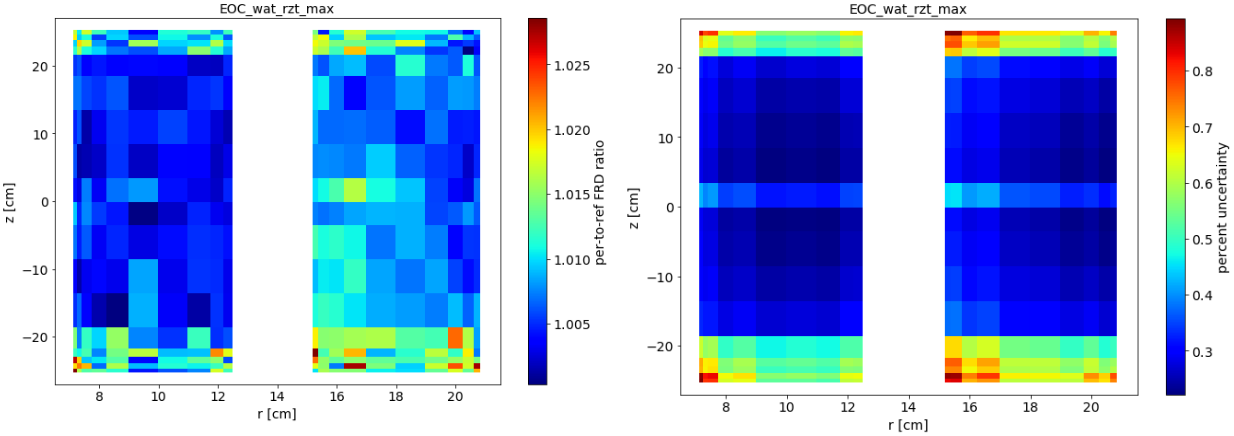

Figure 4.2. Impact of concept design with water/SST liner on fission rate density.

equ-to-ref r-z fission rate density ratios

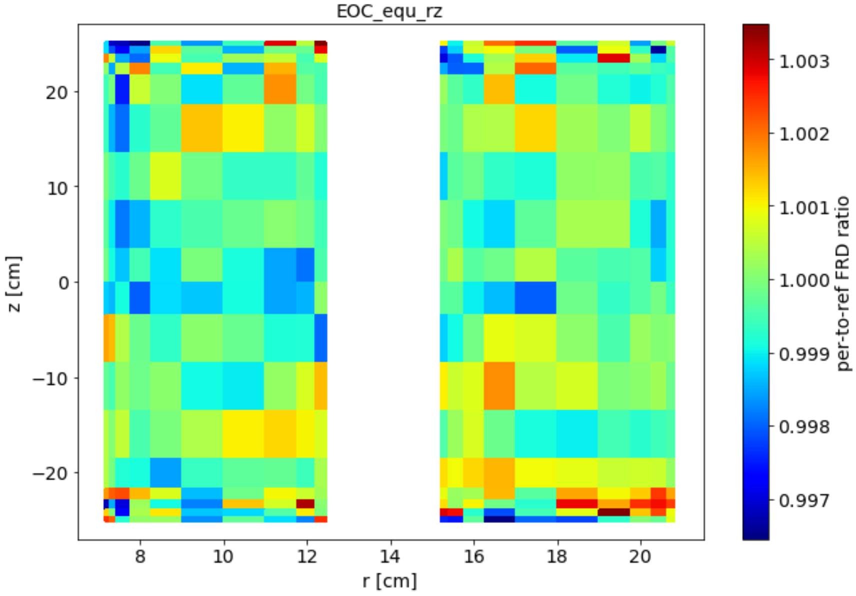

equ-to-ref max(r-z-θ) fission rate density ratios

equ-to-ref max(r-z-θ) fission rate density ratio percent uncertainties

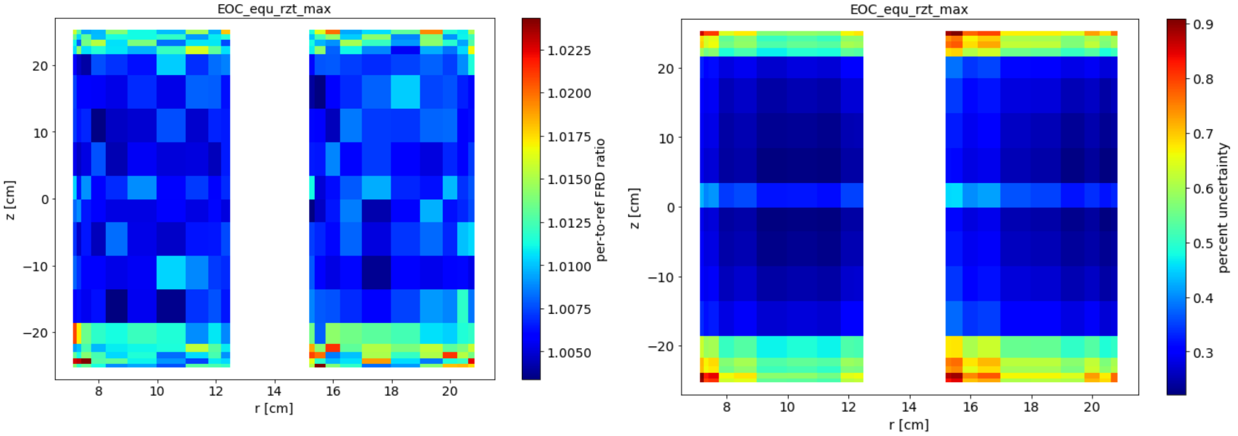

Figure 4.3. Impact of concept design with an equivalent loading on fission rate density.

4.1.3 Region-Dependent Absorption Rates

A requirement was established that the reflector be designed containing a minimum amount of water to avoid excess neutron absorption. As shown in the previous sections, the various configurations have negligible impacts on core physics; thus, any region-wise absorption shifts encountered should be considered acceptable from a safety perspective. The absorption rate in the six major HFIR regions—including the flux trap target region, the IFE, the OFE, the control element region, the removable plus semi-permanent region, and the PB reflector—is calculated for each perturbed case and compared to the reference case.

A F4:N FMESH tally with a multiplier including the absorption reaction MT (−2) is used to estimate the absorption rates on the defined mesh. The prescribed mesh is axially bounded by ±30.48 cm with respect to the core horizontal midplane and is radially bounded by the IFE inner sidewall inner radius, the radial center of the labyrinth region between the fuel elements—calculated as 0.5 × (13.43660 + 14.26845) cm—the OFE outer sidewall outer radius, the inner radius of the Al liner adjacent to the removable Be, the inner radius of the PB reflector, and the outer radius of the PB. Thus, absorptions beyond the PB reflector and outside the ±30.48 cm axial bounds are not scored.

The BOC and EOC region-dependent absorption rates and differences with respect to the reference case are listed in Table 4.5 and Table 4.6, respectively. Considering all regions, trivial differences relative to the reference case are noted for the material change and equivalent loading cases. Negligible differences are noted in the flux trap, IFE, OFE, and control element regions for all the perturbed cases. As expected, the introduction of large amounts of water in the concept water/SST liner case results in a large increase in neuron absorptions, and the introduction of additional Be plugs yields a large reduction in neutron absorptions. It was concluded that the impact of the concept design has no impact on the absorption rate distribution. The choice of the VXF contents has the potential to affect the neutron absorption rate in the Be reflector only. Large local (i.e., within the Be reflector) changes have negligible impacts on the core because of the location of the permanent reflector relative to the core.

Table 4.5. BOC region-dependent absorption rates.

region[a)]	ref.	mat.		ber.		wat.		alu.		equ.	
	(#/s)[b)]	(#/s)[b)]	(%)[c)]	(#/s)[b)]	(%)[c)]	(#/s)[b)]	(%)[c)]	(#/s)[b)]	(%)[c)]	(#/s)[b)]	(%)[c)]
FTT	2.23	2.23	−0.04	2.23	−0.25	2.23	0.07	2.23	0.01	2.23	−0.04
IFE	6.28	6.28	−0.04	6.27	−0.20	6.29	0.08	6.28	0.03	6.28	−0.02
OFE	6.33	6.33	0.01	6.33	0.08	6.32	−0.05	6.32	−0.01	6.32	0.00
CE	11.08	11.08	0.02	11.20	1.10	11.00	−0.75	11.04	−0.38	11.08	−0.03
RB+SPB	2.00	2.00	0.03	2.08	3.94	1.94	−3.04	1.95	−2.30	2.00	−0.26
PB	3.54	3.54	0.09	2.72	−23.18	4.28	21.08	3.23	−8.59	3.49	−1.50

a) Flux trap target (FTT), inner fuel element (IFE), outer fuel element (OFE), control element (CE), removable + semi-permanent (RB+SPB), PB
b) Absorption rate ×10^{17} absorptions per second
c) Percent difference with respect to the ref. case

Table 4.6. EOC region dependent absorption rates.

region[a)]	ref.	mat.		ber.		wat.		alu.		equ.	
	(#/s)[b)]	(#/s)[b)]	(%)[c)]	(#/s)[b)]	(%)[c)]	(#/s)[b)]	(%)[c)]	(#/s)[b)]	(%)[c)]	(#/s)[b)]	(%)[c)]
FTT	2.35	2.35	0.01	2.34	−0.42	2.36	0.32	2.35	0.15	2.35	0.00
IFE	6.14	6.14	−0.01	6.12	−0.38	6.16	0.26	6.15	0.14	6.14	−0.01
OFE	10.10	10.10	0.00	10.11	0.18	10.08	−0.12	10.09	−0.07	10.10	0.00
CE	3.75	3.75	0.02	3.80	1.39	3.71	−0.99	3.73	−0.59	3.75	−0.06
RB+SPB	3.00	3.00	0.06	3.10	3.48	2.92	−2.66	2.93	−2.14	2.99	−0.24
PB	4.49	4.49	0.03	3.46	−22.90	5.41	20.51	4.15	−7.58	4.43	−1.37

a) Flux trap target (FTT), inner fuel element (IFE), outer fuel element (OFE), control element (CE), removable + semi-permanent (RB+SPB), PB
b) Absorption rate ×10^{17} absorptions per second
c) Percent difference with respect to the ref. case

4.2 BERYLLIUM REFLECTOR PHYSICS

This section documents the computations and analyses focused on the PB reflector physics. Calculations and results detailed in the following subsections largely include volume, heat deposition, peak fast fluence, and gas/neutron poison generation.

4.2.1 Volume Calculation

Particle fluxes calculated with MCNP are estimated as track length per unit volume; thus, knowing the volumes of the geometric cells being tallied on is essential. MCNP automatically calculates volumes of polyhedral cells and cells generated by surfaces of revolution about any axis (MCNP 2003). However, for complicated cell geometries such as those that are non-rotationally symmetric or non-polyhedral cells, a stochastic volume method that uses ray tracing can be employed to estimate volumes of the cells of interest. The Be reflector cells being tallied on are geometrically complex because of the regions removed to incorporate experiment facilities (e.g., beam tubes, slant facility tubes).

Cell volumes are therefore required to determine the volumetric heating rates, neutron fluxes, and reaction rates within each cell of interest. The volumes can either be input to the MCNP simulations used to calculate the physics, or they can be used in the postprocessing of the results. The volume of the 273 Be cells are determined stochastically through the use of a F4:N cell tally, the *void* card, and a spherical neutron source. The *void* card essentially “voids out” all the materials in the problem; MCNP does not keep track of the material densities or materials in the model during the volume calculation. A bounding source sphere is set up around the entire problem. This bounding surface floods the HFIR geometry with incoming source neutrons, where the neutron weight, w, is equal to πr^2, where r is the radius of the bounding sphere. These neutrons traverse through the geometry and the F4:N tally tracks the neutrons within each cell; the unit flux from the tally provides the volumes for each cell. The bounding sphere, defined as MCNP surface 10, was specified with a radius of 1,000 cm. A total of 1×10^{11} neutrons were simulated to achieve small statistical uncertainties.

Two volume calculations were performed: one for the current reflector no. 4 design and one for the concept reflector no. 5 design. The volumes do not change from BOC to EOC or when different VXF loadings are modeled. The total calculated volumes of the current and concept reflectors are 0.292 and 0.275 m^3; thus, the concept reflector, with six more VXFs than the current reflector, has approximately 6% less Be material.

4.2.2 Heat Deposition Rates

Heat deposition results are required for the follow-on thermal-structural-hydraulic analyses that will primarily analyze temperature and stress distributions within the Be reflector. The primary contributor to nuclear heating within the beryllium reflector is prompt and capture gammas. Neutrons and core delayed gammas also contribute to the total heat deposition. Heating caused by radionuclide decay within the Be reflector (e.g., β from ^{6}He decay, γ) is considered small and negligible. Details regarding decay heat are provided in Section 4.2.4.3. Gammas produced via ^{28}Al decay provide a large contribution of the total local gamma decay heat, which is considered trivial, but this gamma is produced and transported in the prompt radiation transport calculations as described in Section 3.1.

Neutron and prompt plus capture gamma heat deposition is calculated with MCNP prompt KCODE simulations and F6:N and F6:P tallies. Heat deposition induced by core-delayed gammas are calculated with MCNP fixed-source decay gamma simulations and the F6:P tally. Two-dimensional heat deposition distributions were studied and are reported in this section; however, 3D heat deposition rate distributions were also explored as discussed in Appendix A.

The total heat deposited in the permanent reflector and the volume-averaged volumetric heat deposition rates are provided in Table 4.7. The total heat deposited in the current reflector design was calculated to be 584 and 698 kW at BOC and EOC, respectively. Less heat is deposited in the concept reflector cases because the concept reflector has approximately 6% less Be volume than the current reflector; however, the reflector-average volumetric heat deposition rates are relatively similar for all six cases. Also, the heat deposition results increase approximately 20% from BOC to EOC.

Table 4.7. BOC and EOC permanent reflector heating summary.

parameter	ref.	mat.	ber.	wat.	alu.	equ.
H_{boc} (kW)	583.6	584.6	543.4	555.5	553.9	551.0
H_{boc} (W/cm^3)	1.996	1.999	1.978	2.022	2.016	2.006
H_{eoc} (kW)	697.8	698.8	649.5	664.4	664.0	659.1
H_{eoc} (W/cm^3)	2.386	2.390	2.364	2.418	2.417	2.399

The r-z spatially dependent BOC and EOC total volumetric heat deposition rates for the reference, material, Be plug, water/SST liner, Al plug, and equivalent cases are illustrated and listed in Figure 4.4–Figure 4.9 in the form of heatmaps. The spatially dependent relative errors are low and vary between 0.0003 and 0.0011 (i.e., 0.11%). Additionally, the variation of the BOC and EOC heat deposition results are illustrated in the form of line plots in Figure 4.10 for the reference, the concept with Be plugs, and the concept with water/SST liners cases. The EOC percent differences in heat deposition between the perturbed and reference cases are provided in Figure 4.11. As shown in this figure, the case-to-case variation in heat deposition is less than 5% because the primary heating mechanism is prompt gammas that have high penetrating power. The main differences between the various cases are caused by capture gamma production and neutron/gamma moderation/absorption differences within the materials loaded in the VXFs.

The Figure 4.10 and Figure 4.11 x-axes, titled “i,” have a range of 1–273 to represent the 273 PB reflector cells. The first 21 values correspond to the innermost radial region from the axial top of the reflector (i = 1) to the axial bottom of the reflector (i = 21); thus, the reflector cell corresponding to the innermost radial region on the core horizontal midplane is i = 11. This pattern repeats itself for the other 12 radial regions, such that i values 22–42 represent radial region 2 and i values 253–273 represent the outermost radial region 13.

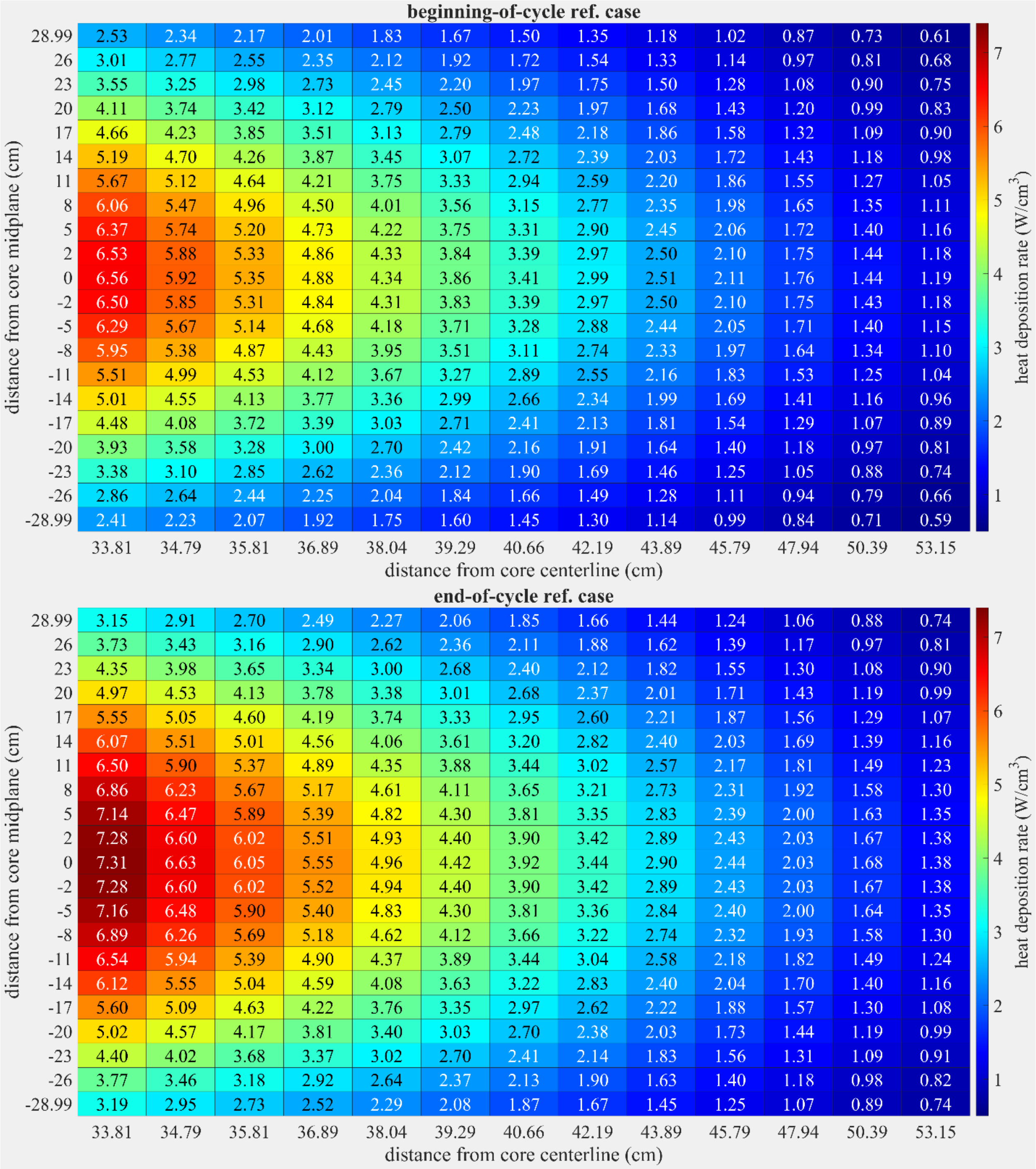

beginning-of-cycle ref. case

	33.81	34.79	35.81	36.89	38.04	39.29	40.66	42.19	43.89	45.79	47.94	50.39	53.15
28.99	2.53	2.34	2.17	2.01	1.83	1.67	1.50	1.35	1.18	1.02	0.87	0.73	0.61
26	3.01	2.77	2.55	2.35	2.12	1.92	1.72	1.54	1.33	1.14	0.97	0.81	0.68
23	3.55	3.25	2.98	2.73	2.45	2.20	1.97	1.75	1.50	1.28	1.08	0.90	0.75
20	4.11	3.74	3.42	3.12	2.79	2.50	2.23	1.97	1.68	1.43	1.20	0.99	0.83
17	4.66	4.23	3.85	3.51	3.13	2.79	2.48	2.18	1.86	1.58	1.32	1.09	0.90
14	5.19	4.70	4.26	3.87	3.45	3.07	2.72	2.39	2.03	1.72	1.43	1.18	0.98
11	5.67	5.12	4.64	4.21	3.75	3.33	2.94	2.59	2.20	1.86	1.55	1.27	1.05
8	6.06	5.47	4.96	4.50	4.01	3.56	3.15	2.77	2.35	1.98	1.65	1.35	1.11
5	6.37	5.74	5.20	4.73	4.22	3.75	3.31	2.90	2.45	2.06	1.72	1.40	1.16
2	6.53	5.88	5.33	4.86	4.33	3.84	3.39	2.97	2.50	2.10	1.75	1.44	1.18
0	6.56	5.92	5.35	4.88	4.34	3.86	3.41	2.99	2.51	2.11	1.76	1.44	1.19
-2	6.50	5.85	5.31	4.84	4.31	3.83	3.39	2.97	2.50	2.10	1.75	1.43	1.18
-5	6.29	5.67	5.14	4.68	4.18	3.71	3.28	2.88	2.44	2.05	1.71	1.40	1.15
-8	5.95	5.38	4.87	4.43	3.95	3.51	3.11	2.74	2.33	1.97	1.64	1.34	1.10
-11	5.51	4.99	4.53	4.12	3.67	3.27	2.89	2.55	2.16	1.83	1.53	1.25	1.04
-14	5.01	4.55	4.13	3.77	3.36	2.99	2.66	2.34	1.99	1.69	1.41	1.16	0.96
-17	4.48	4.08	3.72	3.39	3.03	2.71	2.41	2.13	1.81	1.54	1.29	1.07	0.89
-20	3.93	3.58	3.28	3.00	2.70	2.42	2.16	1.91	1.64	1.40	1.18	0.97	0.81
-23	3.38	3.10	2.85	2.62	2.36	2.12	1.90	1.69	1.46	1.25	1.05	0.88	0.74
-26	2.86	2.64	2.44	2.25	2.04	1.84	1.66	1.49	1.28	1.11	0.94	0.79	0.66
-28.99	2.41	2.23	2.07	1.92	1.75	1.60	1.45	1.30	1.14	0.99	0.84	0.71	0.59

end-of-cycle ref. case

	33.81	34.79	35.81	36.89	38.04	39.29	40.66	42.19	43.89	45.79	47.94	50.39	53.15
28.99	3.15	2.91	2.70	2.49	2.27	2.06	1.85	1.66	1.44	1.24	1.06	0.88	0.74
26	3.73	3.43	3.16	2.90	2.62	2.36	2.11	1.88	1.62	1.39	1.17	0.97	0.81
23	4.35	3.98	3.65	3.34	3.00	2.68	2.40	2.12	1.82	1.55	1.30	1.08	0.90
20	4.97	4.53	4.13	3.78	3.38	3.01	2.68	2.37	2.01	1.71	1.43	1.19	0.99
17	5.55	5.05	4.60	4.19	3.74	3.33	2.95	2.60	2.21	1.87	1.56	1.29	1.07
14	6.07	5.51	5.01	4.56	4.06	3.61	3.20	2.82	2.40	2.03	1.69	1.39	1.16
11	6.50	5.90	5.37	4.89	4.35	3.88	3.44	3.02	2.57	2.17	1.81	1.49	1.23
8	6.86	6.23	5.67	5.17	4.61	4.11	3.65	3.21	2.73	2.31	1.92	1.58	1.30
5	7.14	6.47	5.89	5.39	4.82	4.30	3.81	3.35	2.83	2.39	2.00	1.63	1.35
2	7.28	6.60	6.02	5.51	4.93	4.40	3.90	3.42	2.89	2.43	2.03	1.67	1.38
0	7.31	6.63	6.05	5.55	4.96	4.42	3.92	3.44	2.90	2.44	2.03	1.68	1.38
-2	7.28	6.60	6.02	5.52	4.94	4.40	3.90	3.42	2.89	2.43	2.03	1.67	1.38
-5	7.16	6.48	5.90	5.40	4.83	4.30	3.81	3.36	2.84	2.40	2.00	1.64	1.35
-8	6.89	6.26	5.69	5.18	4.62	4.12	3.66	3.22	2.74	2.32	1.93	1.58	1.30
-11	6.54	5.94	5.39	4.90	4.37	3.89	3.44	3.04	2.58	2.18	1.82	1.49	1.24
-14	6.12	5.55	5.04	4.59	4.08	3.63	3.22	2.83	2.40	2.04	1.70	1.40	1.16
-17	5.60	5.09	4.63	4.22	3.76	3.35	2.97	2.62	2.22	1.88	1.57	1.30	1.08
-20	5.02	4.57	4.17	3.81	3.40	3.03	2.70	2.38	2.03	1.73	1.44	1.19	0.99
-23	4.40	4.02	3.68	3.37	3.02	2.70	2.41	2.14	1.83	1.56	1.31	1.09	0.91
-26	3.77	3.46	3.18	2.92	2.64	2.37	2.13	1.90	1.63	1.40	1.18	0.98	0.82
-28.99	3.19	2.95	2.73	2.52	2.29	2.08	1.87	1.67	1.45	1.25	1.07	0.89	0.74

Figure 4.4. Reference case heat deposition rate distribution.

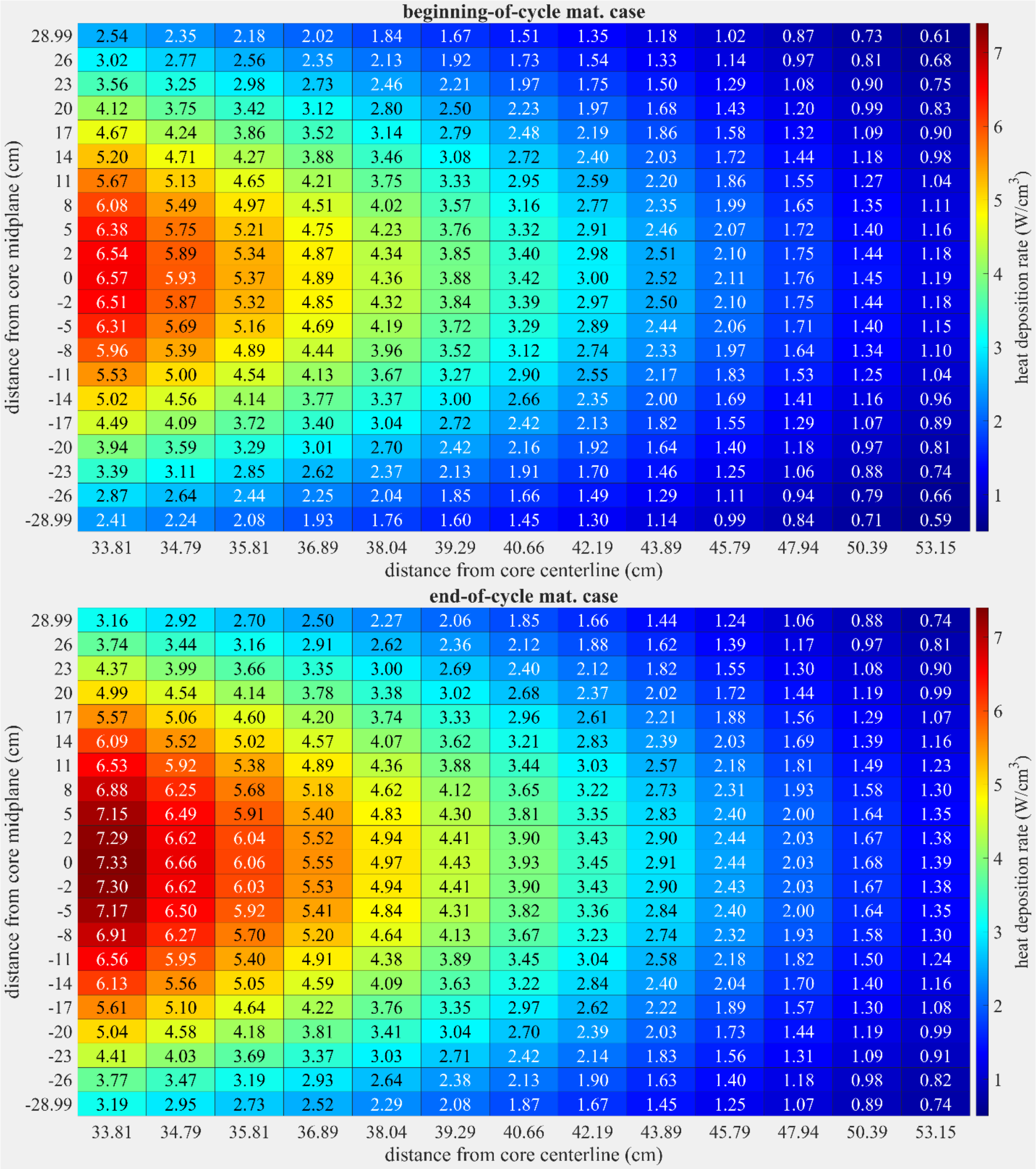

beginning-of-cycle mat. case

	33.81	34.79	35.81	36.89	38.04	39.29	40.66	42.19	43.89	45.79	47.94	50.39	53.15
28.99	2.54	2.35	2.18	2.02	1.84	1.67	1.51	1.35	1.18	1.02	0.87	0.73	0.61
26	3.02	2.77	2.56	2.35	2.13	1.92	1.73	1.54	1.33	1.14	0.97	0.81	0.68
23	3.56	3.25	2.98	2.73	2.46	2.21	1.97	1.75	1.50	1.29	1.08	0.90	0.75
20	4.12	3.75	3.42	3.12	2.80	2.50	2.23	1.97	1.68	1.43	1.20	0.99	0.83
17	4.67	4.24	3.86	3.52	3.14	2.79	2.48	2.19	1.86	1.58	1.32	1.09	0.90
14	5.20	4.71	4.27	3.88	3.46	3.08	2.72	2.40	2.03	1.72	1.44	1.18	0.98
11	5.67	5.13	4.65	4.21	3.75	3.33	2.95	2.59	2.20	1.86	1.55	1.27	1.04
8	6.08	5.49	4.97	4.51	4.02	3.57	3.16	2.77	2.35	1.99	1.65	1.35	1.11
5	6.38	5.75	5.21	4.75	4.23	3.76	3.32	2.91	2.46	2.07	1.72	1.40	1.16
2	6.54	5.89	5.34	4.87	4.34	3.85	3.40	2.98	2.51	2.10	1.75	1.44	1.18
0	6.57	5.93	5.37	4.89	4.36	3.88	3.42	3.00	2.52	2.11	1.76	1.45	1.19
-2	6.51	5.87	5.32	4.85	4.32	3.84	3.39	2.97	2.50	2.10	1.75	1.44	1.18
-5	6.31	5.69	5.16	4.69	4.19	3.72	3.29	2.89	2.44	2.06	1.71	1.40	1.15
-8	5.96	5.39	4.89	4.44	3.96	3.52	3.12	2.74	2.33	1.97	1.64	1.34	1.10
-11	5.53	5.00	4.54	4.13	3.67	3.27	2.90	2.55	2.17	1.83	1.53	1.25	1.04
-14	5.02	4.56	4.14	3.77	3.37	3.00	2.66	2.35	2.00	1.69	1.41	1.16	0.96
-17	4.49	4.09	3.72	3.40	3.04	2.72	2.42	2.13	1.82	1.55	1.29	1.07	0.89
-20	3.94	3.59	3.29	3.01	2.70	2.42	2.16	1.92	1.64	1.40	1.18	0.97	0.81
-23	3.39	3.11	2.85	2.62	2.37	2.13	1.91	1.70	1.46	1.25	1.06	0.88	0.74
-26	2.87	2.64	2.44	2.25	2.04	1.85	1.66	1.49	1.29	1.11	0.94	0.79	0.66
-28.99	2.41	2.24	2.08	1.93	1.76	1.60	1.45	1.30	1.14	0.99	0.84	0.71	0.59

end-of-cycle mat. case

	33.81	34.79	35.81	36.89	38.04	39.29	40.66	42.19	43.89	45.79	47.94	50.39	53.15
28.99	3.16	2.92	2.70	2.50	2.27	2.06	1.85	1.66	1.44	1.24	1.06	0.88	0.74
26	3.74	3.44	3.16	2.91	2.62	2.36	2.12	1.88	1.62	1.39	1.17	0.97	0.81
23	4.37	3.99	3.66	3.35	3.00	2.69	2.40	2.12	1.82	1.55	1.30	1.08	0.90
20	4.99	4.54	4.14	3.78	3.38	3.02	2.68	2.37	2.02	1.72	1.44	1.19	0.99
17	5.57	5.06	4.60	4.20	3.74	3.33	2.96	2.61	2.21	1.88	1.56	1.29	1.07
14	6.09	5.52	5.02	4.57	4.07	3.62	3.21	2.83	2.39	2.03	1.69	1.39	1.16
11	6.53	5.92	5.38	4.89	4.36	3.88	3.44	3.03	2.57	2.18	1.81	1.49	1.23
8	6.88	6.25	5.68	5.18	4.62	4.12	3.65	3.22	2.73	2.31	1.93	1.58	1.30
5	7.15	6.49	5.91	5.40	4.83	4.30	3.81	3.35	2.83	2.40	2.00	1.64	1.35
2	7.29	6.62	6.04	5.52	4.94	4.41	3.90	3.43	2.90	2.44	2.03	1.67	1.38
0	7.33	6.66	6.06	5.55	4.97	4.43	3.93	3.45	2.91	2.44	2.03	1.68	1.39
-2	7.30	6.62	6.03	5.53	4.94	4.41	3.90	3.43	2.90	2.43	2.03	1.67	1.38
-5	7.17	6.50	5.92	5.41	4.84	4.31	3.82	3.36	2.84	2.40	2.00	1.64	1.35
-8	6.91	6.27	5.70	5.20	4.64	4.13	3.67	3.23	2.74	2.32	1.93	1.58	1.30
-11	6.56	5.95	5.40	4.91	4.38	3.89	3.45	3.04	2.58	2.18	1.82	1.50	1.24
-14	6.13	5.56	5.05	4.59	4.09	3.63	3.22	2.84	2.40	2.04	1.70	1.40	1.16
-17	5.61	5.10	4.64	4.22	3.76	3.35	2.97	2.62	2.22	1.89	1.57	1.30	1.08
-20	5.04	4.58	4.18	3.81	3.41	3.04	2.70	2.39	2.03	1.73	1.44	1.19	0.99
-23	4.41	4.03	3.69	3.37	3.03	2.71	2.42	2.14	1.83	1.56	1.31	1.09	0.91
-26	3.77	3.47	3.19	2.93	2.64	2.38	2.13	1.90	1.63	1.40	1.18	0.98	0.82
-28.99	3.19	2.95	2.73	2.52	2.29	2.08	1.87	1.67	1.45	1.25	1.07	0.89	0.74

Figure 4.5. Material case heat deposition rate distribution.

beginning-of-cycle ber. case

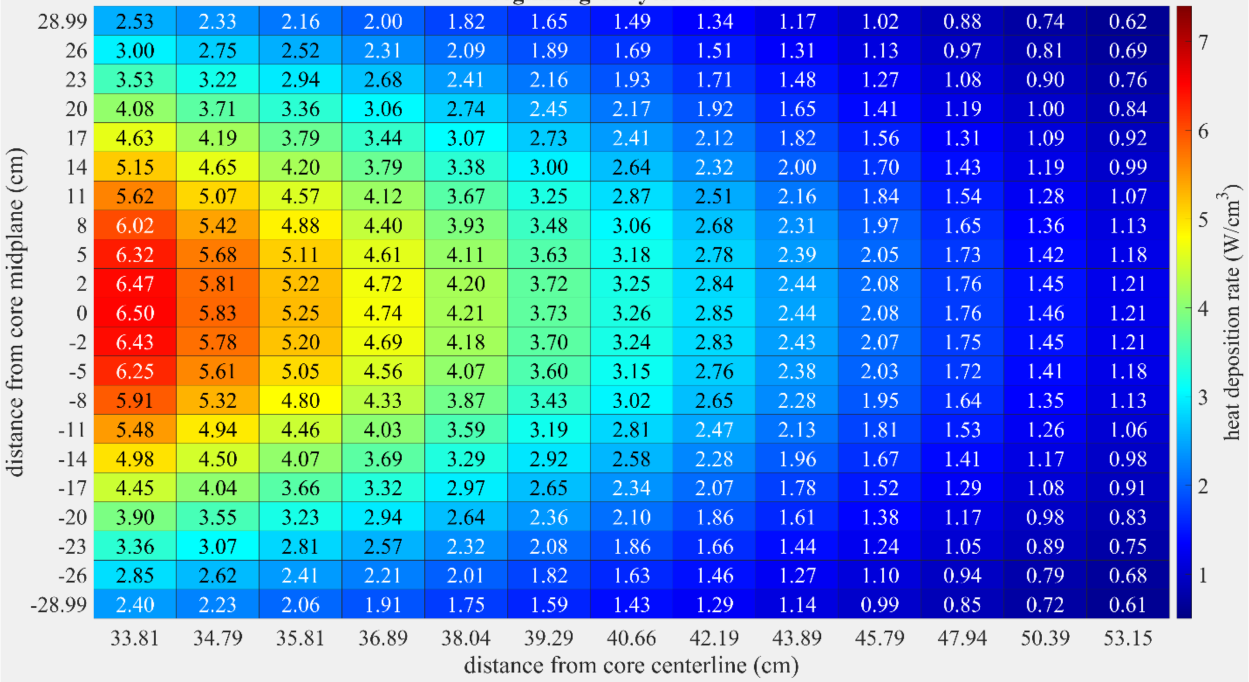

distance from core midplane (cm)	33.81	34.79	35.81	36.89	38.04	39.29	40.66	42.19	43.89	45.79	47.94	50.39	53.15
28.99	2.53	2.33	2.16	2.00	1.82	1.65	1.49	1.34	1.17	1.02	0.88	0.74	0.62
26	3.00	2.75	2.52	2.31	2.09	1.89	1.69	1.51	1.31	1.13	0.97	0.81	0.69
23	3.53	3.22	2.94	2.68	2.41	2.16	1.93	1.71	1.48	1.27	1.08	0.90	0.76
20	4.08	3.71	3.36	3.06	2.74	2.45	2.17	1.92	1.65	1.41	1.19	1.00	0.84
17	4.63	4.19	3.79	3.44	3.07	2.73	2.41	2.12	1.82	1.56	1.31	1.09	0.92
14	5.15	4.65	4.20	3.79	3.38	3.00	2.64	2.32	2.00	1.70	1.43	1.19	0.99
11	5.62	5.07	4.57	4.12	3.67	3.25	2.87	2.51	2.16	1.84	1.54	1.28	1.07
8	6.02	5.42	4.88	4.40	3.93	3.48	3.06	2.68	2.31	1.97	1.65	1.36	1.13
5	6.32	5.68	5.11	4.61	4.11	3.63	3.18	2.78	2.39	2.05	1.73	1.42	1.18
2	6.47	5.81	5.22	4.72	4.20	3.72	3.25	2.84	2.44	2.08	1.76	1.45	1.21
0	6.50	5.83	5.25	4.74	4.21	3.73	3.26	2.85	2.44	2.08	1.76	1.46	1.21
-2	6.43	5.78	5.20	4.69	4.18	3.70	3.24	2.83	2.43	2.07	1.75	1.45	1.21
-5	6.25	5.61	5.05	4.56	4.07	3.60	3.15	2.76	2.38	2.03	1.72	1.41	1.18
-8	5.91	5.32	4.80	4.33	3.87	3.43	3.02	2.65	2.28	1.95	1.64	1.35	1.13
-11	5.48	4.94	4.46	4.03	3.59	3.19	2.81	2.47	2.13	1.81	1.53	1.26	1.06
-14	4.98	4.50	4.07	3.69	3.29	2.92	2.58	2.28	1.96	1.67	1.41	1.17	0.98
-17	4.45	4.04	3.66	3.32	2.97	2.65	2.34	2.07	1.78	1.52	1.29	1.08	0.91
-20	3.90	3.55	3.23	2.94	2.64	2.36	2.10	1.86	1.61	1.38	1.17	0.98	0.83
-23	3.36	3.07	2.81	2.57	2.32	2.08	1.86	1.66	1.44	1.24	1.05	0.89	0.75
-26	2.85	2.62	2.41	2.21	2.01	1.82	1.63	1.46	1.27	1.10	0.94	0.79	0.68
-28.99	2.40	2.23	2.06	1.91	1.75	1.59	1.43	1.29	1.14	0.99	0.85	0.72	0.61

distance from core centerline (cm)

end-of-cycle ber. case

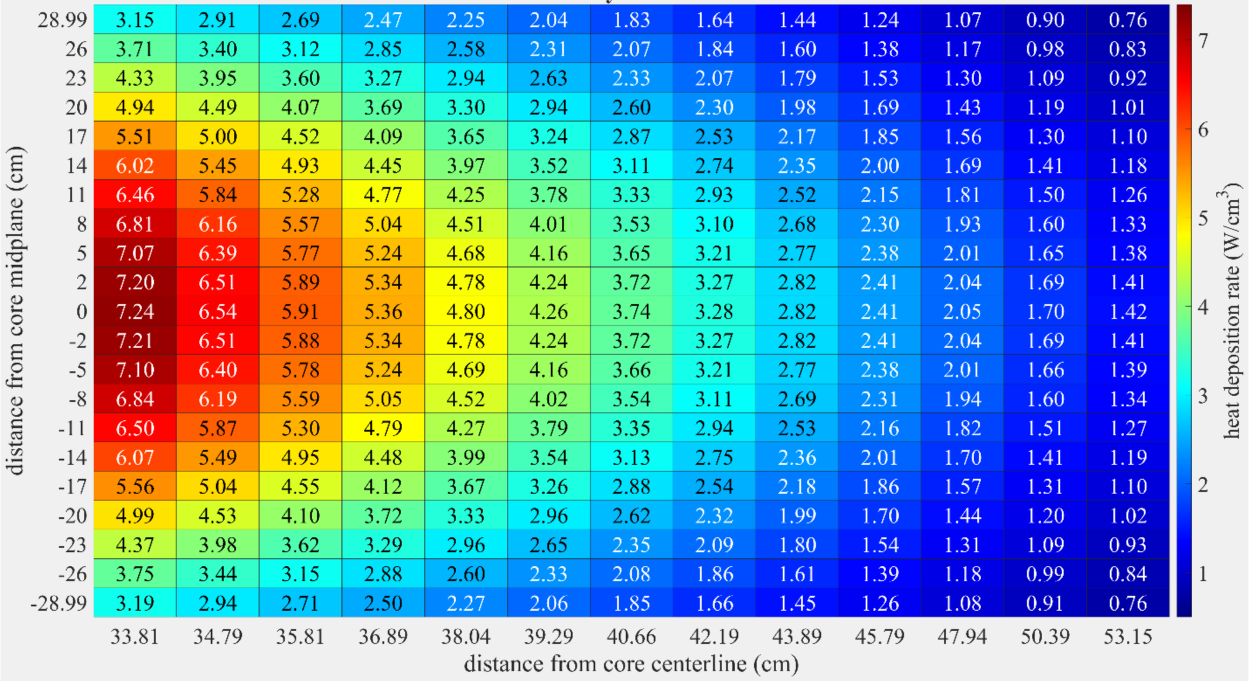

distance from core midplane (cm)	33.81	34.79	35.81	36.89	38.04	39.29	40.66	42.19	43.89	45.79	47.94	50.39	53.15
28.99	3.15	2.91	2.69	2.47	2.25	2.04	1.83	1.64	1.44	1.24	1.07	0.90	0.76
26	3.71	3.40	3.12	2.85	2.58	2.31	2.07	1.84	1.60	1.38	1.17	0.98	0.83
23	4.33	3.95	3.60	3.27	2.94	2.63	2.33	2.07	1.79	1.53	1.30	1.09	0.92
20	4.94	4.49	4.07	3.69	3.30	2.94	2.60	2.30	1.98	1.69	1.43	1.19	1.01
17	5.51	5.00	4.52	4.09	3.65	3.24	2.87	2.53	2.17	1.85	1.56	1.30	1.10
14	6.02	5.45	4.93	4.45	3.97	3.52	3.11	2.74	2.35	2.00	1.69	1.41	1.18
11	6.46	5.84	5.28	4.77	4.25	3.78	3.33	2.93	2.52	2.15	1.81	1.50	1.26
8	6.81	6.16	5.57	5.04	4.51	4.01	3.53	3.10	2.68	2.30	1.93	1.60	1.33
5	7.07	6.39	5.77	5.24	4.68	4.16	3.65	3.21	2.77	2.38	2.01	1.65	1.38
2	7.20	6.51	5.89	5.34	4.78	4.24	3.72	3.27	2.82	2.41	2.04	1.69	1.41
0	7.24	6.54	5.91	5.36	4.80	4.26	3.74	3.28	2.82	2.41	2.05	1.70	1.42
-2	7.21	6.51	5.88	5.34	4.78	4.24	3.72	3.27	2.82	2.41	2.04	1.69	1.41
-5	7.10	6.40	5.78	5.24	4.69	4.16	3.66	3.21	2.77	2.38	2.01	1.66	1.39
-8	6.84	6.19	5.59	5.05	4.52	4.02	3.54	3.11	2.69	2.31	1.94	1.60	1.34
-11	6.50	5.87	5.30	4.79	4.27	3.79	3.35	2.94	2.53	2.16	1.82	1.51	1.27
-14	6.07	5.49	4.95	4.48	3.99	3.54	3.13	2.75	2.36	2.01	1.70	1.41	1.19
-17	5.56	5.04	4.55	4.12	3.67	3.26	2.88	2.54	2.18	1.86	1.57	1.31	1.10
-20	4.99	4.53	4.10	3.72	3.33	2.96	2.62	2.32	1.99	1.70	1.44	1.20	1.02
-23	4.37	3.98	3.62	3.29	2.96	2.65	2.35	2.09	1.80	1.54	1.31	1.09	0.93
-26	3.75	3.44	3.15	2.88	2.60	2.33	2.08	1.86	1.61	1.39	1.18	0.99	0.84
-28.99	3.19	2.94	2.71	2.50	2.27	2.06	1.85	1.66	1.45	1.26	1.08	0.91	0.76

distance from core centerline (cm)

Figure 4.6. Beryllium plug case heat deposition rate distribution.

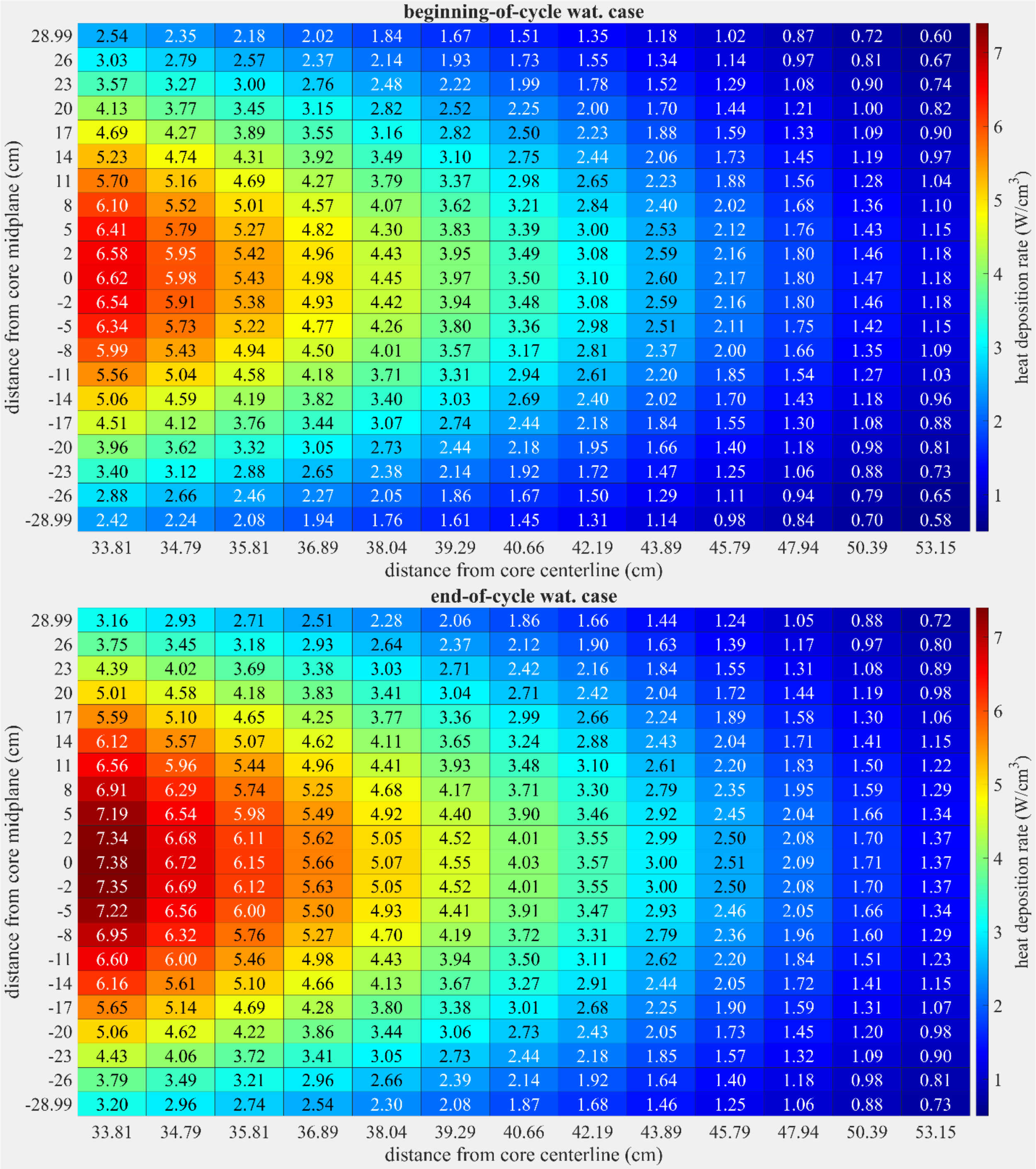

beginning-of-cycle wat. case

	33.81	34.79	35.81	36.89	38.04	39.29	40.66	42.19	43.89	45.79	47.94	50.39	53.15
28.99	2.54	2.35	2.18	2.02	1.84	1.67	1.51	1.35	1.18	1.02	0.87	0.72	0.60
26	3.03	2.79	2.57	2.37	2.14	1.93	1.73	1.55	1.34	1.14	0.97	0.81	0.67
23	3.57	3.27	3.00	2.76	2.48	2.22	1.99	1.78	1.52	1.29	1.08	0.90	0.74
20	4.13	3.77	3.45	3.15	2.82	2.52	2.25	2.00	1.70	1.44	1.21	1.00	0.82
17	4.69	4.27	3.89	3.55	3.16	2.82	2.50	2.23	1.88	1.59	1.33	1.09	0.90
14	5.23	4.74	4.31	3.92	3.49	3.10	2.75	2.44	2.06	1.73	1.45	1.19	0.97
11	5.70	5.16	4.69	4.27	3.79	3.37	2.98	2.65	2.23	1.88	1.56	1.28	1.04
8	6.10	5.52	5.01	4.57	4.07	3.62	3.21	2.84	2.40	2.02	1.68	1.36	1.10
5	6.41	5.79	5.27	4.82	4.30	3.83	3.39	3.00	2.53	2.12	1.76	1.43	1.15
2	6.58	5.95	5.42	4.96	4.43	3.95	3.49	3.08	2.59	2.16	1.80	1.46	1.18
0	6.62	5.98	5.43	4.98	4.45	3.97	3.50	3.10	2.60	2.17	1.80	1.47	1.18
-2	6.54	5.91	5.38	4.93	4.42	3.94	3.48	3.08	2.59	2.16	1.80	1.46	1.18
-5	6.34	5.73	5.22	4.77	4.26	3.80	3.36	2.98	2.51	2.11	1.75	1.42	1.15
-8	5.99	5.43	4.94	4.50	4.01	3.57	3.17	2.81	2.37	2.00	1.66	1.35	1.09
-11	5.56	5.04	4.58	4.18	3.71	3.31	2.94	2.61	2.20	1.85	1.54	1.27	1.03
-14	5.06	4.59	4.19	3.82	3.40	3.03	2.69	2.40	2.02	1.70	1.43	1.18	0.96
-17	4.51	4.12	3.76	3.44	3.07	2.74	2.44	2.18	1.84	1.55	1.30	1.08	0.88
-20	3.96	3.62	3.32	3.05	2.73	2.44	2.18	1.95	1.66	1.40	1.18	0.98	0.81
-23	3.40	3.12	2.88	2.65	2.38	2.14	1.92	1.72	1.47	1.25	1.06	0.88	0.73
-26	2.88	2.66	2.46	2.27	2.05	1.86	1.67	1.50	1.29	1.11	0.94	0.79	0.65
-28.99	2.42	2.24	2.08	1.94	1.76	1.61	1.45	1.31	1.14	0.98	0.84	0.70	0.58

end-of-cycle wat. case

	33.81	34.79	35.81	36.89	38.04	39.29	40.66	42.19	43.89	45.79	47.94	50.39	53.15
28.99	3.16	2.93	2.71	2.51	2.28	2.06	1.86	1.66	1.44	1.24	1.05	0.88	0.72
26	3.75	3.45	3.18	2.93	2.64	2.37	2.12	1.90	1.63	1.39	1.17	0.97	0.80
23	4.39	4.02	3.69	3.38	3.03	2.71	2.42	2.16	1.84	1.55	1.31	1.08	0.89
20	5.01	4.58	4.18	3.83	3.41	3.04	2.71	2.42	2.04	1.72	1.44	1.19	0.98
17	5.59	5.10	4.65	4.25	3.77	3.36	2.99	2.66	2.24	1.89	1.58	1.30	1.06
14	6.12	5.57	5.07	4.62	4.11	3.65	3.24	2.88	2.43	2.04	1.71	1.41	1.15
11	6.56	5.96	5.44	4.96	4.41	3.93	3.48	3.10	2.61	2.20	1.83	1.50	1.22
8	6.91	6.29	5.74	5.25	4.68	4.17	3.71	3.30	2.79	2.35	1.95	1.59	1.29
5	7.19	6.54	5.98	5.49	4.92	4.40	3.90	3.46	2.92	2.45	2.04	1.66	1.34
2	7.34	6.68	6.11	5.62	5.05	4.52	4.01	3.55	2.99	2.50	2.08	1.70	1.37
0	7.38	6.72	6.15	5.66	5.07	4.55	4.03	3.57	3.00	2.51	2.09	1.71	1.37
-2	7.35	6.69	6.12	5.63	5.05	4.52	4.01	3.55	3.00	2.50	2.08	1.70	1.37
-5	7.22	6.56	6.00	5.50	4.93	4.41	3.91	3.47	2.93	2.46	2.05	1.66	1.34
-8	6.95	6.32	5.76	5.27	4.70	4.19	3.72	3.31	2.79	2.36	1.96	1.60	1.29
-11	6.60	6.00	5.46	4.98	4.43	3.94	3.50	3.11	2.62	2.20	1.84	1.51	1.23
-14	6.16	5.61	5.10	4.66	4.13	3.67	3.27	2.91	2.44	2.05	1.72	1.41	1.15
-17	5.65	5.14	4.69	4.28	3.80	3.38	3.01	2.68	2.25	1.90	1.59	1.31	1.07
-20	5.06	4.62	4.22	3.86	3.44	3.06	2.73	2.43	2.05	1.73	1.45	1.20	0.98
-23	4.43	4.06	3.72	3.41	3.05	2.73	2.44	2.18	1.85	1.57	1.32	1.09	0.90
-26	3.79	3.49	3.21	2.96	2.66	2.39	2.14	1.92	1.64	1.40	1.18	0.98	0.81
-28.99	3.20	2.96	2.74	2.54	2.30	2.08	1.87	1.68	1.46	1.25	1.06	0.88	0.73

Figure 4.7. Water/SST liner case heat deposition rate distribution.

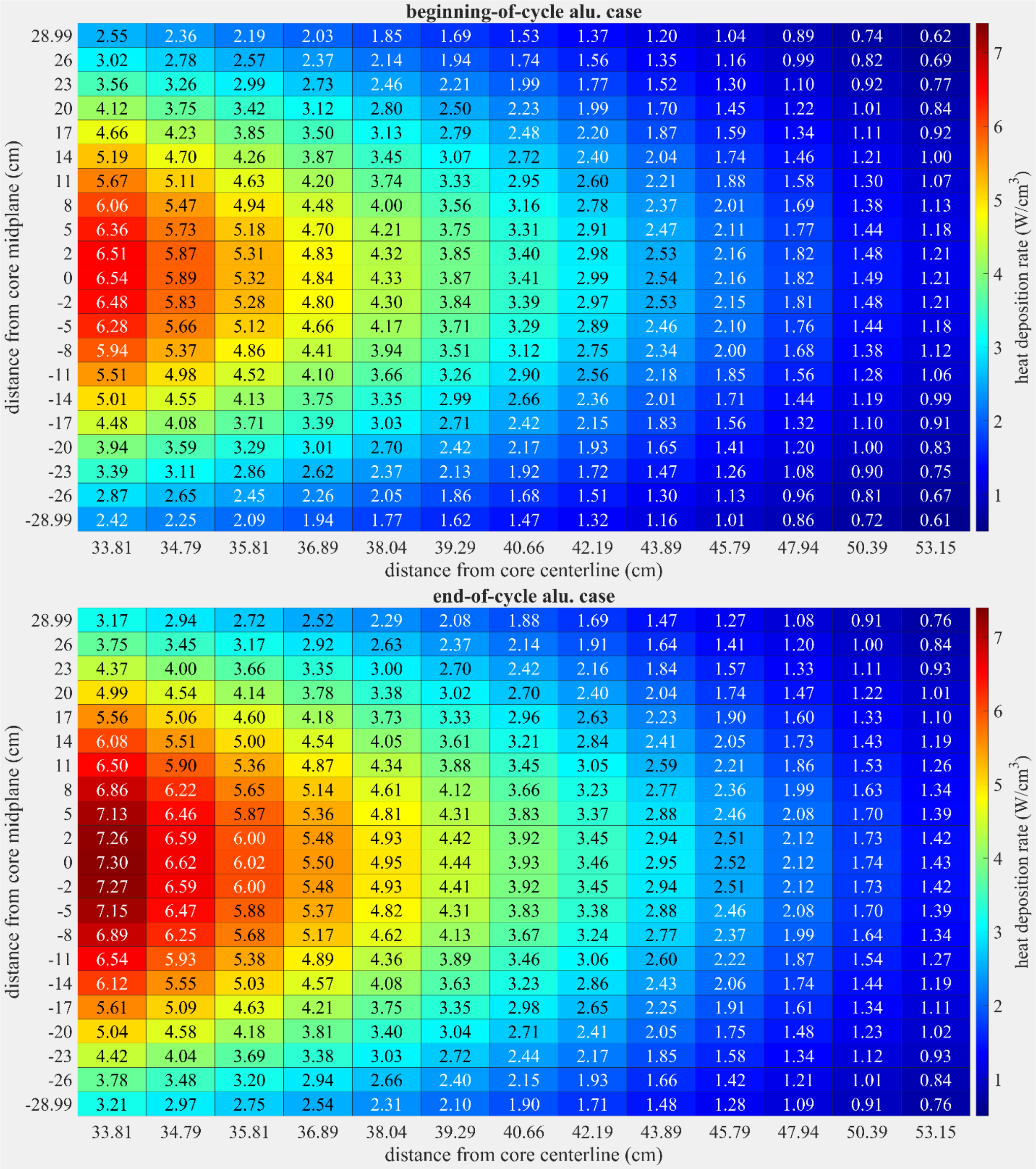

beginning-of-cycle alu. case

	33.81	34.79	35.81	36.89	38.04	39.29	40.66	42.19	43.89	45.79	47.94	50.39	53.15
28.99	2.55	2.36	2.19	2.03	1.85	1.69	1.53	1.37	1.20	1.04	0.89	0.74	0.62
26	3.02	2.78	2.57	2.37	2.14	1.94	1.74	1.56	1.35	1.16	0.99	0.82	0.69
23	3.56	3.26	2.99	2.73	2.46	2.21	1.99	1.77	1.52	1.30	1.10	0.92	0.77
20	4.12	3.75	3.42	3.12	2.80	2.50	2.23	1.99	1.70	1.45	1.22	1.01	0.84
17	4.66	4.23	3.85	3.50	3.13	2.79	2.48	2.20	1.87	1.59	1.34	1.11	0.92
14	5.19	4.70	4.26	3.87	3.45	3.07	2.72	2.40	2.04	1.74	1.46	1.21	1.00
11	5.67	5.11	4.63	4.20	3.74	3.33	2.95	2.60	2.21	1.88	1.58	1.30	1.07
8	6.06	5.47	4.94	4.48	4.00	3.56	3.16	2.78	2.37	2.01	1.69	1.38	1.13
5	6.36	5.73	5.18	4.70	4.21	3.75	3.31	2.91	2.47	2.11	1.77	1.44	1.18
2	6.51	5.87	5.31	4.83	4.32	3.85	3.40	2.98	2.53	2.16	1.82	1.48	1.21
0	6.54	5.89	5.32	4.84	4.33	3.87	3.41	2.99	2.54	2.16	1.82	1.49	1.21
-2	6.48	5.83	5.28	4.80	4.30	3.84	3.39	2.97	2.53	2.15	1.81	1.48	1.21
-5	6.28	5.66	5.12	4.66	4.17	3.71	3.29	2.89	2.46	2.10	1.76	1.44	1.18
-8	5.94	5.37	4.86	4.41	3.94	3.51	3.12	2.75	2.34	2.00	1.68	1.38	1.12
-11	5.51	4.98	4.52	4.10	3.66	3.26	2.90	2.56	2.18	1.85	1.56	1.28	1.06
-14	5.01	4.55	4.13	3.75	3.35	2.99	2.66	2.36	2.01	1.71	1.44	1.19	0.99
-17	4.48	4.08	3.71	3.39	3.03	2.71	2.42	2.15	1.83	1.56	1.32	1.10	0.91
-20	3.94	3.59	3.29	3.01	2.70	2.42	2.17	1.93	1.65	1.41	1.20	1.00	0.83
-23	3.39	3.11	2.86	2.62	2.37	2.13	1.92	1.72	1.47	1.26	1.08	0.90	0.75
-26	2.87	2.65	2.45	2.26	2.05	1.86	1.68	1.51	1.30	1.13	0.96	0.81	0.67
-28.99	2.42	2.25	2.09	1.94	1.77	1.62	1.47	1.32	1.16	1.01	0.86	0.72	0.61

end-of-cycle alu. case

	33.81	34.79	35.81	36.89	38.04	39.29	40.66	42.19	43.89	45.79	47.94	50.39	53.15
28.99	3.17	2.94	2.72	2.52	2.29	2.08	1.88	1.69	1.47	1.27	1.08	0.91	0.76
26	3.75	3.45	3.17	2.92	2.63	2.37	2.14	1.91	1.64	1.41	1.20	1.00	0.84
23	4.37	4.00	3.66	3.35	3.00	2.70	2.42	2.16	1.84	1.57	1.33	1.11	0.93
20	4.99	4.54	4.14	3.78	3.38	3.02	2.70	2.40	2.04	1.74	1.47	1.22	1.01
17	5.56	5.06	4.60	4.18	3.73	3.33	2.96	2.63	2.23	1.90	1.60	1.33	1.10
14	6.08	5.51	5.00	4.54	4.05	3.61	3.21	2.84	2.41	2.05	1.73	1.43	1.19
11	6.50	5.90	5.36	4.87	4.34	3.88	3.45	3.05	2.59	2.21	1.86	1.53	1.26
8	6.86	6.22	5.65	5.14	4.61	4.12	3.66	3.23	2.77	2.36	1.99	1.63	1.34
5	7.13	6.46	5.87	5.36	4.81	4.31	3.83	3.37	2.88	2.46	2.08	1.70	1.39
2	7.26	6.59	6.00	5.48	4.93	4.42	3.92	3.45	2.94	2.51	2.12	1.73	1.42
0	7.30	6.62	6.02	5.50	4.95	4.44	3.93	3.46	2.95	2.52	2.12	1.74	1.43
-2	7.27	6.59	6.00	5.48	4.93	4.41	3.92	3.45	2.94	2.51	2.12	1.73	1.42
-5	7.15	6.47	5.88	5.37	4.82	4.31	3.83	3.38	2.88	2.46	2.08	1.70	1.39
-8	6.89	6.25	5.68	5.17	4.62	4.13	3.67	3.24	2.77	2.37	1.99	1.64	1.34
-11	6.54	5.93	5.38	4.89	4.36	3.89	3.46	3.06	2.60	2.22	1.87	1.54	1.27
-14	6.12	5.55	5.03	4.57	4.08	3.63	3.23	2.86	2.43	2.06	1.74	1.44	1.19
-17	5.61	5.09	4.63	4.21	3.75	3.35	2.98	2.65	2.25	1.91	1.61	1.34	1.11
-20	5.04	4.58	4.18	3.81	3.40	3.04	2.71	2.41	2.05	1.75	1.48	1.23	1.02
-23	4.42	4.04	3.69	3.38	3.03	2.72	2.44	2.17	1.85	1.58	1.34	1.12	0.93
-26	3.78	3.48	3.20	2.94	2.66	2.40	2.15	1.93	1.66	1.42	1.21	1.01	0.84
-28.99	3.21	2.97	2.75	2.54	2.31	2.10	1.90	1.71	1.48	1.28	1.09	0.91	0.76

Figure 4.8. Aluminum plug case heat deposition rate distribution.

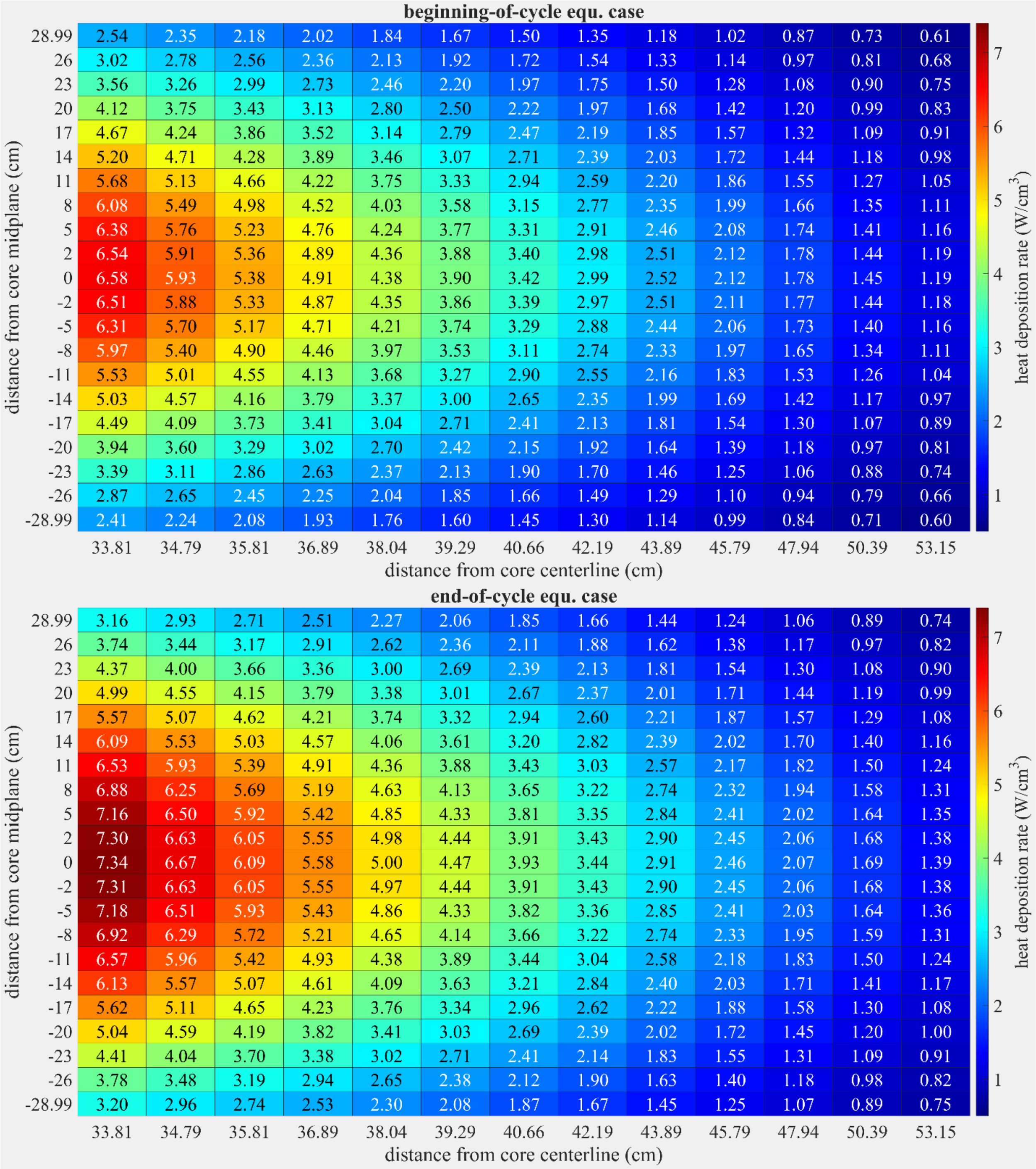

beginning-of-cycle equ. case

distance from core midplane (cm)	33.81	34.79	35.81	36.89	38.04	39.29	40.66	42.19	43.89	45.79	47.94	50.39	53.15
28.99	2.54	2.35	2.18	2.02	1.84	1.67	1.50	1.35	1.18	1.02	0.87	0.73	0.61
26	3.02	2.78	2.56	2.36	2.13	1.92	1.72	1.54	1.33	1.14	0.97	0.81	0.68
23	3.56	3.26	2.99	2.73	2.46	2.20	1.97	1.75	1.50	1.28	1.08	0.90	0.75
20	4.12	3.75	3.43	3.13	2.80	2.50	2.22	1.97	1.68	1.42	1.20	0.99	0.83
17	4.67	4.24	3.86	3.52	3.14	2.79	2.47	2.19	1.85	1.57	1.32	1.09	0.91
14	5.20	4.71	4.28	3.89	3.46	3.07	2.71	2.39	2.03	1.72	1.44	1.18	0.98
11	5.68	5.13	4.66	4.22	3.75	3.33	2.94	2.59	2.20	1.86	1.55	1.27	1.05
8	6.08	5.49	4.98	4.52	4.03	3.58	3.15	2.77	2.35	1.99	1.66	1.35	1.11
5	6.38	5.76	5.23	4.76	4.24	3.77	3.31	2.91	2.46	2.08	1.74	1.41	1.16
2	6.54	5.91	5.36	4.89	4.36	3.88	3.40	2.98	2.51	2.12	1.78	1.44	1.19
0	6.58	5.93	5.38	4.91	4.38	3.90	3.42	2.99	2.52	2.12	1.78	1.45	1.19
-2	6.51	5.88	5.33	4.87	4.35	3.86	3.39	2.97	2.51	2.11	1.77	1.44	1.18
-5	6.31	5.70	5.17	4.71	4.21	3.74	3.29	2.88	2.44	2.06	1.73	1.40	1.16
-8	5.97	5.40	4.90	4.46	3.97	3.53	3.11	2.74	2.33	1.97	1.65	1.34	1.11
-11	5.53	5.01	4.55	4.13	3.68	3.27	2.90	2.55	2.16	1.83	1.53	1.26	1.04
-14	5.03	4.57	4.16	3.79	3.37	3.00	2.65	2.35	1.99	1.69	1.42	1.17	0.97
-17	4.49	4.09	3.73	3.41	3.04	2.71	2.41	2.13	1.81	1.54	1.30	1.07	0.89
-20	3.94	3.60	3.29	3.02	2.70	2.42	2.15	1.92	1.64	1.39	1.18	0.97	0.81
-23	3.39	3.11	2.86	2.63	2.37	2.13	1.90	1.70	1.46	1.25	1.06	0.88	0.74
-26	2.87	2.65	2.45	2.25	2.04	1.85	1.66	1.49	1.29	1.10	0.94	0.79	0.66
-28.99	2.41	2.24	2.08	1.93	1.76	1.60	1.45	1.30	1.14	0.99	0.84	0.71	0.60

end-of-cycle equ. case

distance from core midplane (cm)	33.81	34.79	35.81	36.89	38.04	39.29	40.66	42.19	43.89	45.79	47.94	50.39	53.15
28.99	3.16	2.93	2.71	2.51	2.27	2.06	1.85	1.66	1.44	1.24	1.06	0.89	0.74
26	3.74	3.44	3.17	2.91	2.62	2.36	2.11	1.88	1.62	1.38	1.17	0.97	0.82
23	4.37	4.00	3.66	3.36	3.00	2.69	2.39	2.13	1.81	1.54	1.30	1.08	0.90
20	4.99	4.55	4.15	3.79	3.38	3.01	2.67	2.37	2.01	1.71	1.44	1.19	0.99
17	5.57	5.07	4.62	4.21	3.74	3.32	2.94	2.60	2.21	1.87	1.57	1.29	1.08
14	6.09	5.53	5.03	4.57	4.06	3.61	3.20	2.82	2.39	2.02	1.70	1.40	1.16
11	6.53	5.93	5.39	4.91	4.36	3.88	3.43	3.03	2.57	2.17	1.82	1.50	1.24
8	6.88	6.25	5.69	5.19	4.63	4.13	3.65	3.22	2.74	2.32	1.94	1.58	1.31
5	7.16	6.50	5.92	5.42	4.85	4.33	3.81	3.35	2.84	2.41	2.02	1.64	1.35
2	7.30	6.63	6.05	5.55	4.98	4.44	3.91	3.43	2.90	2.45	2.06	1.68	1.38
0	7.34	6.67	6.09	5.58	5.00	4.47	3.93	3.44	2.91	2.46	2.07	1.69	1.39
-2	7.31	6.63	6.05	5.55	4.97	4.44	3.91	3.43	2.90	2.45	2.06	1.68	1.38
-5	7.18	6.51	5.93	5.43	4.86	4.33	3.82	3.36	2.85	2.41	2.03	1.64	1.36
-8	6.92	6.29	5.72	5.21	4.65	4.14	3.66	3.22	2.74	2.33	1.95	1.59	1.31
-11	6.57	5.96	5.42	4.93	4.38	3.89	3.44	3.04	2.58	2.18	1.83	1.50	1.24
-14	6.13	5.57	5.07	4.61	4.09	3.63	3.21	2.84	2.40	2.03	1.71	1.41	1.17
-17	5.62	5.11	4.65	4.23	3.76	3.34	2.96	2.62	2.22	1.88	1.58	1.30	1.08
-20	5.04	4.59	4.19	3.82	3.41	3.03	2.69	2.39	2.02	1.72	1.45	1.20	1.00
-23	4.41	4.04	3.70	3.38	3.02	2.71	2.41	2.14	1.83	1.55	1.31	1.09	0.91
-26	3.78	3.48	3.19	2.94	2.65	2.38	2.12	1.90	1.63	1.40	1.18	0.98	0.82
-28.99	3.20	2.96	2.74	2.53	2.30	2.08	1.87	1.67	1.45	1.25	1.07	0.89	0.75

Figure 4.9. Equivalent case heat deposition rate distribution.

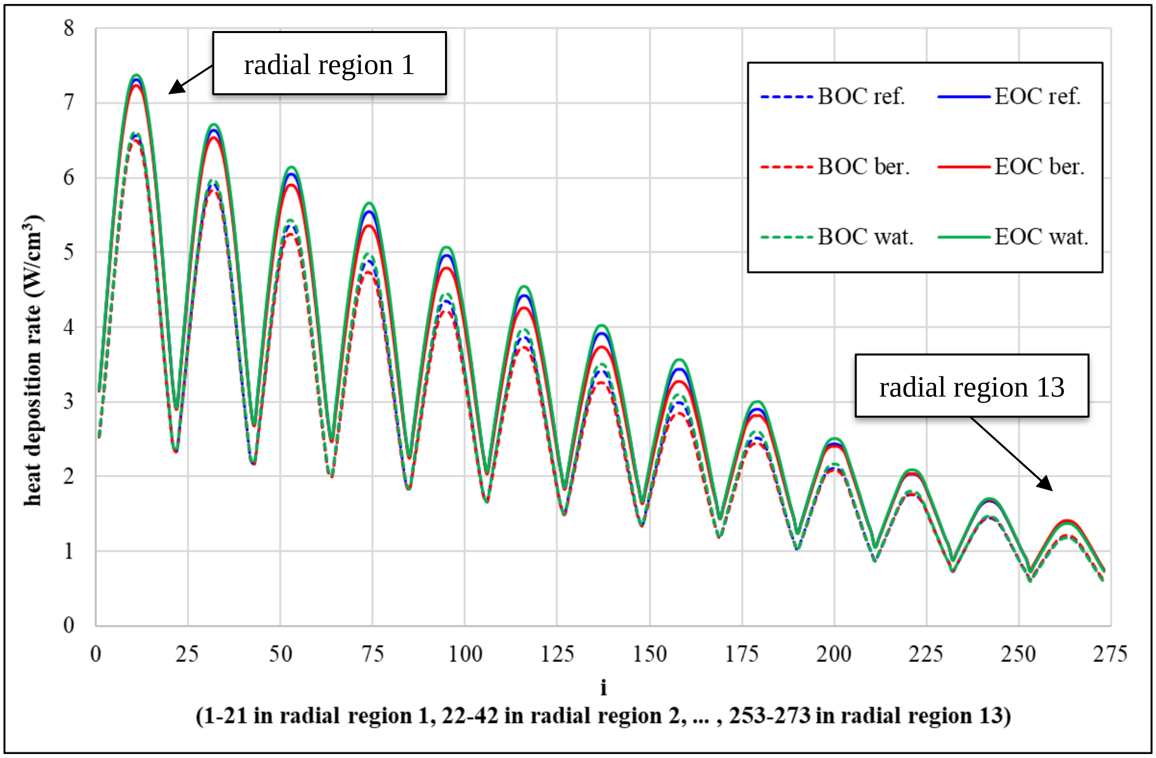

Figure 4.10. PB reflector total volumetric heat deposition rate results.

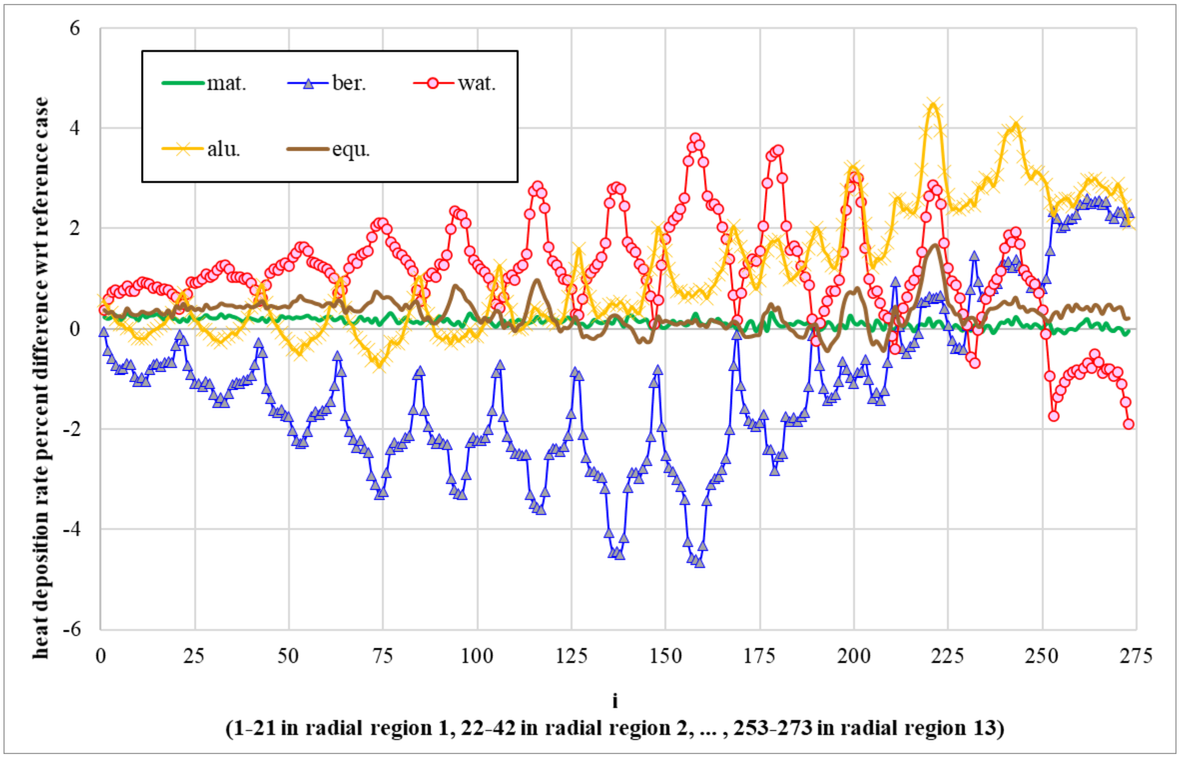

Figure 4.11. EOC PB reflector total heat deposition rate differences relative to reference case.

4.2.3 Fast Fluence

An initial design requirement was established that the reflector be designed for a maximum lifetime fast neutron (E_n > 1 MeV) fluence of 2 × 10^{22} n/cm^2. When ^{9}Be is irradiated by neutrons above ~1 MeV, it undergoes (n,α) and (n,2n) reactions, which results in the generation of gas and neutron poisons. To estimate the fast flux and lifetime fluence at the innermost radius of the PB on the core horizontal midplane, a four-energy group ring detector tally was defined at this location with a radius of 0.5 cm. The upper bounds of the four energy groups were defined as 0.625 eV, 100 keV, 1 MeV, and 20 MeV. The EOL fast fluence, *nvt*, is estimated by extrapolating the state point's flux to an exposure of 279,000 MWd at 85 MW:

$$nvt\left(\frac{n}{cm^2}\right) = \emptyset\left(\frac{n}{cm^2-s}\right)\ 279{,}000\ (MWd)\ \frac{1}{85(MW)}\ 86{,}400\left(\frac{s}{d}\right).$$

Additionally, the exposure at which a fast fluence of 2 × 10^{22} n/cm^2 is estimated using a similar approach:

$$Exp(MWd) = \ 2\times 10^{22}\left(\frac{n}{cm^2}\right)\frac{1}{\emptyset}\left(\frac{cm^2-s}{n}\right)\ 85(MW)\ \frac{d}{86{,}400\ s}.$$

The BOC and EOC fast neutron fluxes and corresponding relative errors are provided in Table 4.8 and Table 4.9. The results of the six cases at each state point are within 1% of each other, and the difference between the BOC and EOC results is less than 2%. Thus, none of the perturbations have an adverse impact on the peak fast flux, peak fast fluence, or expected lifetime based on the 279,000 MWd and 2 × 10^{22} n/cm^2 criteria.

Table 4.8. BOC fast flux and extrapolated fluence.

case	flux (E_n>1 MeV) (n/cm^2-s)	relative error (-)	fluence at EOL (n/cm^2)	difference (%)	MWd at 2×10^{22} n/cm^2
ref.	4.27457E+13	0.0009	1.21212E+22	—	460,350
mat.	4.28154E+13	0.0009	1.21410E+22	0.163	459,600
ber.	4.30038E+13	0.0009	1.21944E+22	0.604	457,587
wat.	4.27553E+13	0.0009	1.21239E+22	0.022	460,248
alu.	4.30575E+13	0.0009	1.22096E+22	0.729	457,017
equ.	4.28479E+13	0.0009	1.21501E+22	0.238	459,255

Table 4.9. EOC fast flux and extrapolated fluence.

case	flux (E_n>1 MeV) (n/cm^2-s)	relative error (-)	fluence at EOL (n/cm^2)	difference (%)	MWd at 2×10^{22} n/cm^2
ref.	4.22190E+13	0.0009	1.19718E+22	—	466,095
mat.	4.21845E+13	0.0009	1.19620E+22	−0.082	466,477
ber.	4.22846E+13	0.0009	1.19904E+22	0.155	465,372
wat.	4.22087E+13	0.0009	1.19689E+22	−0.024	466,208
alu.	4.24385E+13	0.0009	1.20341E+22	0.520	463,682
equ.	4.22827E+13	0.0009	1.19899E+22	0.151	465,392

4.2.4 Nuclear Processes

This section evaluates the nuclear processes that take place in the Be reflector, including multigroup neutron fluxes, cross sections, reaction rates, and transmutations. The primary purpose of this section is to evaluate the impact of the various configurations on gas generation, neutron poison generation, and decay heat in the permanent reflector.

4.2.4.1 44-energy group fluxes

The neutron flux spectrum is calculated in each of the 273 Be cells in the SCALE 44-energy group structure. The group-wise fluxes are used as weighting data in the COUPLE code to generate the one-group cross sections required in ORIGEN, and the total fluxes are used to activate the Be reflector materials (refer to Section 3.6). The reference case neutron flux spectrum for the cells in the innermost and outermost radial regions on the core horizontal midplane are illustrated in Figure 4.12.

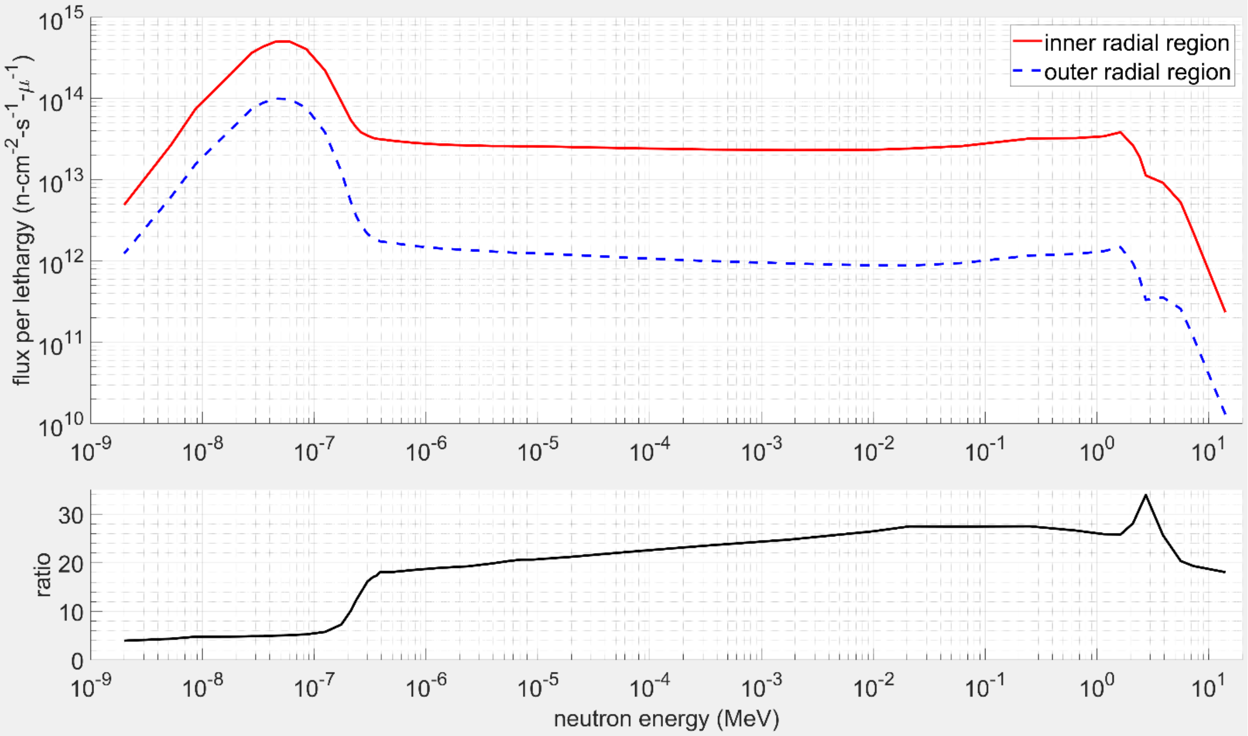

Figure 4.12. Reference case PB reflector neutron flux spectrum at EOC.

Figure 4.13 illustrates the total neutron flux distribution for the reference case permanent reflector. The total neutron flux differences between the perturbed cases and the reference case at EOC are illustrated in Figure 4.14. As expected, the total flux for the Be plug and water/SST liner cases are much greater and much less than that for the reference case, respectively, because of the Be and water nuclear properties. The Al plug case has a lower neutron flux than the reference case in the first ~six radial regions because of reduced neutron reflection (i.e., backscatter) and then becomes greater than the reference case because of the reduced absorption rate in Al. The material change case has trivial impacts on total flux, and the equivalent case yields similar fluxes except for the region around the outer VXFs, which is increased because of the additional Be material resulting from reducing the number of outer small VXFs containing water/SST liners.

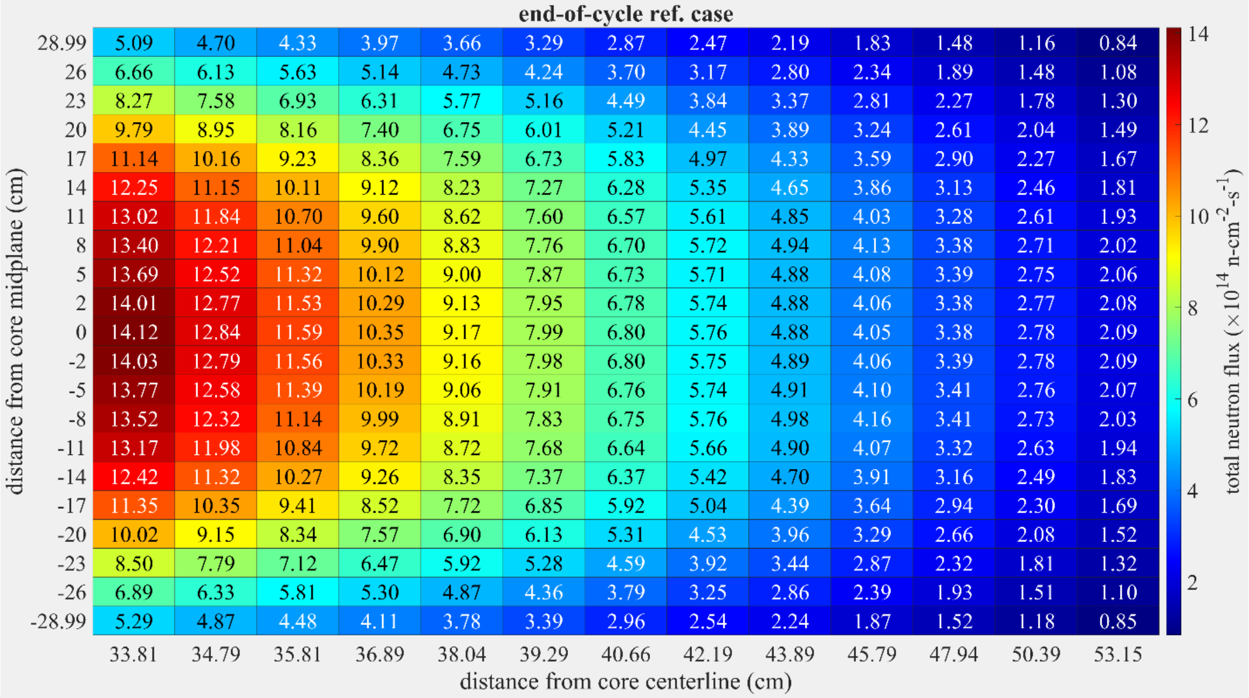

	33.81	34.79	35.81	36.89	38.04	39.29	40.66	42.19	43.89	45.79	47.94	50.39	53.15
28.99	5.09	4.70	4.33	3.97	3.66	3.29	2.87	2.47	2.19	1.83	1.48	1.16	0.84
26	6.66	6.13	5.63	5.14	4.73	4.24	3.70	3.17	2.80	2.34	1.89	1.48	1.08
23	8.27	7.58	6.93	6.31	5.77	5.16	4.49	3.84	3.37	2.81	2.27	1.78	1.30
20	9.79	8.95	8.16	7.40	6.75	6.01	5.21	4.45	3.89	3.24	2.61	2.04	1.49
17	11.14	10.16	9.23	8.36	7.59	6.73	5.83	4.97	4.33	3.59	2.90	2.27	1.67
14	12.25	11.15	10.11	9.12	8.23	7.27	6.28	5.35	4.65	3.86	3.13	2.46	1.81
11	13.02	11.84	10.70	9.60	8.62	7.60	6.57	5.61	4.85	4.03	3.28	2.61	1.93
8	13.40	12.21	11.04	9.90	8.83	7.76	6.70	5.72	4.94	4.13	3.38	2.71	2.02
5	13.69	12.52	11.32	10.12	9.00	7.87	6.73	5.71	4.88	4.08	3.39	2.75	2.06
2	14.01	12.77	11.53	10.29	9.13	7.95	6.78	5.74	4.88	4.06	3.38	2.77	2.08
0	14.12	12.84	11.59	10.35	9.17	7.99	6.80	5.76	4.88	4.05	3.38	2.78	2.09
-2	14.03	12.79	11.56	10.33	9.16	7.98	6.80	5.75	4.89	4.06	3.39	2.78	2.09
-5	13.77	12.58	11.39	10.19	9.06	7.91	6.76	5.74	4.91	4.10	3.41	2.76	2.07
-8	13.52	12.32	11.14	9.99	8.91	7.83	6.75	5.76	4.98	4.16	3.41	2.73	2.03
-11	13.17	11.98	10.84	9.72	8.72	7.68	6.64	5.66	4.90	4.07	3.32	2.63	1.94
-14	12.42	11.32	10.27	9.26	8.35	7.37	6.37	5.42	4.70	3.91	3.16	2.49	1.83
-17	11.35	10.35	9.41	8.52	7.72	6.85	5.92	5.04	4.39	3.64	2.94	2.30	1.69
-20	10.02	9.15	8.34	7.57	6.90	6.13	5.31	4.53	3.96	3.29	2.66	2.08	1.52
-23	8.50	7.79	7.12	6.47	5.92	5.28	4.59	3.92	3.44	2.87	2.32	1.81	1.32
-26	6.89	6.33	5.81	5.30	4.87	4.36	3.79	3.25	2.86	2.39	1.93	1.51	1.10
-28.99	5.29	4.87	4.48	4.11	3.78	3.39	2.96	2.54	2.24	1.87	1.52	1.18	0.85

Figure 4.13. Reference case total neutron flux distribution at EOC.

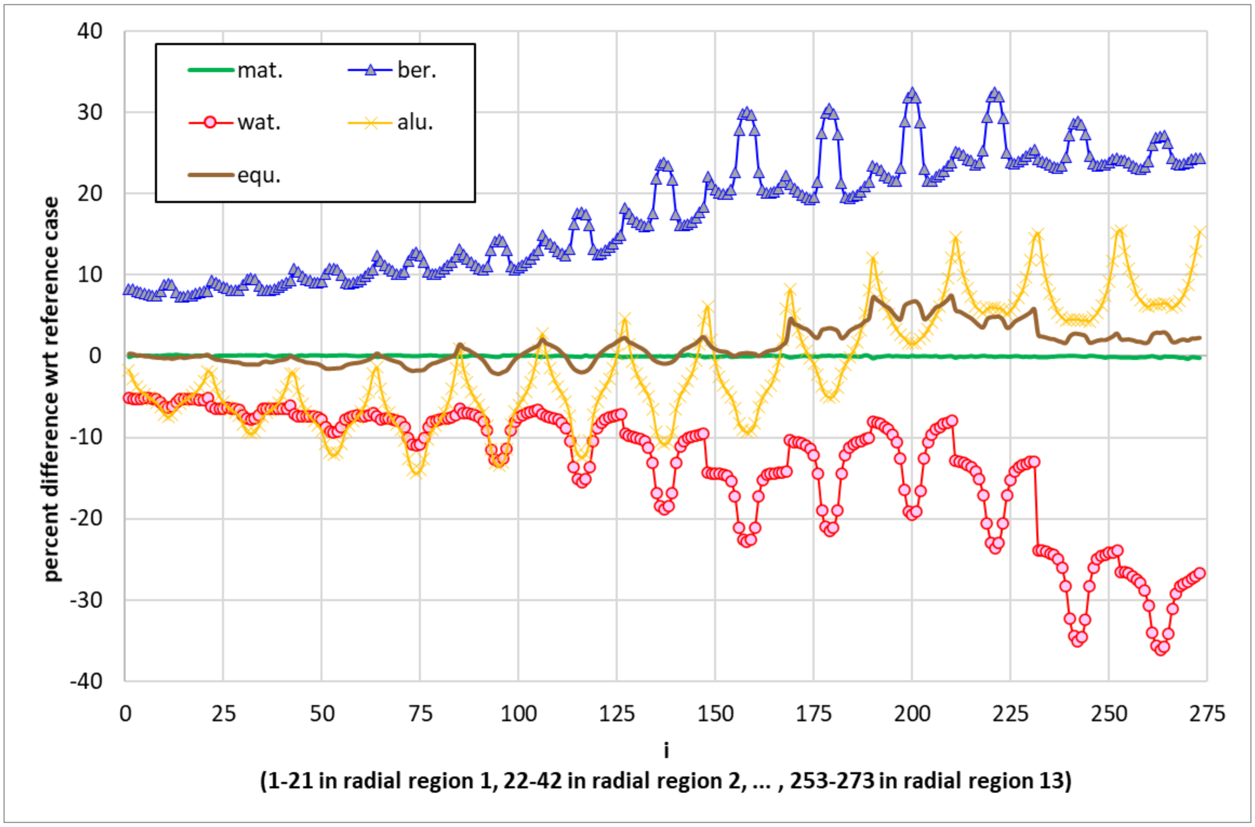

Figure 4.14. Total neutron flux differences at EOC.

4.2.4.2 One-group cross sections and reaction rates

The effective one-group $^{9}Be(n,\alpha)$, $^{9}Be(n,2n)$, ^{9}Be(n,absorption), $^{6}Li(n,t)$, ^{6}Li(n,absorption), $^{3}He(n,p)$, and ^{3}He(n,absorption) reaction rate densities per atom density were calculated in MCNP with a F4:N tally and multipliers including the appropriate MT reaction numbers. Phantom materials were defined for ^{9}Be (m35), ^{6}Li (m36), and ^{3}He (m37). The sd card was again used to define each of the Be cell volumes as unity. Thus, each tally result was multiplied by S_n and divided by its volume to obtain $\sigma(b)\Phi(\#/cm^2\text{-}s)$. The effective one-group cross section is therefore obtained by dividing $\sigma\Phi$ by the total flux, Φ.

$^{9}Be(n,\alpha)$ and $^{9}Be(n,2n)$ reactions are threshold reactions and require neutrons with energies greater than ~1 MeV, whereas $^{6}Li(n,t)$ and $^{3}He(n,p)$ reactions are 1/v. The energy-dependent cross sections for these reactions are provided in Figure 4.15.

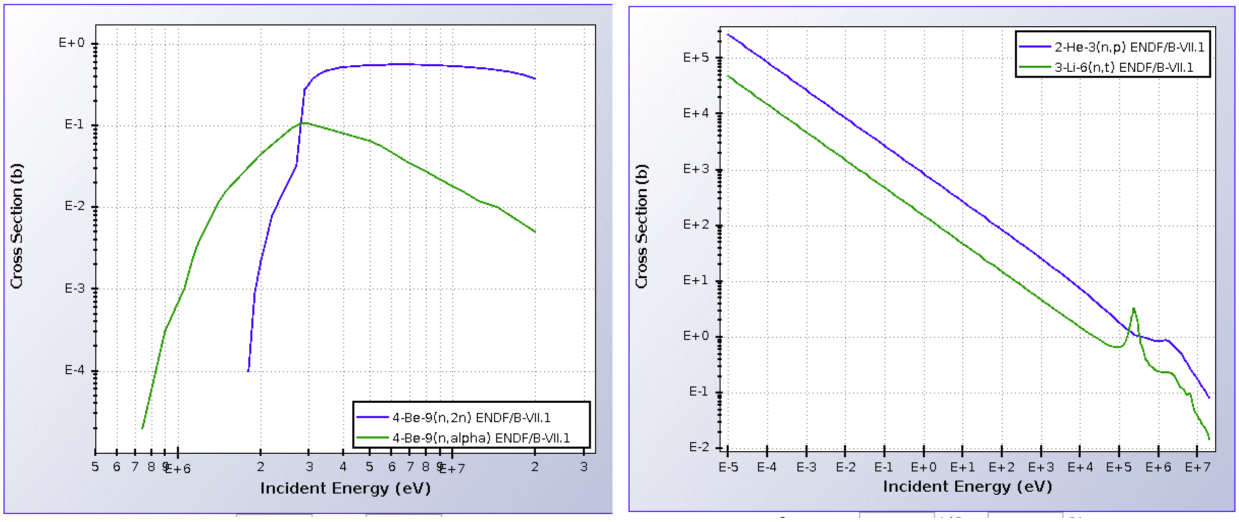

Figure 4.15. Energy-dependent cross section for primary reactions (NNDC 2018).

Differences between the one-group cross sections and reaction rates at EOC are respectively illustrated in Figure 4.16 and Figure 4.17. Cross sections are highly dependent on the neutron flux spectrum, which varies in the reflector depending on the VXF contents modeled. The differences relative to the reference case for the $^{9}Be(n,\alpha)$ and $^{9}Be(n,2n)$ are similar because they are both high-energy threshold reactions. The differences for the $^{6}Li(n,t)$ and $^{3}He(n,p)$ are similar because they are both 1/v absorbers. For reasons similar to those discussed in the previous section, the water/SST liner case Be cross sections are greater than those for the reference case, especially in the outer radial half of the permanent reflector. The Be plug case Be cross sections are less than those of the reference case. The differences between the perturbed and reference $^{6}Li(n,t)$ and $^{3}He(n,p)$ cross sections are relatively small, except for the Al plug case. These cross sections are reduced for the Al plug case because Al has a trivial scattering cross section relative to water and Be.

The differences between the perturbed and reference $^{9}Be(n,\alpha)$ and $^{9}Be(n,2n)$ $\sigma\Phi$ results are relatively small, except for the Al plug case because of the reasons previously stated. Consistent with the total flux and $^{6}Li(n,t)$ and $^{3}He(n,p)$ cross section results, the water/SST liner case $^{6}Li(n,t)$ and $^{3}He(n,p)$ $\sigma\Phi$ results are less than those of the reference case, especially in the outer radial half of the permanent reflector. Conversely, the Be plug case $^{6}Li(n,t)$ and $^{3}He(n,p)$ $\sigma\Phi$ results are greater those of the reference case.

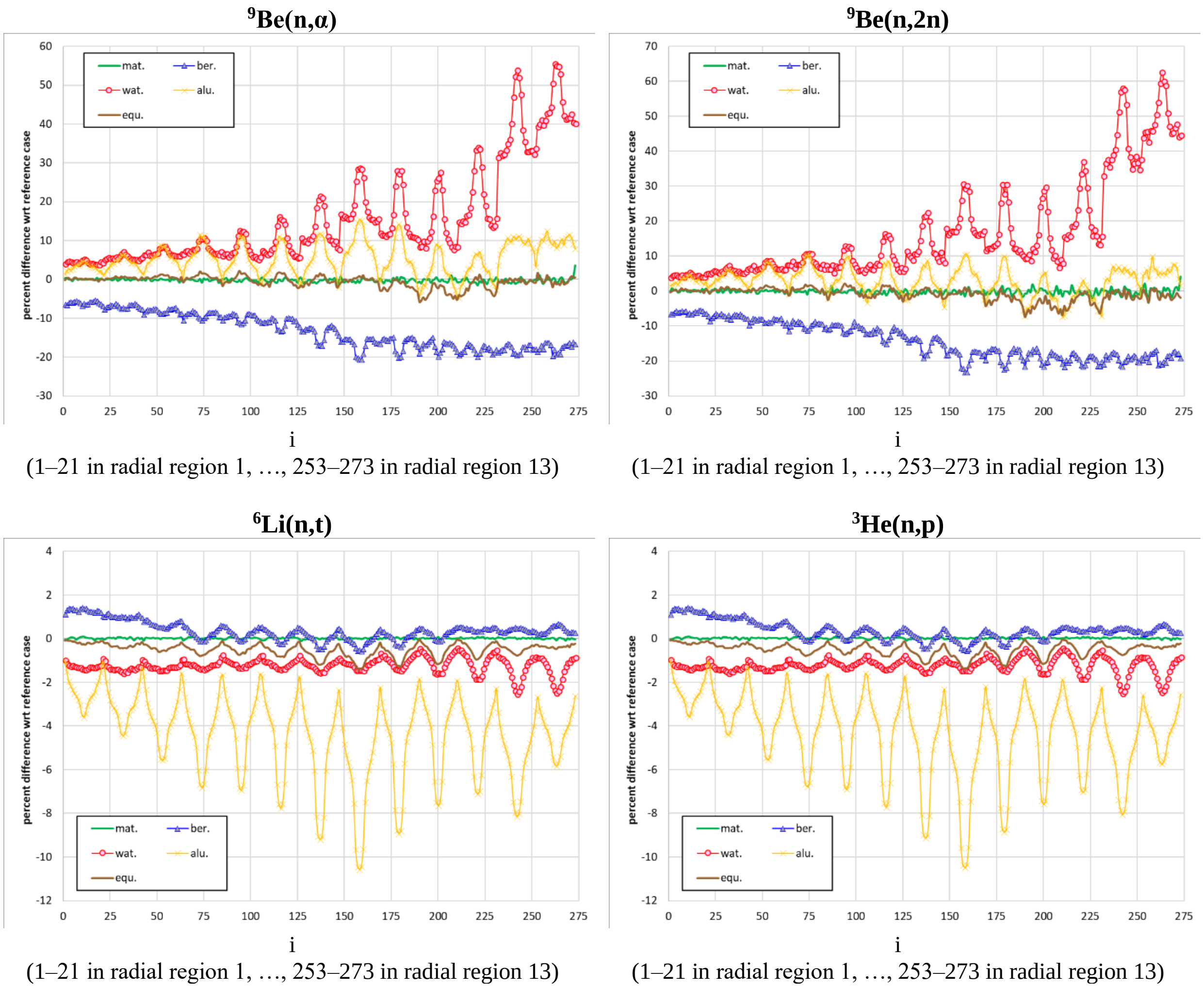

^{9}Be(n,α)

^{9}Be(n,2n)

^{6}Li(n,t)

^{3}He(n,p)

Figure 4.16. EOC cross section differences relative to reference case.

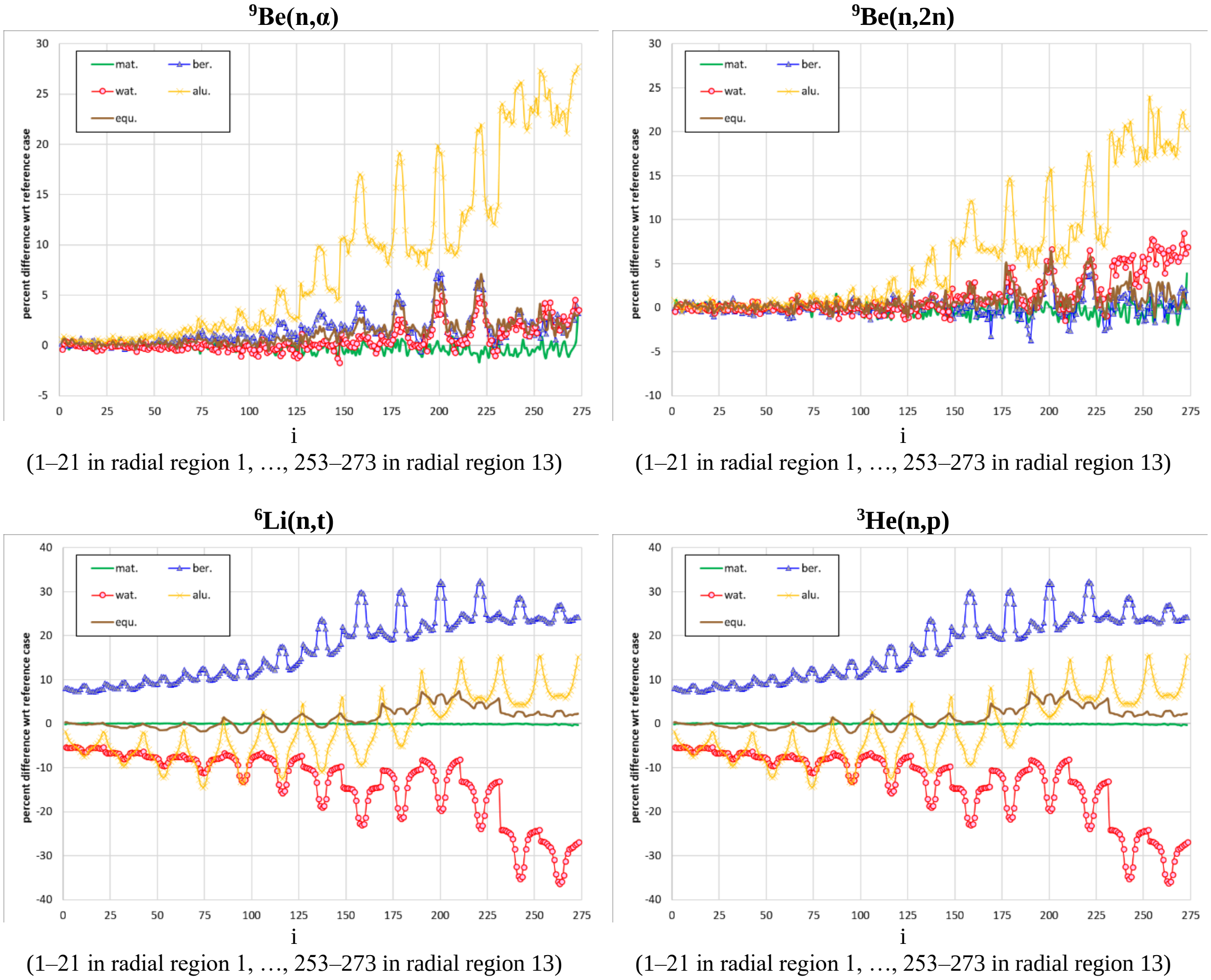

Figure 4.17. EOC reaction rate (σΦ) differences with respect to reference case.

4.2.4.3 Activation

Activation calculations were performed utilizing the 44-energy group fluxes and one-group cross sections discussed in the two previous sections and the methods discussed in Section 3.6. Calculations were performed for the materials located on the core horizontal midplane only, and the results are based on using either the BOC or EOC fluxes and cross sections for the entire simulation. The simulations consisted of 132 cycles, including 25 d irradiation cycles and 25 d outages (6,600 d simulation). Time steps including 1, 3, 5, 10, 15, 20, and 25 d into each of the irradiation and decay periods were used.

The ^{3}H, ^{3}He, ^{4}He, and ^{6}Li densities calculated for the reference case midplane inner radial edge mesh cell are provided in Figure 4.18. The variation of ^{3}He is very dependent on the assumed irradiation and decay history because it is generated and depleted during irradiation, but it is generated only during an outage. Table 4.10–Table 4.17 list the maximum calculated nuclide densities for all midplane mesh cells for all cases modeled. The percent differences between the perturbed and reference cases are also provided in these tables and are illustrated in Figure 4.19. The results are consistent with the discussions provided in the two previous sections.

Helium-4 is the primary gaseous He isotope, and 2.40 mg/cm^3 is the maximum calculated density for the various cases analyzed. Using an atomic weight of 4.002603 (NIST 2018) and the initial concept Be atom density of 0.123476 at/b-cm, the maximum calculated ^{4}He atom percent is estimated to be 0.29 at %.

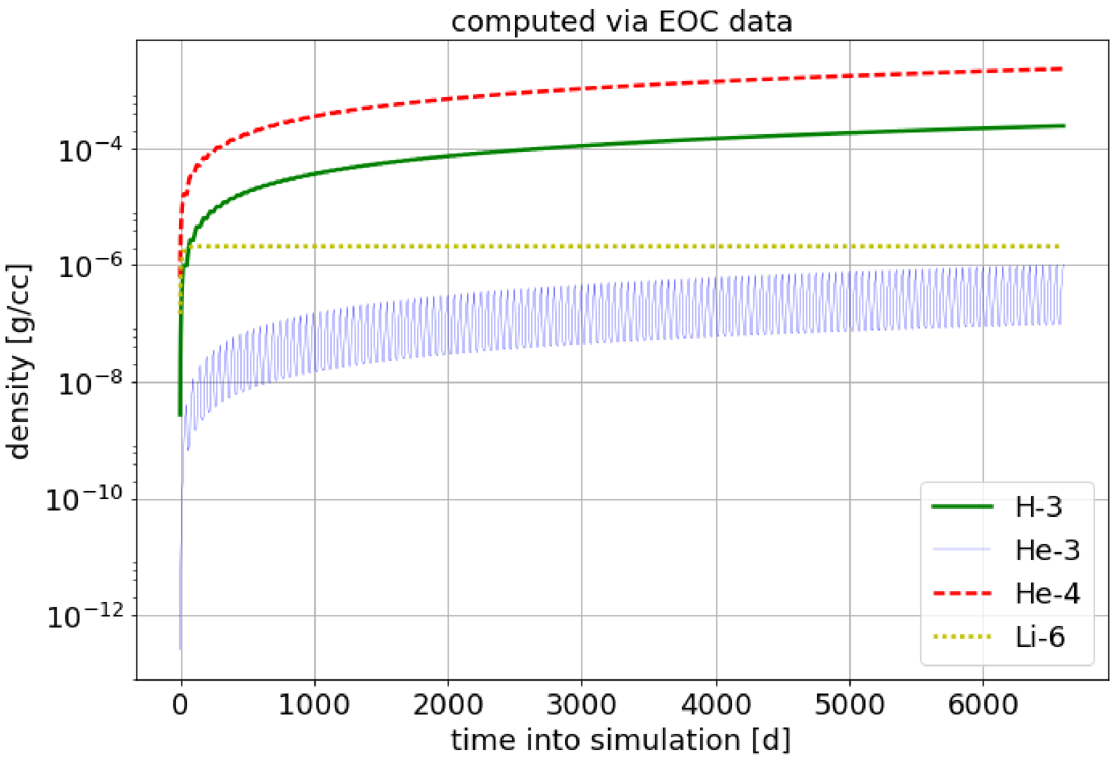

Figure 4.18. Gas and poison variation with time for the reference case midplane inner edge mesh cell.

Table 4.10. Max midplane ^{3}H density computed with BOC data.

r_c (cm)	^{3}H (g/cm^3)						percent difference wrt reference case				
	ref.	mat.	ber.	wat.	alu.	equ.	mat.	ber.	wat.	alu.	equ.
33.81250	2.489E-04	2.501E-04	2.508E-04	2.509E-04	2.525E-04	2.493E-04	0.48	0.76	0.80	1.45	0.16
34.78750	2.049E-04	2.058E-04	2.069E-04	2.058E-04	2.074E-04	2.047E-04	0.44	0.98	0.44	1.22	−0.10
35.81250	1.661E-04	1.667E-04	1.670E-04	1.659E-04	1.687E-04	1.670E-04	0.36	0.54	−0.12	1.57	0.54
36.88750	1.329E-04	1.337E-04	1.355E-04	1.336E-04	1.366E-04	1.348E-04	0.60	1.96	0.53	2.78	1.43
38.03750	1.043E-04	1.051E-04	1.068E-04	1.044E-04	1.084E-04	1.053E-04	0.77	2.40	0.10	3.93	0.96
39.28750	8.091E-05	8.125E-05	8.318E-05	8.094E-05	8.522E-05	8.185E-05	0.42	2.81	0.04	5.33	1.16
40.66250	6.148E-05	6.169E-05	6.352E-05	6.157E-05	6.758E-05	6.241E-05	0.34	3.32	0.15	9.92	1.51
42.18750	4.713E-05	4.718E-05	4.914E-05	4.753E-05	5.483E-05	4.827E-05	0.11	4.27	0.85	16.34	2.42
43.88750	3.448E-05	3.471E-05	3.632E-05	3.529E-05	4.079E-05	3.594E-05	0.67	5.34	2.35	18.30	4.23
45.78750	2.479E-05	2.486E-05	2.702E-05	2.571E-05	3.057E-05	2.674E-05	0.28	9.00	3.71	23.32	7.87
47.93750	1.829E-05	1.838E-05	2.006E-05	1.918E-05	2.279E-05	1.980E-05	0.49	9.68	4.87	24.60	8.26
50.38750	1.329E-05	1.316E-05	1.396E-05	1.342E-05	1.688E-05	1.373E-05	−0.98	5.04	0.98	27.01	3.31
53.14875	8.892E-06	8.788E-06	9.084E-06	8.825E-06	1.093E-05	9.053E-06	−1.17	2.16	−0.75	22.92	1.81

Table 4.11. Max midplane ^{3}H density computed with EOC data.

r_c (cm)	^{3}H (g/cm^3)						percent difference wrt reference case				
	ref.	mat.	ber.	wat.	alu.	equ.	mat.	ber.	wat.	alu.	equ.
33.81250	2.448E-04	2.458E-04	2.476E-04	2.459E-04	2.467E-04	2.456E-04	0.41	1.14	0.45	0.78	0.33
34.78750	2.020E-04	2.040E-04	2.039E-04	2.033E-04	2.038E-04	2.027E-04	0.99	0.94	0.64	0.89	0.35
35.81250	1.644E-04	1.650E-04	1.660E-04	1.643E-04	1.661E-04	1.655E-04	0.37	0.97	−0.06	1.03	0.67
36.88750	1.323E-04	1.316E-04	1.340E-04	1.323E-04	1.348E-04	1.335E-04	−0.53	1.29	0.00	1.89	0.91
38.03750	1.040E-04	1.036E-04	1.058E-04	1.032E-04	1.073E-04	1.044E-04	−0.38	1.73	−0.77	3.17	0.38
39.28750	8.043E-05	8.029E-05	8.247E-05	7.979E-05	8.449E-05	8.113E-05	−0.17	2.54	−0.80	5.05	0.87
40.66250	6.121E-05	6.121E-05	6.358E-05	6.144E-05	6.733E-05	6.255E-05	0.00	3.87	0.38	10.00	2.19
42.18750	4.713E-05	4.685E-05	4.918E-05	4.753E-05	5.525E-05	4.856E-05	−0.59	4.35	0.85	17.23	3.03
43.88750	3.471E-05	3.461E-05	3.652E-05	3.521E-05	4.146E-05	3.627E-05	−0.29	5.22	1.44	19.45	4.49
45.78750	2.513E-05	2.515E-05	2.688E-05	2.594E-05	3.004E-05	2.660E-05	0.08	6.96	3.22	19.54	5.85
47.93750	1.865E-05	1.839E-05	1.986E-05	1.942E-05	2.270E-05	1.979E-05	−1.39	6.49	4.13	21.72	6.11
50.38750	1.333E-05	1.326E-05	1.386E-05	1.358E-05	1.685E-05	1.383E-05	−0.53	3.98	1.88	26.41	3.75
53.14875	8.870E-06	8.801E-06	9.119E-06	8.918E-06	1.089E-05	9.088E-06	−0.78	2.81	0.54	22.77	2.46

Table 4.12. Max midplane ^{3}He density computed with BOC data.

r_c (cm)	^{3}He (g/cm^3)						percent difference wrt reference case				
	ref.	mat.	ber.	wat.	alu.	equ.	mat.	ber.	wat.	alu.	equ.
33.81250	1.083E-06	1.088E-06	1.081E-06	1.101E-06	1.110E-06	1.084E-06	0.46	−0.18	1.66	2.49	0.09
34.78750	8.983E-07	9.020E-07	8.970E-07	9.126E-07	9.225E-07	8.989E-07	0.41	−0.14	1.59	2.69	0.07
35.81250	7.346E-07	7.376E-07	7.290E-07	7.443E-07	7.619E-07	7.402E-07	0.41	−0.76	1.32	3.72	0.76
36.88750	5.948E-07	5.978E-07	5.966E-07	6.087E-07	6.284E-07	6.044E-07	0.50	0.30	2.34	5.65	1.61
38.03750	4.730E-07	4.765E-07	4.750E-07	4.855E-07	5.063E-07	4.793E-07	0.74	0.42	2.64	7.04	1.33
39.28750	3.740E-07	3.757E-07	3.745E-07	3.874E-07	4.063E-07	3.798E-07	0.45	0.13	3.58	8.64	1.55
40.66250	2.920E-07	2.930E-07	2.900E-07	3.078E-07	3.317E-07	2.971E-07	0.34	−0.68	5.41	13.60	1.75
42.18750	2.314E-07	2.318E-07	2.281E-07	2.522E-07	2.793E-07	2.370E-07	0.17	−1.43	8.99	20.70	2.42
43.88750	1.761E-07	1.773E-07	1.736E-07	1.962E-07	2.137E-07	1.821E-07	0.68	−1.42	11.41	21.35	3.41
45.78750	1.338E-07	1.342E-07	1.340E-07	1.518E-07	1.654E-07	1.413E-07	0.30	0.15	13.45	23.62	5.61
47.93750	1.053E-07	1.058E-07	1.043E-07	1.255E-07	1.290E-07	1.119E-07	0.47	−0.95	19.18	22.51	6.27
50.38750	8.299E-08	8.219E-08	7.817E-08	1.069E-07	1.041E-07	8.463E-08	−0.96	−5.81	28.81	25.44	1.98
53.14875	6.358E-08	6.281E-08	5.726E-08	8.410E-08	7.588E-08	6.365E-08	−1.21	−9.94	32.27	19.35	0.11

Table 4.13. Max midplane ^{3}He density computed with EOC data.

r_c (cm)	^{3}He (g/cm^3)						percent difference wrt reference case				
	ref.	**mat.**	**ber.**	**wat.**	**alu.**	**equ.**	**mat.**	**ber.**	**wat.**	**alu.**	**equ.**
33.81250	1.038E-06	1.042E-06	1.042E-06	1.050E-06	1.054E-06	1.042E-06	0.39	0.39	1.16	1.54	0.39
34.78750	8.623E-07	8.709E-07	8.629E-07	8.753E-07	8.790E-07	8.660E-07	1.00	0.07	1.51	1.94	0.43
35.81250	7.070E-07	7.094E-07	7.067E-07	7.149E-07	7.255E-07	7.132E-07	0.34	−0.04	1.12	2.62	0.88
36.88750	5.745E-07	5.714E-07	5.744E-07	5.830E-07	5.973E-07	5.809E-07	−0.54	−0.02	1.48	3.97	1.11
38.03750	4.574E-07	4.555E-07	4.573E-07	4.628E-07	4.814E-07	4.601E-07	−0.42	−0.02	1.18	5.25	0.59
39.28750	3.591E-07	3.587E-07	3.603E-07	3.664E-07	3.853E-07	3.634E-07	−0.11	0.33	2.03	7.30	1.20
40.66250	2.794E-07	2.796E-07	2.809E-07	2.924E-07	3.140E-07	2.861E-07	0.07	0.54	4.65	12.38	2.40
42.18750	2.214E-07	2.200E-07	2.203E-07	2.380E-07	2.652E-07	2.279E-07	−0.63	−0.50	7.50	19.78	2.94
43.88750	1.684E-07	1.679E-07	1.675E-07	1.832E-07	2.038E-07	1.745E-07	−0.30	−0.53	8.79	21.02	3.62
45.78750	1.276E-07	1.277E-07	1.269E-07	1.420E-07	1.518E-07	1.325E-07	0.08	−0.55	11.29	18.97	3.84
47.93750	9.998E-08	9.863E-08	9.746E-08	1.165E-07	1.191E-07	1.043E-07	−1.35	−2.52	16.52	19.12	4.32
50.38750	7.658E-08	7.619E-08	7.221E-08	9.746E-08	9.492E-08	7.850E-08	−0.51	−5.71	27.27	23.95	2.51
53.14875	5.739E-08	5.702E-08	5.255E-08	7.575E-08	6.816E-08	5.793E-08	−0.64	−8.43	31.99	18.77	0.94

Table 4.14. Max midplane ^{4}He density computed with BOC data.

r_c (cm)	^{4}He (g/cm^3)						percent difference wrt reference case				
	ref.	**mat.**	**ber.**	**wat.**	**alu.**	**equ.**	**mat.**	**ber.**	**wat.**	**alu.**	**equ.**
33.81250	2.368E-03	2.372E-03	2.381E-03	2.388E-03	2.399E-03	2.370E-03	0.17	0.55	0.84	1.31	0.08
34.78750	1.954E-03	1.962E-03	1.969E-03	1.962E-03	1.975E-03	1.948E-03	0.41	0.77	0.41	1.08	−0.31
35.81250	1.590E-03	1.603E-03	1.597E-03	1.591E-03	1.613E-03	1.597E-03	0.82	0.44	0.06	1.45	0.44
36.88750	1.283E-03	1.295E-03	1.297E-03	1.292E-03	1.307E-03	1.296E-03	0.94	1.09	0.70	1.87	1.01
38.03750	1.014E-03	1.016E-03	1.022E-03	1.015E-03	1.039E-03	1.021E-03	0.20	0.79	0.10	2.47	0.69
39.28750	7.927E-04	7.906E-04	8.015E-04	7.915E-04	8.131E-04	8.002E-04	−0.26	1.11	−0.15	2.57	0.95
40.66250	6.078E-04	6.083E-04	6.147E-04	6.078E-04	6.492E-04	6.158E-04	0.08	1.14	0.00	6.81	1.32
42.18750	4.730E-04	4.730E-04	4.794E-04	4.847E-04	5.322E-04	4.823E-04	0.00	1.35	2.47	12.52	1.97
43.88750	3.479E-04	3.506E-04	3.572E-04	3.636E-04	4.003E-04	3.614E-04	0.78	2.67	4.51	15.06	3.88
45.78750	2.543E-04	2.536E-04	2.703E-04	2.635E-04	3.030E-04	2.705E-04	−0.28	6.29	3.62	19.15	6.37
47.93750	1.899E-04	1.907E-04	2.037E-04	2.013E-04	2.281E-04	2.035E-04	0.42	7.27	6.00	20.12	7.16
50.38750	1.397E-04	1.390E-04	1.441E-04	1.466E-04	1.716E-04	1.450E-04	−0.50	3.15	4.94	22.83	3.79
53.14875	9.676E-05	9.555E-05	9.667E-05	9.940E-05	1.144E-04	9.912E-05	−1.25	−0.09	2.73	18.23	2.44

Table 4.15. Max midplane ^{4}He density computed with EOC data.

r_c (cm)	^{4}He (g/cm^{3})						percent difference wrt reference case				
	ref.	mat.	ber.	wat.	alu.	equ.	mat.	ber.	wat.	alu.	equ.
33.81250	2.321E-03	2.326E-03	2.345E-03	2.333E-03	2.341E-03	2.331E-03	0.22	1.03	0.52	0.86	0.43
34.78750	1.918E-03	1.939E-03	1.943E-03	1.934E-03	1.933E-03	1.931E-03	1.10	1.30	0.83	0.78	0.68
35.81250	1.568E-03	1.573E-03	1.582E-03	1.570E-03	1.581E-03	1.579E-03	0.32	0.89	0.13	0.83	0.70
36.88750	1.270E-03	1.261E-03	1.278E-03	1.273E-03	1.290E-03	1.280E-03	−0.71	0.63	0.24	1.58	0.79
38.03750	1.001E-03	9.972E-04	1.015E-03	9.954E-04	1.027E-03	1.004E-03	−0.38	1.40	−0.56	2.60	0.30
39.28750	7.810E-04	7.742E-04	7.887E-04	7.766E-04	8.042E-04	7.871E-04	−0.87	0.99	−0.56	2.97	0.78
40.66250	6.019E-04	5.992E-04	6.164E-04	6.055E-04	6.422E-04	6.125E-04	−0.45	2.41	0.60	6.70	1.76
42.18750	4.693E-04	4.639E-04	4.769E-04	4.761E-04	5.339E-04	4.839E-04	−1.15	1.62	1.45	13.77	3.11
43.88750	3.493E-04	3.481E-04	3.585E-04	3.567E-04	4.061E-04	3.647E-04	−0.34	2.63	2.12	16.26	4.41
45.78750	2.552E-04	2.560E-04	2.680E-04	2.681E-04	2.974E-04	2.678E-04	0.31	5.02	5.06	16.54	4.94
47.93750	1.920E-04	1.897E-04	2.008E-04	2.040E-04	2.282E-04	2.025E-04	−1.20	4.58	6.25	18.85	5.47
50.38750	1.403E-04	1.386E-04	1.426E-04	1.471E-04	1.710E-04	1.441E-04	−1.21	1.64	4.85	21.88	2.71
53.14875	9.500E-05	9.378E-05	9.566E-05	1.003E-04	1.138E-04	9.780E-05	−1.28	0.69	5.58	19.79	2.95

Table 4.16. Max midplane ^{6}Li density computed with BOC data.

r_c (cm)	^{6}Li (g/cm^{3})						percent difference wrt reference case				
	ref.	mat.	ber.	wat.	alu.	equ.	mat.	ber.	wat.	alu.	equ.
33.81250	2.746E-06	2.759E-06	2.541E-06	2.960E-06	3.031E-06	2.760E-06	0.47	−7.47	7.79	10.38	0.51
34.78750	2.405E-06	2.415E-06	2.222E-06	2.627E-06	2.717E-06	2.432E-06	0.42	−7.61	9.23	12.97	1.12
35.81250	2.086E-06	2.093E-06	1.899E-06	2.306E-06	2.441E-06	2.133E-06	0.34	−8.97	10.55	17.02	2.25
36.88750	1.805E-06	1.815E-06	1.643E-06	2.041E-06	2.197E-06	1.865E-06	0.55	−8.98	13.07	21.72	3.32
38.03750	1.549E-06	1.561E-06	1.398E-06	1.782E-06	1.890E-06	1.600E-06	0.77	−9.75	15.04	22.01	3.29
39.28750	1.339E-06	1.345E-06	1.179E-06	1.584E-06	1.640E-06	1.382E-06	0.45	−11.95	18.30	22.48	3.21
40.66250	1.160E-06	1.163E-06	9.807E-07	1.427E-06	1.466E-06	1.190E-06	0.26	−15.46	23.02	26.38	2.59
42.18750	1.022E-06	1.024E-06	8.328E-07	1.330E-06	1.355E-06	1.047E-06	0.20	−18.51	30.14	32.58	2.45
43.88750	8.588E-07	8.635E-07	7.055E-07	1.118E-06	1.100E-06	8.712E-07	0.55	−17.85	30.18	28.09	1.44
45.78750	7.269E-07	7.285E-07	6.073E-07	9.388E-07	9.029E-07	7.385E-07	0.22	−16.45	29.15	24.21	1.60
47.93750	6.309E-07	6.336E-07	5.276E-07	8.657E-07	7.558E-07	6.529E-07	0.43	−16.37	37.22	19.80	3.49
50.38750	5.466E-07	5.416E-07	4.500E-07	8.500E-07	6.769E-07	5.496E-07	-0.91	−17.67	55.51	23.84	0.55
53.14875	4.702E-07	4.643E-07	3.800E-07	7.324E-07	5.496E-07	4.648E-07	-1.26	−19.18	55.76	16.89	−1.15

Table 4.17. Max midplane ^{6}Li density computed with EOC data.

r_c (cm)	^{6}Li (g/cm^{3})						percent difference wrt reference case				
	ref.	mat.	ber.	wat.	alu.	equ.	mat.	ber.	wat.	alu.	equ.
33.81250	2.118E-06	2.123E-06	1.967E-06	2.271E-06	2.306E-06	2.129E-06	0.24	−7.13	7.22	8.88	0.52
34.78750	1.873E-06	1.890E-06	1.726E-06	2.046E-06	2.089E-06	1.898E-06	0.91	−7.85	9.24	11.53	1.34
35.81250	1.642E-06	1.647E-06	1.495E-06	1.812E-06	1.890E-06	1.678E-06	0.30	−8.95	10.35	15.10	2.19
36.88750	1.438E-06	1.430E-06	1.292E-06	1.617E-06	1.713E-06	1.476E-06	-0.56	−10.15	12.45	19.12	2.64
38.03750	1.246E-06	1.242E-06	1.107E-06	1.422E-06	1.487E-06	1.277E-06	-0.32	−11.16	14.13	19.34	2.49
39.28750	1.081E-06	1.080E-06	9.409E-07	1.271E-06	1.297E-06	1.112E-06	-0.09	−12.96	17.58	19.98	2.87
40.66250	9.456E-07	9.466E-07	7.924E-07	1.172E-06	1.167E-06	9.756E-07	0.11	−16.20	23.94	23.41	3.17
42.18750	8.441E-07	8.396E-07	6.755E-07	1.106E-06	1.093E-06	8.659E-07	-0.53	−19.97	31.03	29.49	2.58
43.88750	7.174E-07	7.146E-07	5.770E-07	9.286E-07	9.024E-07	7.241E-07	-0.39	−19.57	29.44	25.79	0.93
45.78750	6.134E-07	6.134E-07	4.939E-07	7.894E-07	7.219E-07	6.084E-07	0.00	−19.48	28.69	17.69	−0.82
47.93750	5.360E-07	5.292E-07	4.292E-07	7.349E-07	6.149E-07	5.422E-07	-1.27	−19.93	37.11	14.72	1.16
50.38750	4.569E-07	4.546E-07	3.668E-07	7.239E-07	5.519E-07	4.607E-07	-0.50	−19.72	58.44	20.79	0.83
53.14875	3.907E-07	3.886E-07	3.146E-07	6.232E-07	4.498E-07	3.888E-07	-0.54	−19.48	59.51	15.13	−0.49

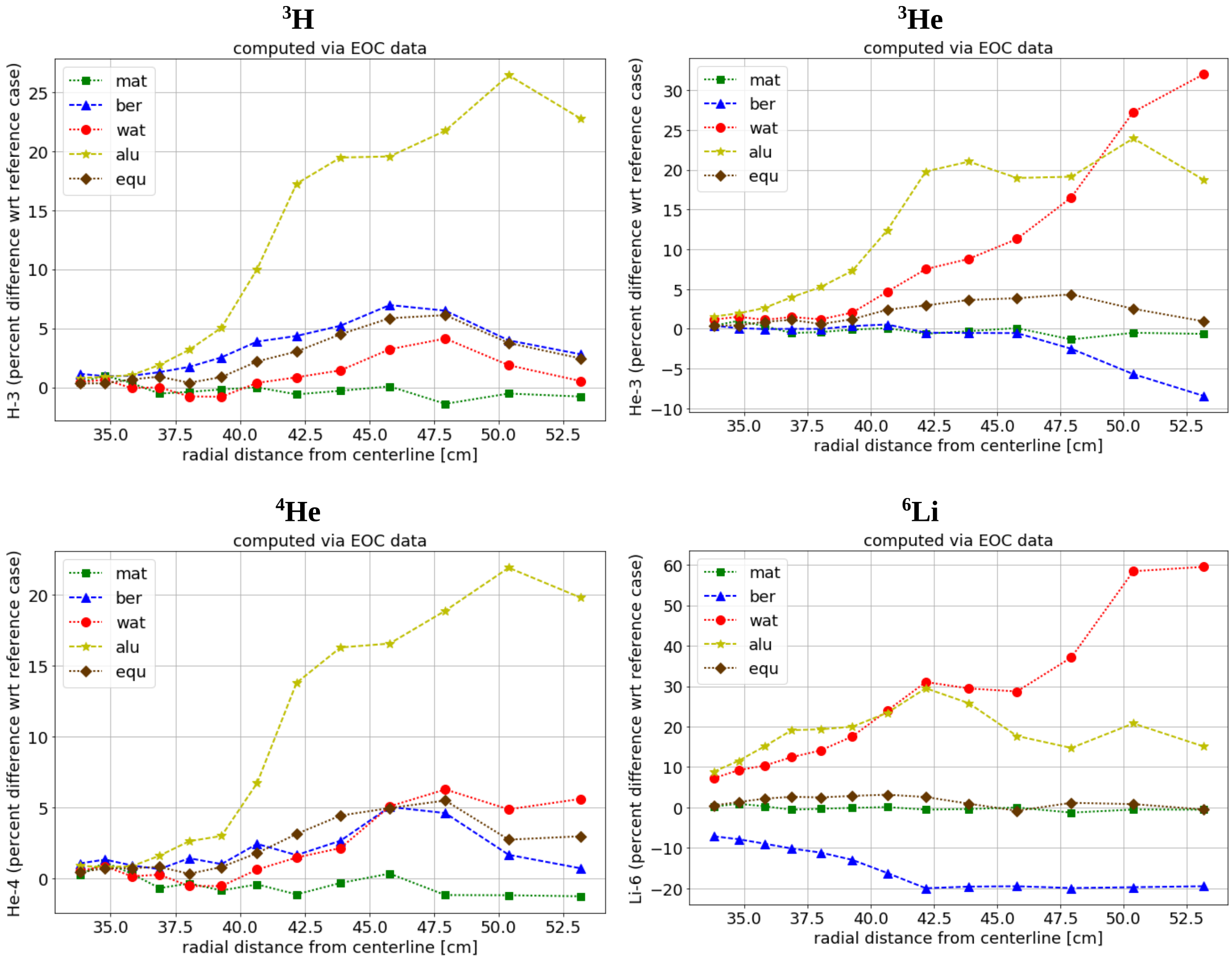
^{3}H

^{3}He

^{4}He

^{6}Li

Figure 4.19. Maximum gas and poison concentration percent differences on core midplane.

As shown in Figure 4.19, the reference case is bounded by the concept design with various loadings, and it is noted that the equivalent case again yields results similar to those of the reference case. It is important to note that the plots show percent differences associated with very small numbers, and thus the results should be interpreted accordingly. Therefore, the concept design itself has no adverse impact on gas and poison buildup in the reflector. Loading the large VXFs with Al plugs results in the greatest overall gas buildup in the reflector; however, evaluating the impact of the increased gas content (e.g., on local stresses) is outside the scope of this study.

The total and gamma-only decay heat results for each of the activation simulations were also evaluated. The total decay heat at BOC is negligible ($10^{-06} - 10^{-04}$ W/cm^3 for midplane inner radial edge mesh cell), and the total decay heat at EOC is small (~5.4×10^{-02} W/cm^3 for midplane inner radial edge mesh cell). The maximum calculated midplane total decay heat results are provided in Table 4.18 and Table 4.19, respectively, for the simulations using the BOC and EOC flux and cross section data. Figure 4.20, Figure 4.21, and Figure 4.22 illustrate the alpha+beta, gamma, and total decay heat generation rates for each of the configurations, demonstrating that beta decay is the primary decay heat constituent.

Although decay heat is considered small relative to the total heating, a 0.75% increase in the heat deposition rate results reported in Section 4.2.2 could be added to the EOC results for follow-on thermal-hydraulic-structural calculations, which would be slightly conservative. The decay heat contribution to total heating reduces across the radius of the reflector because neutrons (transmutation) attenuate more than gammas (majority of heat deposition). The decay heat contribution is ~0.75% in the innermost radial ring and ~0.20% in the outermost radial ring. The third-degree polynomial provided below could be used in the follow-on thermal calculations to determine the multiplication factors, M, to apply to the total heat deposition results reported in Section 4.2.2, as a function of radius, r (cm), relative to the core centerline.

$$M = -8.23852 \times 10^{-07} r^3 + 1.23005 \times 10^{-04} r^2 - 6.23474 \times 10^{-03} r + 1.10961\ .$$

Table 4.18. Max midplane total decay heat computed with BOC data.

r_c (cm)	total decay heat (W/cm^3)						percent difference wrt reference case				
	ref.	mat.	ber.	wat.	alu.	equ.	mat.	ber.	wat.	alu.	equ.
33.81250	5.338E-02	5.398E-02	5.439E-02	5.404E-02	5.432E-02	5.382E-02	1.12	1.89	1.24	1.76	0.82
34.78750	4.416E-02	4.472E-02	4.517E-02	4.457E-02	4.483E-02	4.447E-02	1.27	2.29	0.93	1.52	0.70
35.81250	3.605E-02	3.655E-02	3.680E-02	3.619E-02	3.666E-02	3.656E-02	1.39	2.08	0.39	1.69	1.42
36.88750	2.911E-02	2.960E-02	3.014E-02	2.936E-02	2.986E-02	2.975E-02	1.68	3.54	0.86	2.58	2.20
38.03750	2.305E-02	2.347E-02	2.403E-02	2.315E-02	2.389E-02	2.349E-02	1.82	4.25	0.43	3.64	1.91
39.28750	1.807E-02	1.838E-02	1.901E-02	1.809E-02	1.893E-02	1.848E-02	1.72	5.20	0.11	4.76	2.27
40.66250	1.389E-02	1.415E-02	1.478E-02	1.388E-02	1.514E-02	1.429E-02	1.87	6.41	−0.07	9.00	2.88
42.18750	1.078E-02	1.097E-02	1.165E-02	1.084E-02	1.238E-02	1.121E-02	1.76	8.07	0.56	14.84	3.99
43.88750	8.008E-03	8.225E-03	8.799E-03	8.187E-03	9.401E-03	8.504E-03	2.71	9.88	2.24	17.40	6.19
45.78750	5.871E-03	6.019E-03	6.700E-03	6.052E-03	7.187E-03	6.453E-03	2.52	14.12	3.08	22.42	9.91
47.93750	4.404E-03	4.538E-03	5.085E-03	4.584E-03	5.468E-03	4.866E-03	3.04	15.46	4.09	24.16	10.49
50.38750	3.263E-03	3.333E-03	3.639E-03	3.251E-03	4.120E-03	3.472E-03	2.15	11.52	−0.37	26.26	6.41
53.14875	2.245E-03	2.296E-03	2.454E-03	2.197E-03	2.759E-03	2.366E-03	2.27	9.31	−2.14	22.90	5.39

Table 4.19. Max midplane total decay heat computed with EOC data.

r_c (cm)	total decay heat (W/cm^3)						percent difference wrt reference case				
	ref.	mat.	ber.	wat.	alu.	equ.	mat.	ber.	wat.	alu.	equ.
33.81250	5.308E-02	5.380E-02	5.451E-02	5.364E-02	5.373E-02	5.380E-02	1.36	2.69	1.06	1.23	1.36
34.78750	4.408E-02	4.499E-02	4.532E-02	4.458E-02	4.460E-02	4.471E-02	2.06	2.81	1.13	1.18	1.43
35.81250	3.615E-02	3.671E-02	3.726E-02	3.632E-02	3.658E-02	3.679E-02	1.55	3.07	0.47	1.19	1.77
36.88750	2.936E-02	2.960E-02	3.045E-02	2.948E-02	2.988E-02	2.995E-02	0.82	3.71	0.41	1.77	2.01
38.03750	2.333E-02	2.358E-02	2.437E-02	2.323E-02	2.403E-02	2.370E-02	1.07	4.46	−0.43	3.00	1.59
39.28750	1.824E-02	1.851E-02	1.930E-02	1.813E-02	1.910E-02	1.866E-02	1.48	5.81	−0.60	4.72	2.30
40.66250	1.405E-02	1.432E-02	1.521E-02	1.408E-02	1.535E-02	1.460E-02	1.92	8.26	0.21	9.25	3.92
42.18750	1.096E-02	1.111E-02	1.201E-02	1.098E-02	1.270E-02	1.150E-02	1.37	9.58	0.18	15.88	4.93
43.88750	8.216E-03	8.395E-03	9.133E-03	8.285E-03	9.735E-03	8.783E-03	2.18	11.16	0.84	18.49	6.90
45.78750	6.058E-03	6.230E-03	6.909E-03	6.228E-03	7.251E-03	6.582E-03	2.84	14.05	2.81	19.69	8.65
47.93750	4.582E-03	4.668E-03	5.235E-03	4.713E-03	5.607E-03	4.995E-03	1.88	14.25	2.86	22.37	9.01
50.38750	3.358E-03	3.455E-03	3.771E-03	3.330E-03	4.233E-03	3.594E-03	2.89	12.30	−0.83	26.06	7.03
53.14875	2.294E-03	2.365E-03	2.564E-03	2.256E-03	2.839E-03	2.449E-03	3.10	11.77	−1.66	23.76	6.76

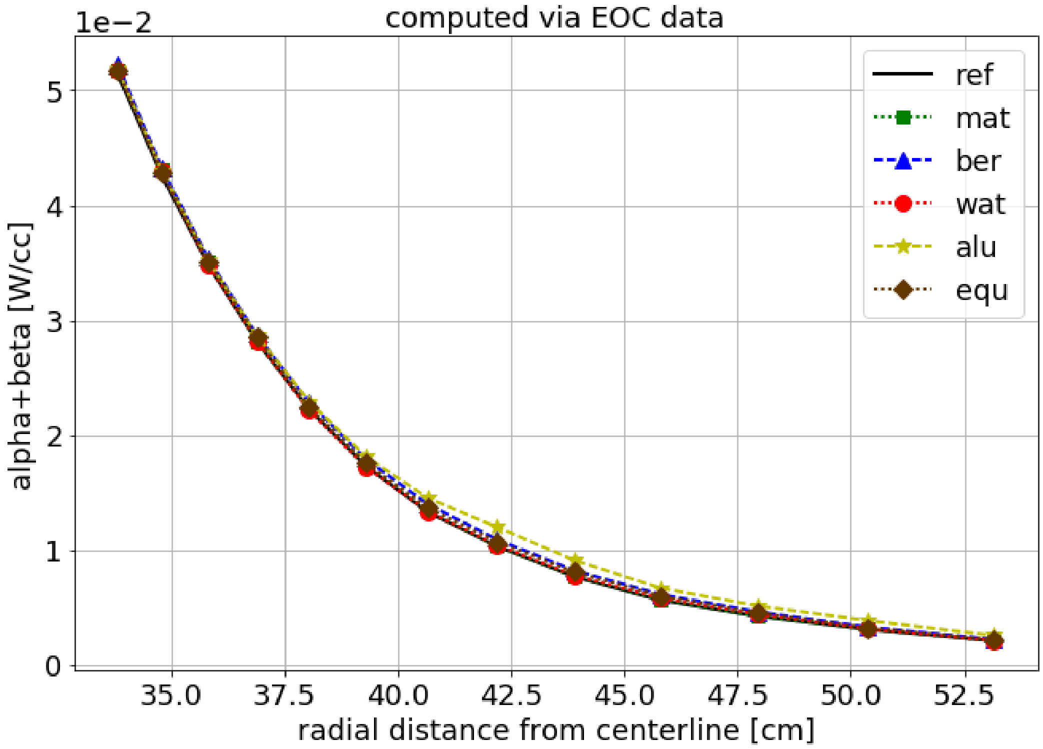

Figure 4.20. Maximum calculated EOC alpha+beta decay heat results on core midplane.

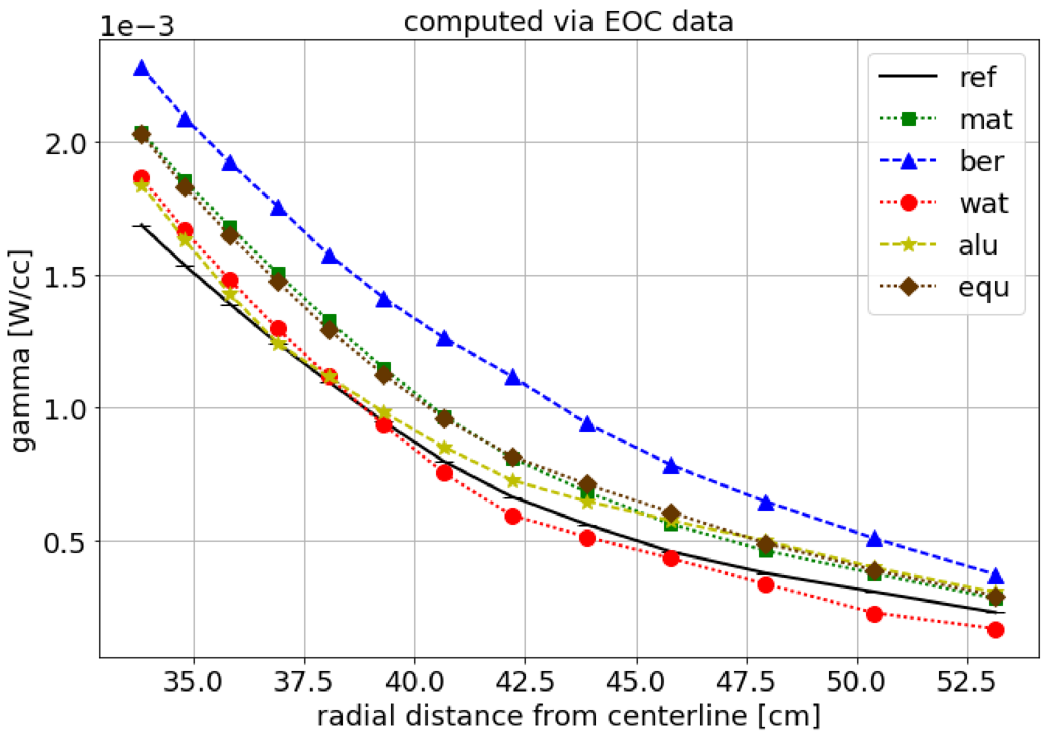

Figure 4.21. Maximum calculated EOC gamma decay heat results on core midplane.

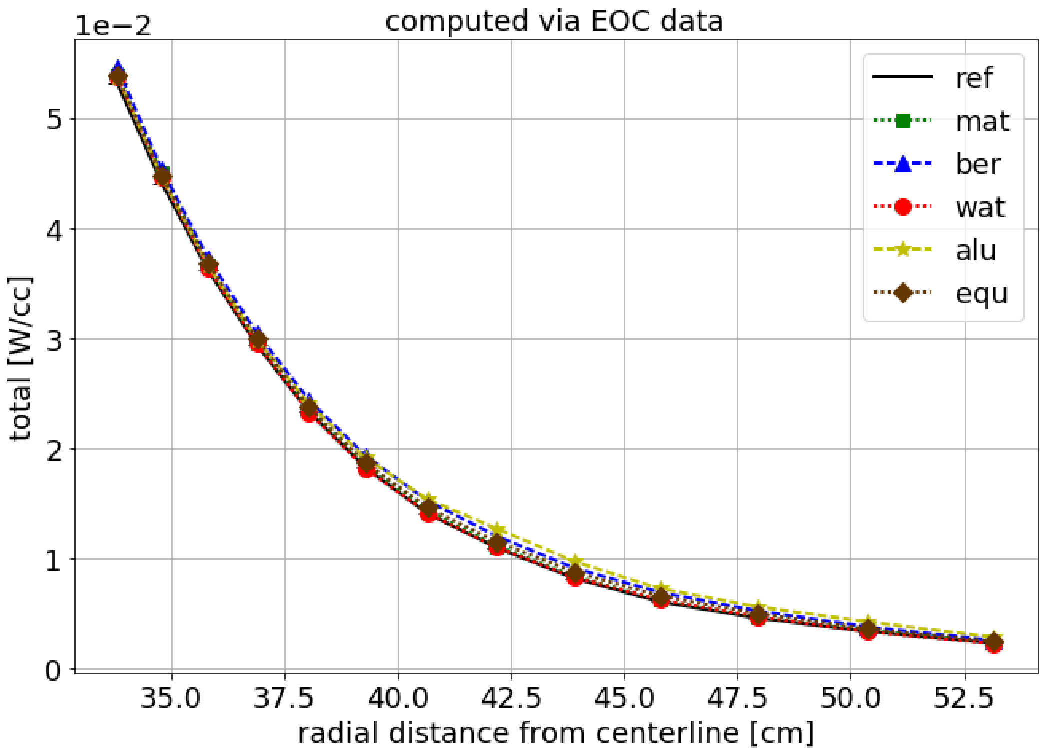

Figure 4.22. Maximum calculated EOC total decay heat results on core midplane.

4.3 PERFORMANCE ASSESSMENT

This section documents the computations and analyses performed to assess the impact of the various configurations on the performance of HFIR. The evaluations and results documented in this section are not necessarily safety related; rather, they are programmatic evaluations and include descriptions of impacts on experiments, neutron flux distributions, and dose rate distributions.

4.3.1 Qualitative Description of Impacts to Experiments

High-level summaries regarding the impacts of the concept reflector design on HFIR primary missions are discussed in this section. Missions including neutron scattering, isotope production, materials irradiation, and neutron activation analysis are briefly discussed.

4.3.1.1 Beamline fluxes for neutron scattering

The beamline fluxes with the concept reflector design will be equivalent to or better than those with the existing reflector design. Experiments (e.g., ^{238}Pu production targets) adjacent to HB-2 and HB-3 may have small-to-negligible impacts on their beamline fluxes, but the VXF layout of the concept reflector was designed to minimize the impact on beam tube fluxes even if filled with strongly absorbing targets. The VXF layout of the concept design is more optimized than the existing design when considering an experimentless reflector or one loaded with irradiation experiment targets. Potential impacts of experiments in the Be reflector on beam tube fluxes are addressed through experiment review and approval processes. RRD recently set a programmatic requirement (not safety related) to limit beam tube flux perturbations caused by experiments loaded in the Be reflector to 5% or less.

The VXFs adjacent to HB-1 were moved slightly closer to the beam tube relative to those of the existing design, but these VXFs have negligible impacts on the beamline fluxes because their locations are relatively far from the beam tube hemispherical region, where neutrons enter before traveling down the beam tube. Therefore, the HB-1 beamline fluxes will be maintained with the concept reflector design.

Relative to the existing design, the concept design provides more Be material immediately surrounding the HB-2 hemispherical region by (1) rotating the inner small VXF adjacent to HB-2, located between HB-1 and HB-2, away from HB-2 and (2) removing the outer small VXF adjacent to HB-2 that is located between HB-2 and HB-3. Thus, the HB-2 beamline fluxes will be maintained or enhanced with the concept design reflector.

The HB-3 beamline fluxes will be slightly enhanced with the concept design because of the additional Be material immediately surrounding the HB-3 hemispherical region as a result of rotating the adjacent VXFs away from the beam tube hemisphere.

The two VXFs adjacent to HB-4 in the concept design are rotated away from the beam tube relative to the existing design to increase the Be thickness between the VXFs and the beam tube. Because these VXFs are relatively far from the HB-4 hemispherical region and moderator vessel, they will have negligible impacts on the HB-4 beamline fluxes. Thus, the HB-4 beamline fluxes will be maintained with the concept reflector design.

4.3.1.2 Isotope production and materials irradiation

The concept reflector design will not impact the neutron fluxes (spectrum or magnitude) in the flux trap target region, where the majority of HFIR isotope production, less ^{238}Pu production, and materials irradiation experiments take place. Similarly, the concept design will have no impact on the neutron fluxes to the experiment facilities located within the removable beryllium reflector or the semi-PB reflector. Thus, the performance of the reactor, in terms of experiment irradiations inboard of the PB reflector, is maintained with the concept reflector design.

The increased number of VXFs in the concept design enhances the flexibility of the permanent reflector for isotope production and materials irradiation. Existing holder and target designs for experiment irradiations previously qualified for use in VXF positions (e.g., ^{238}Pu production targets/holders, ^{252}Cf production targets/holders, EPRI targets/holders) will not require requalification or redesign because they will fit into the concept design VXFs, and the bounding irradiation conditions analyzed will be maintained.

The inner small VXF bolt circle diameter is maintained from the existing design; thus, the neutron fluxes in these facilities are also maintained. The outer small and large VXF bolt circle radii are slightly increased to enhance the thermal-structural-hydraulic performance, which consequently slightly reduces the neutron flux magnitude and softens the spectrum to these facilities. However, the impacts of these changes will be trivial and will have no adverse impacts to typical experiment irradiations in these facilities. The additional large VXFs increase the versatility of the reactor by providing more irradiation volume and enabling a greater number of experiments that require large VXFs to be performed simultaneously.

Plutonium-238 production

Aluminum cladded targets containing ^{237}Np are irradiated in the permanent reflector VXFs for the purpose of producing ^{238}Pu, which is used as the power source in radioisotope thermoelectric generators critical to NASA deep-space and planetary missions. The existing reflector houses 22 VXFs; however, one inner small VXF contains PT-1 and one large VXF is inaccessible. Furthermore, depending on the ^{238}Pu production target type, three to five of the VXFs would likely not be permitted to be loaded with targets due to their proximity to the hemispherical regions of the beam tubes. Therefore, a maximum of ~15–17 VXFs are available for ^{238}Pu target irradiations with the existing reflector number 4.

Not only does the concept reflector number 5 design have six more VXFs (28 total) than the existing design, but the layout of the VXFs in the concept reflector was designed to have minimal impact on the fluxes down the beam tubes, even if filled with ^{238}Pu production targets. Thus, fewer VXFs are unavailable (~0–3 depending on the ^{238}Pu production target type) for target irradiations in the concept design than in the existing design. More irradiation volume and flexibility will be available with the concept reflector; therefore, the concept design will be beneficial for the ^{238}Pu production program, as demonstrated in the study by Chandler et al. (2019).

4.3.1.3 Neutron activation analysis

Pneumatic tubes located in inner small VXF-7 (PT-1) and EF-2 (PT-2) of the existing reflector design are used for neutron activation analysis. No changes from the existing reflector to the concept reflector impact the design of PT-2; however, PT-1 will be moved to a different azimuthal location within an inner small VXF, but the bolt circle diameter on which the inner small VXFs reside remains unchanged. The distance from the core centerline to the centerline of the pneumatic tubes is thus unchanged. Therefore, the neutron flux magnitude and spectrum in the pneumatic tubes will be maintained in the concept reflector design.

PT-1 is currently foreseen to be loaded into either VXF-9 or VXF-13 of the concept reflector. Placement of PT-1 in VXF-9 of the concept reflector provides a location close to that of VXF-7 of the existing reflector design, thus requiring only small changes to the piping system extending above the reflector. This location would likely render outer large VXF-8 unusable due to the route required for the piping between the pressure vessel head and the experiment facility. Placement of PT-1 in VXF-13 of the concept reflector would require a little more effort due to plumbing changes. However, relocating PT-1 to VXF-13 is advantageous because neutron-absorbing experiments could be potentially loaded in VXFs only on one side (compared to three if loaded in VXF-9), and the plumbing system could be routed above the reflector so as not to interfere with any other VXF.

Experiments (e.g., ^{238}Pu targets, ^{252}Cf targets) and experiment facilities (e.g., beam tubes, control rod access plugs) nearby the PT facilities could impact the PT fluxes, but this is the case for both the current and the concept reflector designs. As is the case with the current reflector, it will be up to the experiment coordination team to determine the placement of experiments in the concept reflector so as not to unnecessarily interfere with the fluxes to the PT facilities.

4.3.2 Neutron Flux Distributions

Three-energy group neutron flux distributions, including the azimuthally averaged flux on the core horizontal midplane, r-z azimuthally averaged flux, and x-y flux on the core horizontal midplane were calculated. Select results are provided in this section to demonstrate how the various VXF loadings can impact the core neutron flux distribution.

The perturbed-to-reference azimuthally averaged neutron flux ratios are provided in Figure 4.23. The plots illustrate the differences between the perturbed and reference cases and show how the azimuthally averaged material composition impacts the flux distribution along the radius of the reactor on the core horizontal midplane. Perturbed-to-reference thermal and fast neutron flux ratios on the x-y core horizontal midplane are provided in Figure 4.24 and Figure 4.25, respectively. The thermal and fast neutron fluxes are provided because they are respectively used as metrics for isotope production and materials irradiation capabilities.

When interpreting these results, it is important to understand the layout of the VXFs in both the current and concept designs. It is also important to consider the location of the PT-1 facility because it consists of several SST pipes. For all perturbed cases, there are trivial or no differences inboard of the Be reflector. It is again observed that the increased absorption in the water/SST liner case and the increased scattering in the Be plug case result in reduced and increased neutron fluxes, respectively, in the permanent reflector. Thus, the selection of the VXF loadings is important to local PB reflector fluxes, but the concept reflector design itself does not result in degraded reactor performance.

mat-to-ref flux ratios

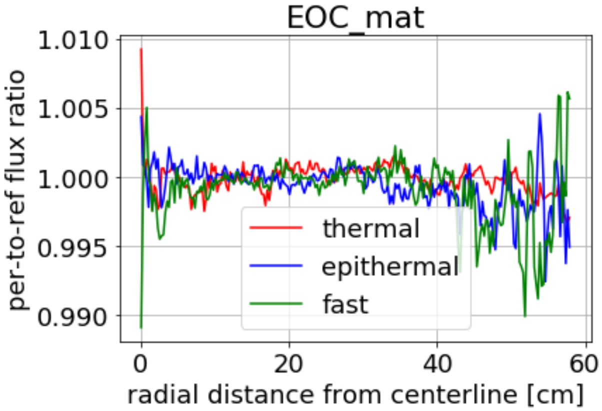

ber-to-ref flux ratios

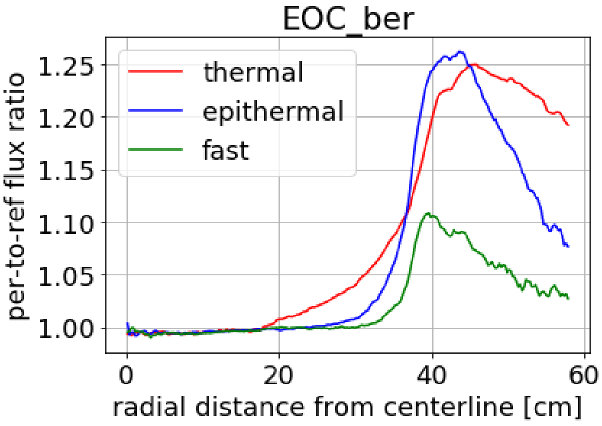

wat-to-ref flux ratios

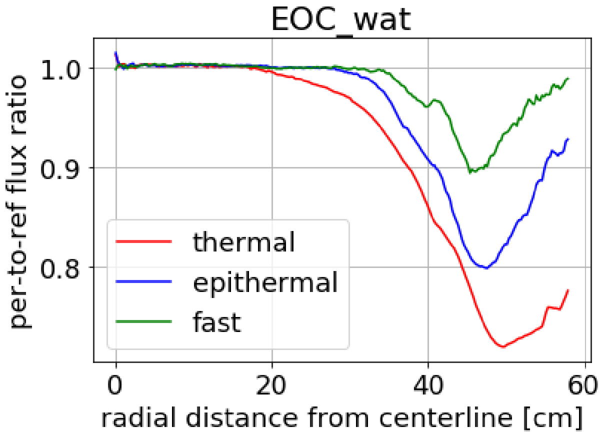

alu-to-ref flux ratios

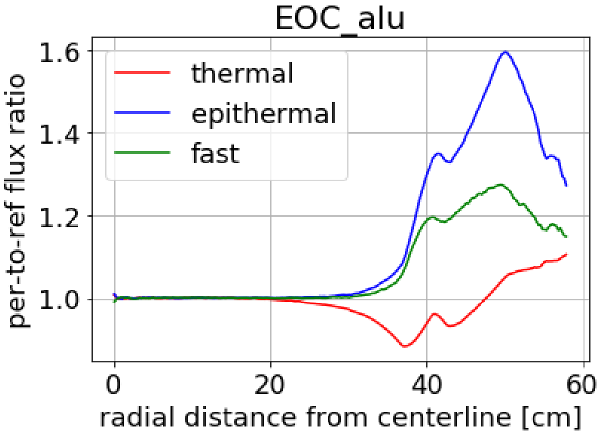

equ-to-ref flux ratios

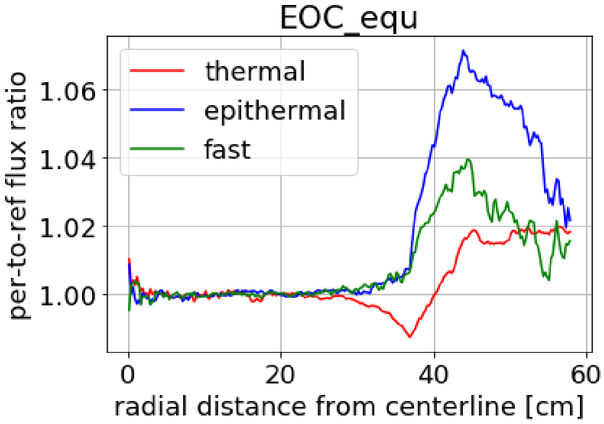

Figure 4.23. Three-energy group azimuthally averaged neutron flux ratios on core horizontal midplane.

ber-to-ref flux ratios **wat-to-ref flux ratios**

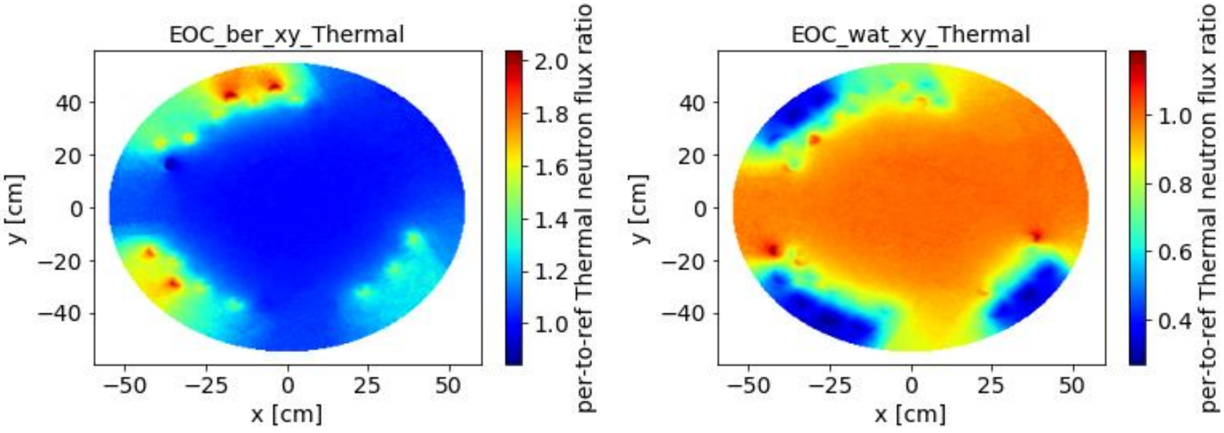

alu-to-ref flux ratios **equ-to-ref flux ratios**

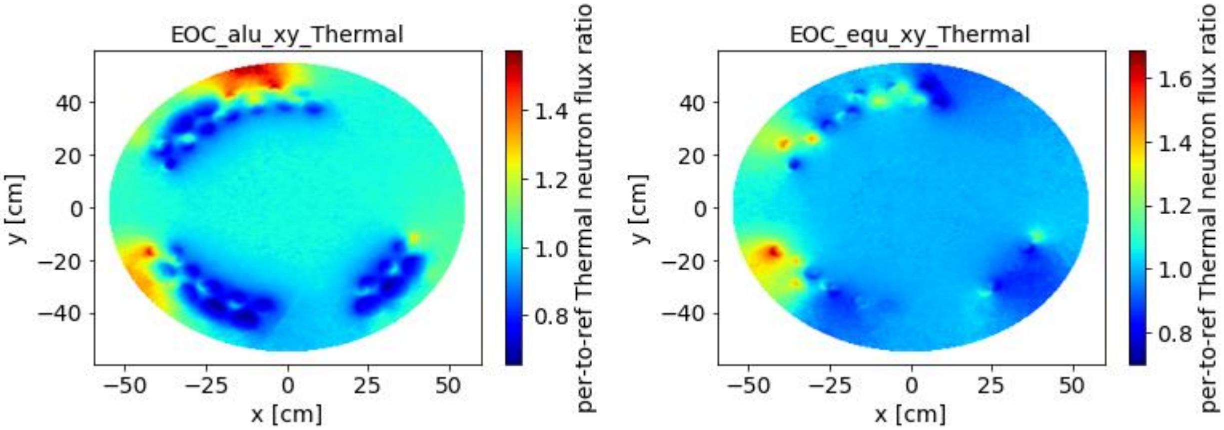

Figure 4.24. Thermal neutron flux ratios on x-y core horizontal midplane.

ber-to-ref flux ratios **wat-to-ref flux ratios**

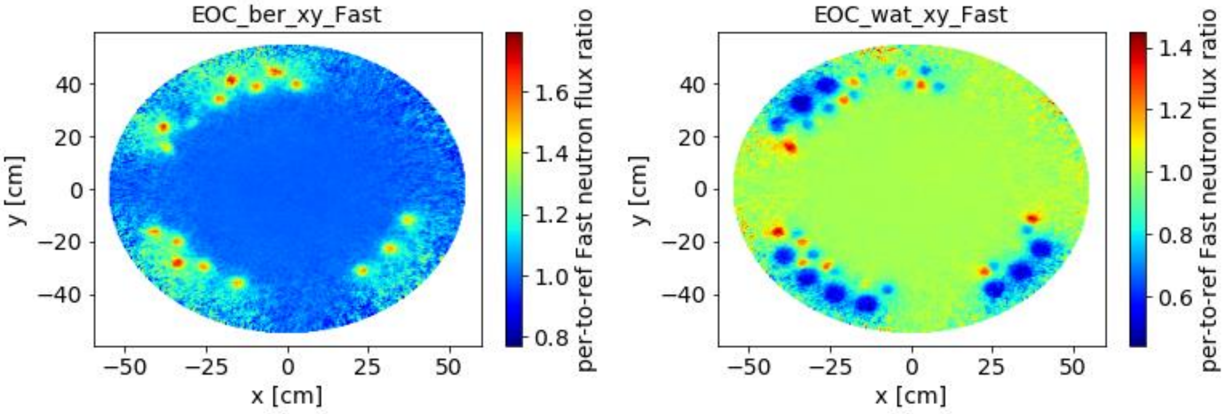

alu-to-ref flux ratios **equ-to-ref flux ratios**

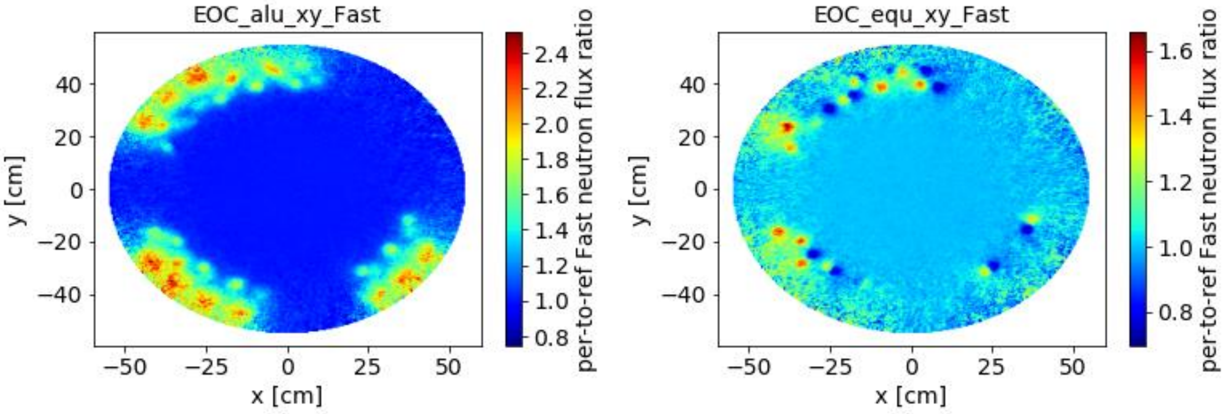

Figure 4.25. Fast neutron flux ratios on x-y core horizontal midplane.

4.3.3 Impact to Radiation Beyond Beryllium

The impacts of the various configurations on radiation source terms radially outward of the Be reflector are evaluated in this section. The purpose of these evaluations is to assess, with a first-order approach, how changes to the VXF layout and loadings can impact the radiation sources to the ionization chambers and the pressure vessel.

4.3.3.1 Ion chamber description

The reactor safety and servo control systems make use of three channels, with final control and protective actions on a two-out-of-three logical basis. Each of the three safety system channels measures and analyzes various plant parameters to determine the existence of potentially unsafe conditions. The safety and servo control systems are independent of each other, and the purpose of the safety system is to override the control system and ensure rapid shutdown if any safety parameters exceed their preset values. The three servo channels provide the primary automatic control of reactor power at levels above N_L (10% power).

The safety and servo systems utilize uncompensated ion chambers located inside thimbles that penetrate the reactor vessel at azimuthal angles of 120°, 220°, and 300°, respectively, when defining North as 90° and the HB-2 centerline as 180°. The thimbles enter the vessel above the core horizontal midplane and are directed downward at an angle of 30° relative to the horizontal plane.

The reactor power signal to each servo channel originates as current in an ionization chamber, which is proportional to the thermal neutron flux. The flux signal is then modified via calibration against the reactor heat power measurement, thus offsetting variations between measured flux and reactor power. The drive mechanism positions the ionization chambers as required over a range of 12 in. to compensate for flux changes during the cycle, which are primarily due to control element withdrawal during the cycle to compensate for reactivity loss caused by fuel depletion and fission product generation.

4.3.3.2 Pressure vessel embrittlement description

The beam tubes are responsible for significant radiation damage to the reactor vessel because they displace Be and water, which would act as radiation shields to reduce the neutron and gamma fluxes to the vessel. Subsequently, the most severe radiation-induced embrittled portion of the vessel is restricted to small areas around the beam tubes (i.e., vessel nozzles and closely surrounding materials) at the beltline region because radiation streams down the beam tubes toward the vessel. Specifically, the region incurring the most significant radiation damage is the HB-2 nozzle because HB-2 is the largest beam tube and it enters the reflector straight on, unlike HB-1, -3, and -4, which enter the reflector tangentially.

As described in the SAR document (2021) Section 5.3.3.3.1, "Vessel embrittlement (fracture toughness)," the embrittlement of vessel materials is determined by measuring the nil-ductility transition temperature of Charpy V notch specimens of vessel materials that are removed per the vessel surveillance program. Fracture mechanics is used for vessel integrity evaluations. Section 5.3.3.4, "Surveillance program," of the same document (SAR 2021) describes, in detail, the surveillance program and the methods used to monitor and evaluate vessel radiation embrittlement and integrity.

4.3.3.3 Neutron flux and gamma dose rate assessments

Radiation sources were characterized via three-energy group neutron flux and gamma dose rate 2D z-θ mesh tallies in the annulus between the PB reflector and the aluminum cage. A 24 azimuthal (15° segments) by 11 axial (~5.5 cm axial zones) mesh was employed. ICRP 51 fluence to air dose conversion coefficients (ICRP 1987) and the MCNP DE/DF cards were employed to fold in the appropriate conversion function to calculate the gamma dose rates in R/hr. The prompt plus capture gamma dose rate was calculated in a KCODE, simulation and the delayed gamma dose rate was calculated in a fixed-source decay gamma simulation. The total gamma dose rates are computed as the sum of the two.

The reference-to-perturbed flux and gamma dose rate ratios are provided in Figure 4.26–Figure 4.29 for the Be plug, water/SST liner, Al plug, and equivalent loading cases. The ion chambers enter the pressure vessel at azimuthal angles of 120°, 220°, and 300°, respectively, as illustrated in these figures, and the HB-2 centerline is defined as 180°. The gamma dose rates for all perturbed cases, in all mesh cells, are within ±8% of the reference case. As shown in the previous sections, large local neutron flux changes can occur because of the VXF loadings, and the reference case is again bounded by the various perturbations. The Be and Al plug cases yield greater neutron fluxes in the vicinity of the ion chambers relative to the reference case and the water/SST liner case results in reduced fluxes.

Based on historical operations with various experiments (e.g., ^{238}Pu targets in Al holders, ^{252}Cf targets in Al holders, EPRI targets, LEU fuel in Hf shields, Be plugs) and the rapid attenuation of radiation in the pool water, it is expected that there is more than enough range in the drives to accommodate the configurations modeled. Also, the sources calculated in the vicinity of HB-2, where the most significant radiation damage occurs, are not significantly affected because of the orientation of HB-2.

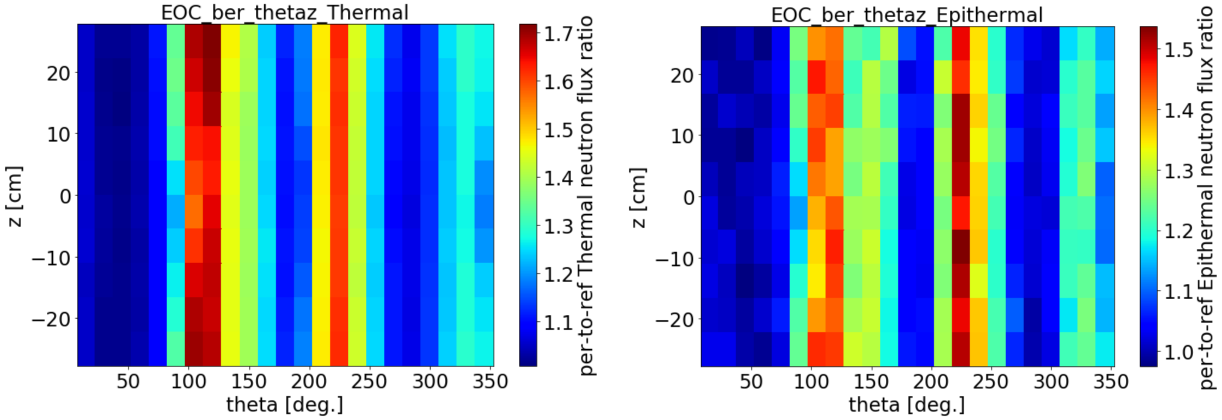

ber-to-ref thermal flux ratio

ber-to-ref epithermal flux ratio

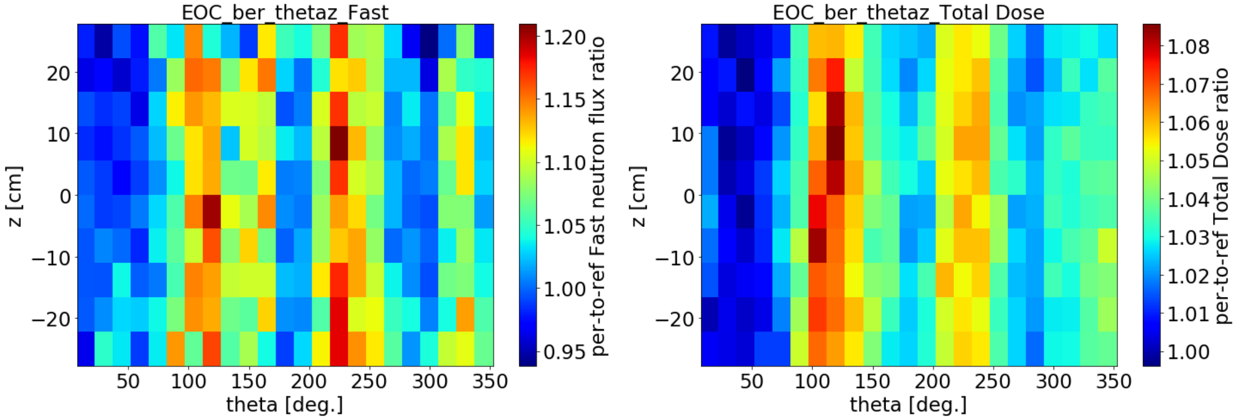

ber-to-ref fast flux ratio

ber-to-ref total gamma dose rate ratio

Figure 4.26. Beryllium plug case beyond reflector flux and gamma dose rate ratios.

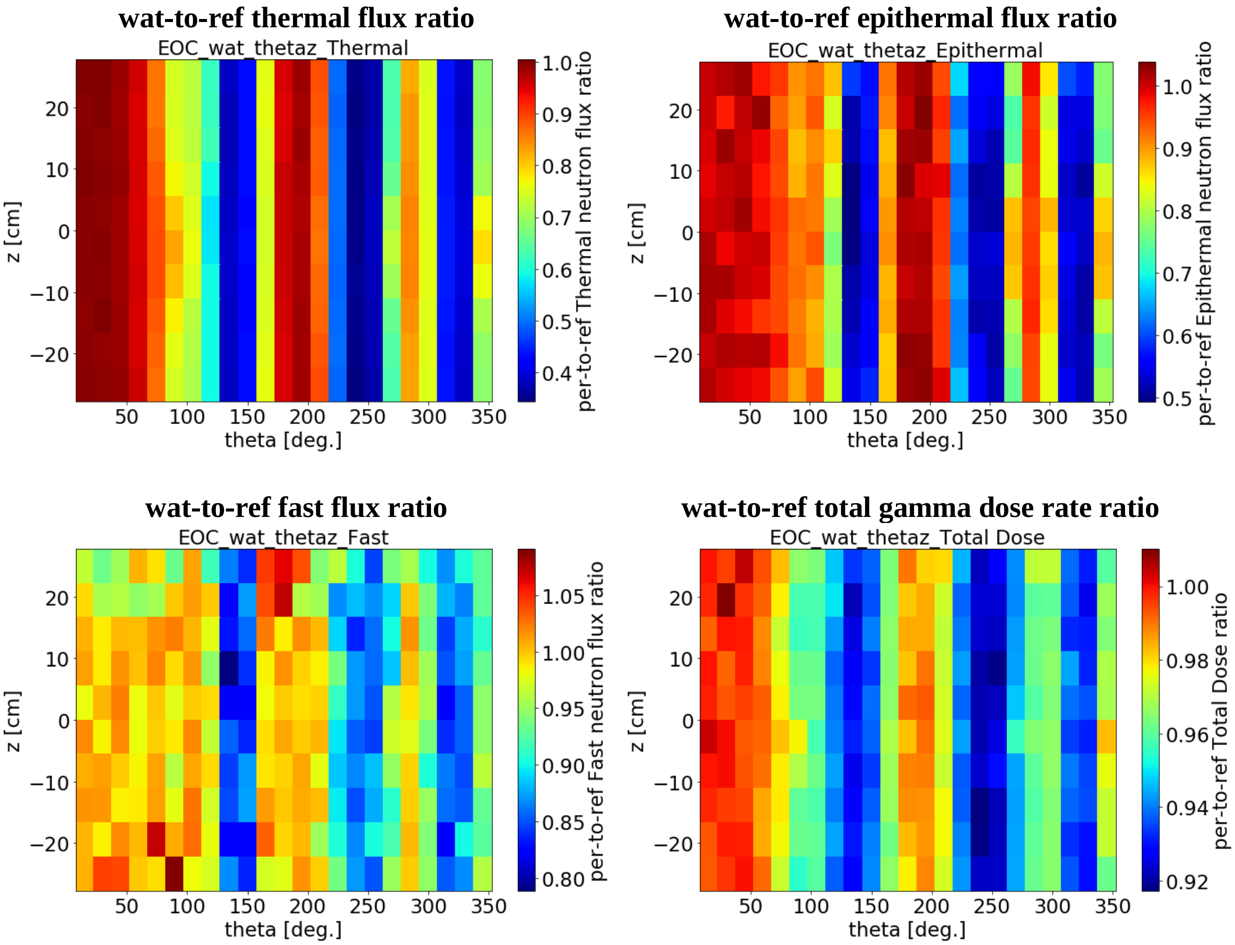

wat-to-ref thermal flux ratio

wat-to-ref epithermal flux ratio

wat-to-ref fast flux ratio

wat-to-ref total gamma dose rate ratio

Figure 4.27. Water/SST liner case beyond reflector flux and gamma dose rate ratios.

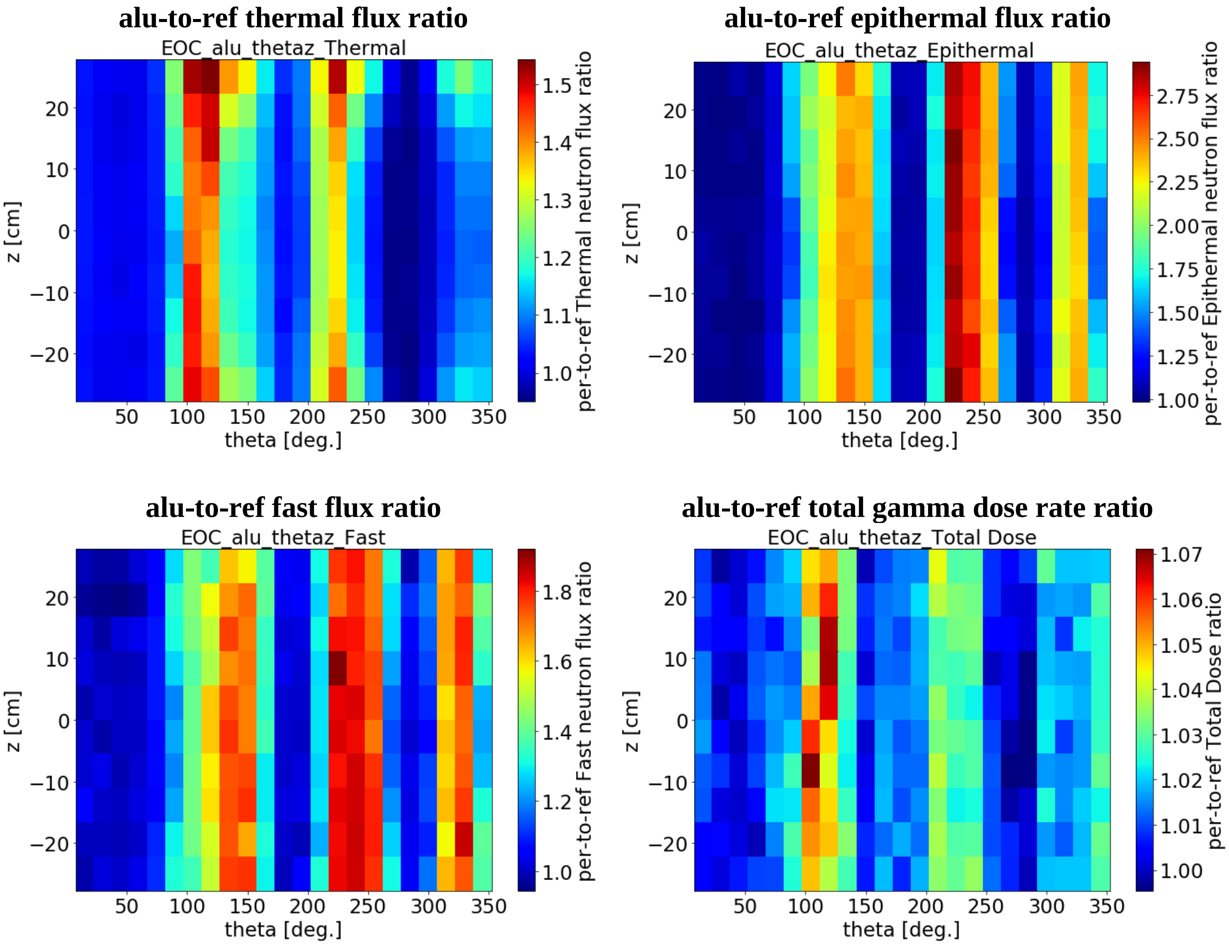

alu-to-ref thermal flux ratio

alu-to-ref epithermal flux ratio

alu-to-ref fast flux ratio

alu-to-ref total gamma dose rate ratio

Figure 4.28. Aluminum plug beyond reflector flux and gamma dose rate ratios.

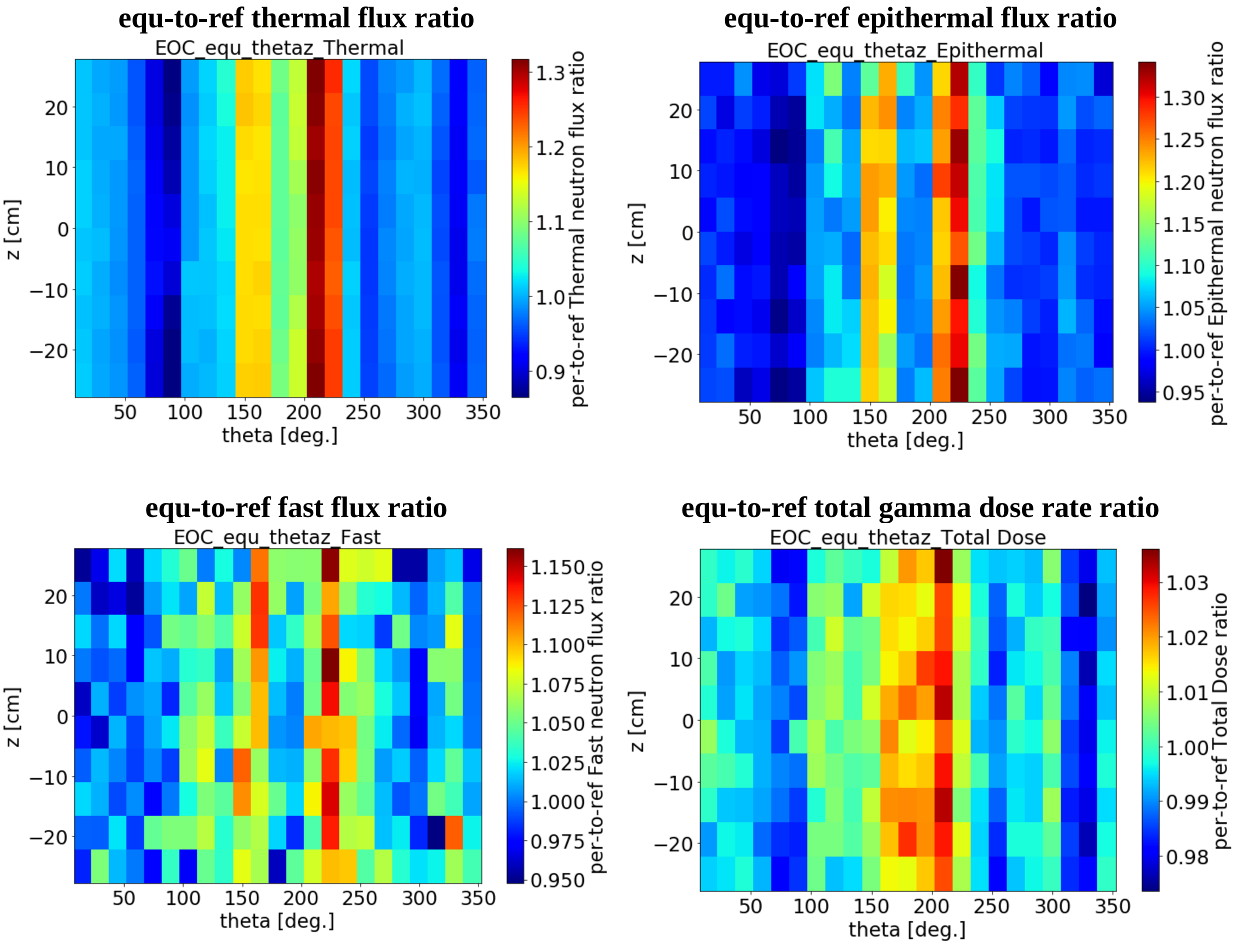

equ-to-ref thermal flux ratio

equ-to-ref epithermal flux ratio

equ-to-ref fast flux ratio

equ-to-ref total gamma dose rate ratio

Figure 4.29. Equivalent beyond reflector flux and gamma dose rate ratios.

5. SUMMARY OF RESULTS AND CONCLUSIONS

A new PB reflector (number 5) has been designed and is referred to as the concept reflector/design throughout this report. The concept design includes 28 VXFs, which is six greater than the current reflector (number 4). This new design is highly desired for several reasons: to increase its versatility for irradiation experiments, to arrange the VXFs in a layout that minimizes their impact on neutron scattering if loaded with neutron absorbing experiments, to enhance its thermal-structural-hydraulic performance, and to simplify the fabrication process. The analyses documented in this report evaluate reactor physics aspects of the concept PB reflector number 5 design.

The MCNP5 v1.51 and SCALE 6.1.3 computer codes were employed to model and simulate HFIR with the current and concept reflectors. The approach taken included developing a high-fidelity model of the current reflector design with a typical "experimentless" loading (water/SST liners in small VXFs and Be plugs in large VXFs) and comparing its results to those of the concept design with bounding experimentless VXF loadings. Perturbation studies were performed, and the current Be reflector model served as the reference case. Five perturbed models were developed to evaluate the impact of the subject perturbations on various reactor physics metrics:

1. Material change case, "mat," current no. 4 reflector design with the no. 5 Be composition
2. Be plug case, "ber," concept reflector design with Be plugs in all VXFs
3. Water/SST liner case, "wat," concept reflector design with water/SST liners in all VXFs
4. Al plug case, "alu," concept reflector design with Al plugs in all VXFs
5. Equivalent loading, "equ," concept reflector design with Be plugs in five inner small and all large VXFs, with the remaining VXFs loaded with water/SST liners

Core reactor physics were assessed for all six models under BOC and EOC conditions. The reactivity worth of the mat case relative to the reference case was small and positive (<1¢), proving that the material composition of the no. 5 Be has trivial reactor physics impacts. The EOC "ber" and "wat" reactivity worths with respect to the reference case were respectively calculated as +34 and −24 cents, thus bounding the reference case. The "equ" case, with a mixture of Be plugs and water/SST liners, was developed to yield a reactivity equivalent to the reference case. The reactivity differences between the concept and current reflector models were demonstrated to be small relative to some other typical cycle-to-cycle reactivity variations. The reactivity differences are attributed to the VXF loadings and not the reflector design itself. Thus, it is concluded that the concept reflector design will have no significant impact on cycle length, safety margin, core reactivity coefficients, or differential/integral rod worths.

No significant impacts on core fission rate distributions, or "flux tilts," were observed for any of the perturbed cases. The "ber" case results in a slight increase (~1%) in the r-z azimuthally integrated fission rate density on the outer edge of the outer fuel element, with a maximum local r-z-θ increase of ~2.5%. Negligible fission rate density changes were detected for the other perturbed cases.

PB reflector heat deposition, peak fast flux/fluence, gas and neutron poison generation, and decay heat metrics were also evaluated. The peak volumetric heat deposition is essentially unaffected by all perturbations and was calculated to be ~7.4 W/cm^3. Maximum differences up to ±5%, which is considered small, were calculated in the outer radial half of the reflector due to the various VXF loadings. Decay heat, for all cases, was determined to contribute less than 1% to the total heat deposition and can therefore be considered negligible.

The peak fast ($E_n > 1$ MeV) flux and fluence in the permanent reflector were not influenced significantly by the perturbations studied. For the various configurations analyzed, a peak fast fluence of 1.22×10^{22} n/cm^2 was predicted assuming a 279,000 MWd end of life.

Beryllium reflector 44-energy group fluxes and effective one-group group ^{9}Be(n,α), ^{9}Be(n,2n), ^{6}Li(n,t), and ^{3}He(n,p) cross sections were tallied and used for input to activation calculations that assumed 132 consecutive reactor cycles consisting of 25 d irradiation periods and 25 d decay periods (280,500 MWd). Maximum ^{3}H, ^{3}He, ^{4}He, and ^{6}Li concentrations of 0.25 mg/cm^3, 1.11 µg/cm^3, 2.40 mg/cm^3 (0.29 at. %), and 3.03 µg/cm^3 were respectively estimated. The peak values varied little among the cases analyzed; however, larger (<35%) but not concerning differences are observed in the outer radial half of the reflector due to flux (magnitude and spectrum) differences induced by the VXF loading choices. The gas and neutron poison buildup calculated for the perturbed cases bound those calculated for the reference case and therefore again prove that the concept design itself has no adverse physics impacts.

With respect to reactor performance, discussions were provided regarding the impact of the new reflector on HFIR's primary missions. Three-energy group neutron flux and gamma dose rate distributions were also tabulated to assess differences caused by the subject perturbations. The concept reflector will maintain or slightly enhance the neutron sources delivered to the neutron scattering instruments and will have no impact on the flux magnitude or distribution within the flux trap target region. The more optimal VXF layout and additional six VXFs will make the permanent reflector more versatile for irradiation experiments to be performed in the VXFs.

The neutron flux radially outward of the Be reflector varies among the cases analyzed. However, the flux in the vicinity of HB-2 varied little, which suggests radiation damage induced by neutron bombardment in the most concerning region of the pressure vessel (i.e., the HB-2 nozzle region) would not be affected for any of the cases modeled. Larger flux differences were observed in areas near the three ionization chambers, but there should be enough range in the drives to accommodate the changes based on historical operations and experiment loadings. However, it is important to reiterate that the differences are introduced solely from the contents of the VXFs, and thus the concept reflector design has no adverse impacts: VXF contents are evaluated on a case-by-case basis by RRD personnel. The gamma dose rates radially outward of the permanent reflector varied little among the cases modeled and therefore should not impact the gamma radiation to the ionization chambers or the pressure vessel.

In conclusion, the concept Be reflector itself has no adverse impacts on reactor physics safety (e.g., core fission rate distribution, shutdown margin) or performance (e.g., cycle length, local fluxes in reflector); however, the choice of the VXF contents can have positive or adverse impacts on performance. The concept design with Be plugs in five inner small and all large VXFs, with the remainder of the VXFs containing water/SST liners, yields physics results equivalent to the current reflector reference case.

6. REFERENCES

J. Bucholz. 1997. "HFIR Upgrade Reflector Impact on Core Nuclear Performance," C-HFIR-1997-025. Internal archived document that may be made available upon request to the RRD Division Director.

M. B. Chadwick et. al. 2006. "ENDF/B-VII.0: Next Generation Evaluated Nuclear Data Library for Nuclear Science and Technology," Nuclear Data Sheets, **107**, pp. 2931–3060.

D. Chandler, B. R. Betzler, E. E. Davidson, and G. Ilas. 2020. "Modeling and Simulation of a High Flux Isotope Reactor Representative Core Model for Updated Performance and Safety Basis Assessments," *Nuclear Engineering and Design*, **366**, 110752. doi: doi.org/10.1016/j.nucengdes.2020.110752

D. Chandler, M. W. Crowell, and K. E. Royston. 2019. "Increased Plutonium-238 Production via High Flux Isotope Reactor Permanent Beryllium Reflector Redesign," Nuclear and Emerging Technologies for Space (NETS) 2019, Richland, WA.

D. Chandler. 2012. "Nuclear Heating and Radionuclide Inventory Calculations to Support NpO2 Single Pellet Irradiations in HFIR," C-HFIR-2012-006, Rev. 0. Internal archived document that may be made available upon request to the RRD Division Director.

COMSOL Multiphysics® v5.3. 2017. www.comsol.com, COMSOL AB, Stockholm, Sweden.

C. Daily. 2016. "Heat Generation Rates in Gadolinium-Shielded Experiment RB19J in Position RB-5B of the HFIR Beryllium Reflector," C-HFIR-2016-010 Rev. 1. Internal archived document that may be made available upon request to the RRD Division Director.

E. E. Davidson (née Sunny), B. R. Betzler, D. Chandler, and G. Ilas. 2017. "Heat Deposition Analysis for the High Flux Isotope Reactor's HEU and LEU Core Models," *Nuclear Engineering and Design*, Vol. **322**, pp. 563–576. doi: doi.org/10.1016/j.nucengdes.2017.06.040

Design Change Memo (DCM). 2002. "Permanent & Semi-Permanent Reflector Upgrade," DCM HFIR-197M-1.

Review and Approval Process for HFIR In-Vessel and Gamma Irradiation Experiments. 2013. EG-1, Rev. 10.

Configuration-Control Requirements for High Flux Isotope Reactor (HFIR) Experiments, Experiment Facilities, and Beam Tube Facilities. 2007. EG-2, Rev. 4.

International Commission on Radiological Protection (ICRP). 1987. *Annals of the ICRP*, "Data for Use in Protection Against External Radiation," **17**, No. 2/3.

G. Ilas, D. Chandler, B. Ade, E. Sunny, and B. Betzler. 2015. "Modeling and Simulations for the High Flux Isotope Reactor Cycle 400," ORNL/TM-2015-36, Oak Ridge National Laboratory.

X-5 Monte Carlo Team. 2003. “MCNP—A General Monte Carlo N-Particle Transport Code, Version 5,” LA-CP-03-0245, Los Alamos National Laboratory.

S. W. Mosher, S. R. Johnson, A. M. Bevill, et al. 2015. “ADVANTG – An Automated Variance Reduction Parameter Generator,” ORNL/TM-2013/416, Rev. 1, Oak Ridge National Laboratory.

National Institute of Standards and Technology (NIST). 2018. Atomic Weights and Isotopic Compositions with Relative Atomic Masses, https://www.nist.gov/pml/atomic-weights-and-isotopic-compositions-relative-atomic-masses

National Nuclear Data Center. 2018. *Evaluated Nuclear Data File (ENDF)*, Brookhaven National Laboratory, http://www.nndc.bnl.gov/exfor/endf00.jsp

“HFIR Safety Analysis Report (SAR),” 2021. ORNL/HFIR/SAR/2344, Rev. 19, Oak Ridge National Laboratory.

“Procedure for Determining the Beginning of Cycle ESCCEP of HFIR Control Plates.” 2021. SBP-1100, Rev. 4.

“SCALE: A Comprehensive Modeling and Simulation Suite for Nuclear Safety Analysis and Design.” 2011. ORNL/TM-2005/39, Version 6.1, Oak Ridge National Laboratory, Oak Ridge, TN. Available from Radiation Safety Information Computational Center at Oak Ridge National Laboratory as CCC-785.

W. Haeck. 2009. *VESTA User’s Manual – Version 2.0.0*, IRSN Report, DSU/SEC/T/2008-331 Indice A, Institut de Radioprotection et de Sûreté Nucléaire (IRSN, The French Institute for Radioprotection and Nuclear Safety), France.

7. ACKNOWLEDGEMENTS

This study was performed and documented to support multiple ORNL efforts and programs, including the Plutonium Supply Project (PSP) seeking to enhance the permanent reflector for increased ^{238}Pu production capabilities, the HFIR-SENSe Initiative seeking to enhance HFIR’s performance and scientific capabilities, and the Research Reactors Divisions (RRD) responsible for safely operating HFIR. The PSP is funded by NASA’s Science Mission Directorate and the U.S. DOE Office of Nuclear Infrastructure Programs. The HFIR-SENSe Initiative is funded by the Laboratory Directed Research and Development Program of ORNL, managed by UT Battelle LLC. RRD is funded by the U.S. DOE Office of Science, Office of Basic Energy Sciences. This paper was authored by UT-Battelle LLC, under contract DE-AC05-00OR22725 with the U.S. DOE. The authors would like to thank Briana Hiscox of ORNL for her comprehensive technical review of this paper and John Batson III of ORNL for his editorial review of this paper.

APPENDIX A. THREE-DIMENSIONAL HEAT DEPOSITION ANALYSES

APPENDIX A. THREE-DIMENSIONAL HEAT DEPOSITION ANALYSES

A-1. INTRODUCTION

Before performing the calculations documented in the body of this report, an iterative study was performed involving MCNP heat deposition calculations and COMSOL Multiphysics FEA thermal-structural calculations to determine the spatial resolution required for the high-fidelity thermal calculations. Initially, 3D (i.e., r-z-θ) heat deposition results were being assessed because the COMSOL calculations were using a 3D geometry and a fine spatial mesh. It was ultimately decided that the 2D (i.e., r-z) heat deposition rates documented in the body of this report were adequate for the thermal calculations because there is not much azimuthal variation in the heat deposition rates in areas of prime importance and because the 2D results were more efficient to calculate and map onto the COMSOL mesh.

A-1. SUPERIMPOSED MESH METHOD

The initial method employed to assess the 3D heat deposition rates implemented a superimposed cylindrical mesh tally and appropriate cross section and heating number tally multipliers to convert the neutron and gamma fluxes into heat deposition rates. This method was tested on the coarse PB reflector seven radial by one axial cell-based mesh model documented by Chandler et al. (2020). The superimposed mesh consisted of seven radial regions, 21 axial regions, and 120 azimuthal regions, for a total of 1,760 mesh cells. This method is straightforward to implement because the Be reflector geometry does not have to be modified. However, the mesh boundaries are defined by radial, axial, and azimuthal surfaces, which results in many mesh cells containing homogenous mixtures of Be reflector and other components (e.g., beam tube Al, beam tube void, VXF liners, VXF plugs, water). The heat deposition rates calculated for these homogeneous mesh cells are based on the flux and material composition of the homogenous mixtures, which is undesirable when calculating heat deposition rates in the Be reflector only.

The first set of MCNP KCODE calculations yielded unsatisfactory statistical uncertainties, so the ADVANTG 3.0.3 code (Mosher 2015) was employed to generate variance reduction parameters to reduce the statistical uncertainties. The KCODE calculation was first converted into a fixed-source calculation based on the EOC fuel element fission distribution from Chandler et al. (2020) to enable the use of ADVANTG. Then, ADVANTG was executed to generate the energy and spatially dependent biases and weight windows data to be used in the prompt MCNP heat deposition rate calculation to calculate the neutron and prompt plus capture gamma heat deposition rates. ADVANTG and MCNP were also used to analyze the delayed gamma heat deposition rates. Figure A-1 provides the EOC θ-z heat deposition rate distribution for the innermost radial region of the PB reflector. This figure illustrates how the heat deposition rates are calculated around the four horizontal beam tubes, which consider homogenous mixtures as previously discussed.

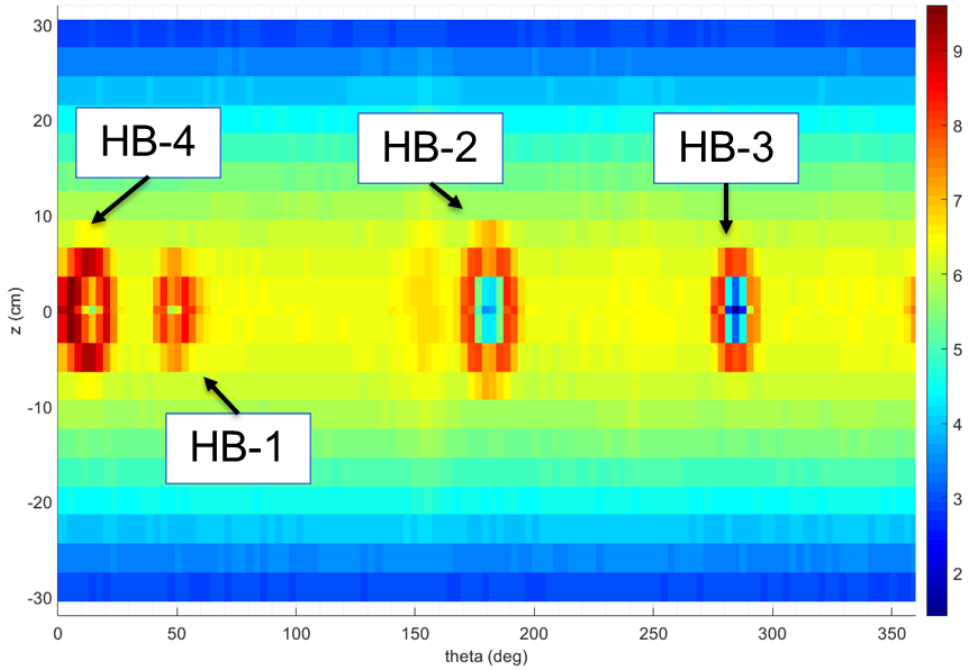

Figure A-1. Heat deposition rate (W/cm^3) distribution in first radial ring using the superimposed mesh method.

A-2. CELL BASED METHOD

Ultimately, the best way to calculate 3D heat deposition rates in the Be reflector was determined to explicitly subdivide the reflector into the desired r-z cell mesh and then use the tally segment card (i.e., FS card) to subdivide each r-z ring into the desired number of azimuthal tally regions. For this study, the tallied mesh consisted of 12 radial regions (i.e., one less radial region than modeled in the body of this report), 21 axial regions, and 120 azimuthal regions. Thus, 252 permanent reflector geometry cells were explicitly modeled, and 30,240 total regions were tallied. Alternatively, 30,240 geometry cells could have been explicitly modeled. ADVANTG was once again utilized to generate variance reduction parameters crucial to calculating satisfactory statistics on such a fine mesh with the MCNP EOC prompt and delayed fixed source inputs.

The 3D heat deposition rate distribution in the permanent reflector concept design with Be plugs in all VXFs is provided in Figure A-2 and the x-y distribution on the core horizontal midplane is illustrated in Figure A-3. A peak local heat deposition rate of about 7.5 W/cm^3 was calculated, which is in good agreement with the peak values reported in Section 4.2.2 of this report. To illustrate the azimuthal variation in the results, the local r-z-θ values were compared to their r-z ring averaged values. The local-to-ring average ratio results on the core midplane are illustrated in Figure A-4, which indicates that the largest ratios exist on the back side of the three tangential horizontal beam tubes. The local heat deposition rates on the back side of these beam tubes are greater than the ring-averaged results because neutrons and gammas are not well shielded through the beam tubes.

Figure A-5, Figure A-6, and Figure A-7 illustrate the local to ring-averaged results for the concept reflector with Be plugs, water/SST liners, and EOC ^{238}Pu production targets in the VXFs, respectively. The ^{238}Pu production target geometry and material data were obtained from a study by Chandler et al. (2019). For each of the three cases, plots on the core horizontal midplane and the core exit plane (i.e., axial bottom of reflector) are provided. Much more azimuthal variation is observed on the core midplane because of the influence of the horizontal beam tubes. Additionally, more azimuthal variation is observed for the ^{238}Pu production case because of the impact of the target pellet materials (e.g., ^{237}Np, ^{238}Np, ^{238}Pu, ^{239}Pu) that both absorb and emit neutrons and gamma rays.

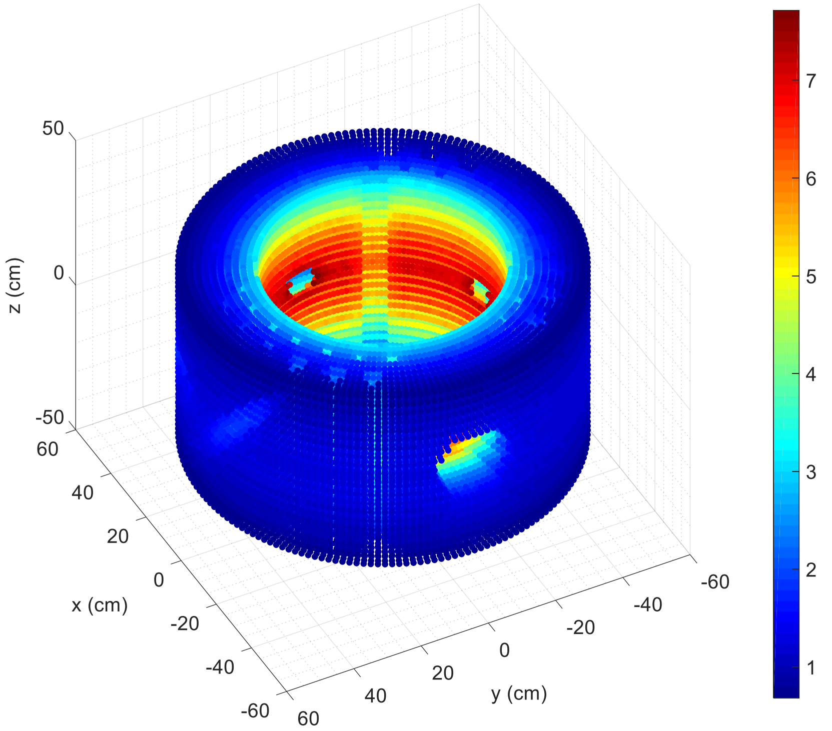

Figure A-2. 3D heat deposition rate (W/cm^3) for concept design with Be plugs in VXFs.

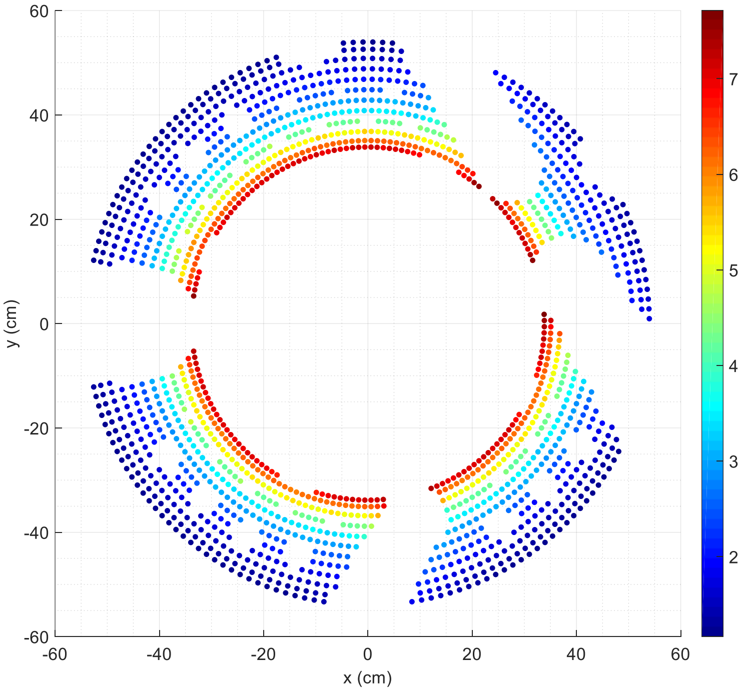

Figure A-3. Core midplane heat deposition rate (W/cm^3) for concept design with Be plugs in VXFs.

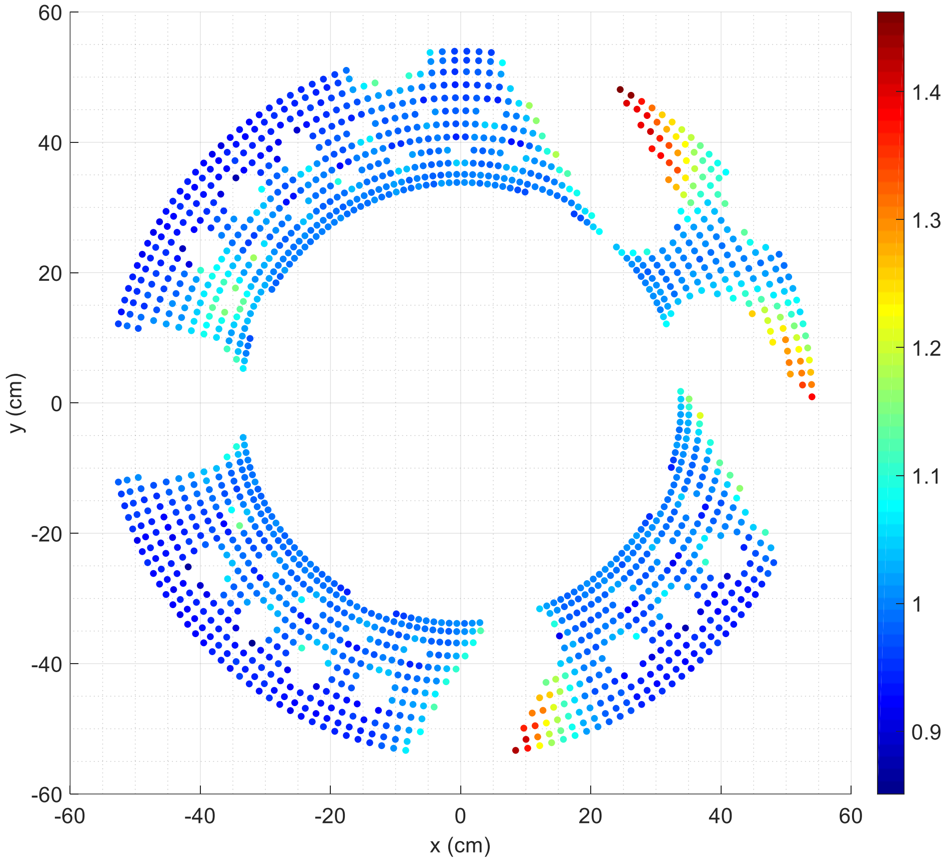

Figure A-4. Core midplane local-to-r-z ring average heat deposition rate ratio distribution for concept reflector with Be plugs.

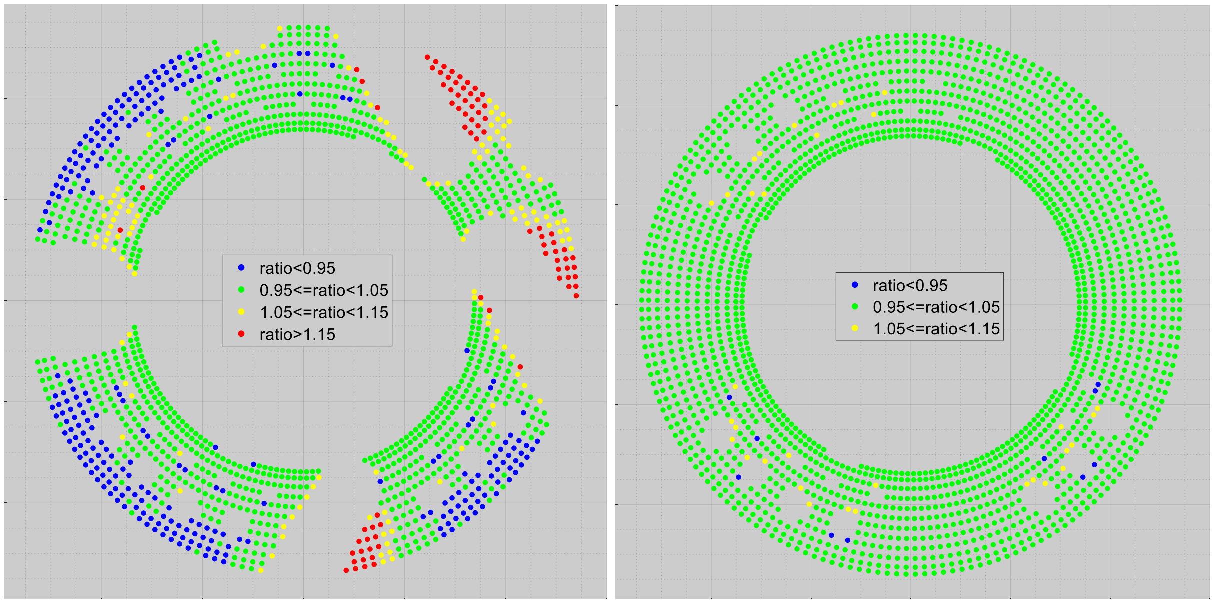

Figure A-5. Local-to-r-z ring average heat deposition rate ratio distribution for case with Be plugs in VXFs on core horizontal midplane (left) and core exit plane (right).

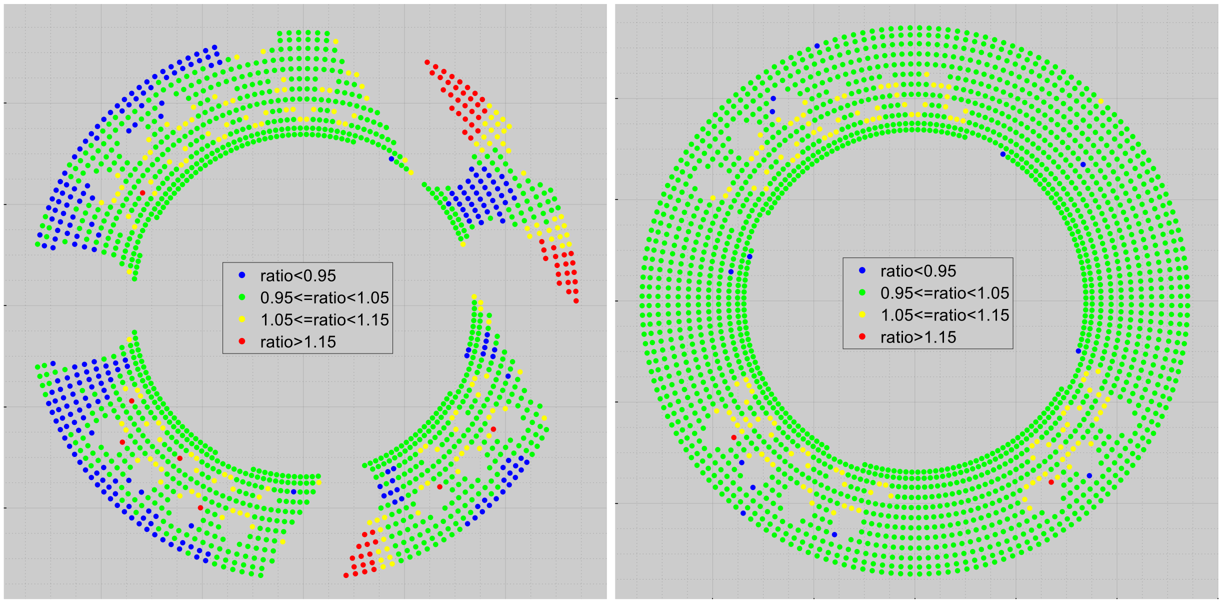

Figure A-6. Local-to-r-z ring average heat deposition rate ratio distribution for case with water/SST in VXFs on core horizontal midplane (left) and core exit plane (right).

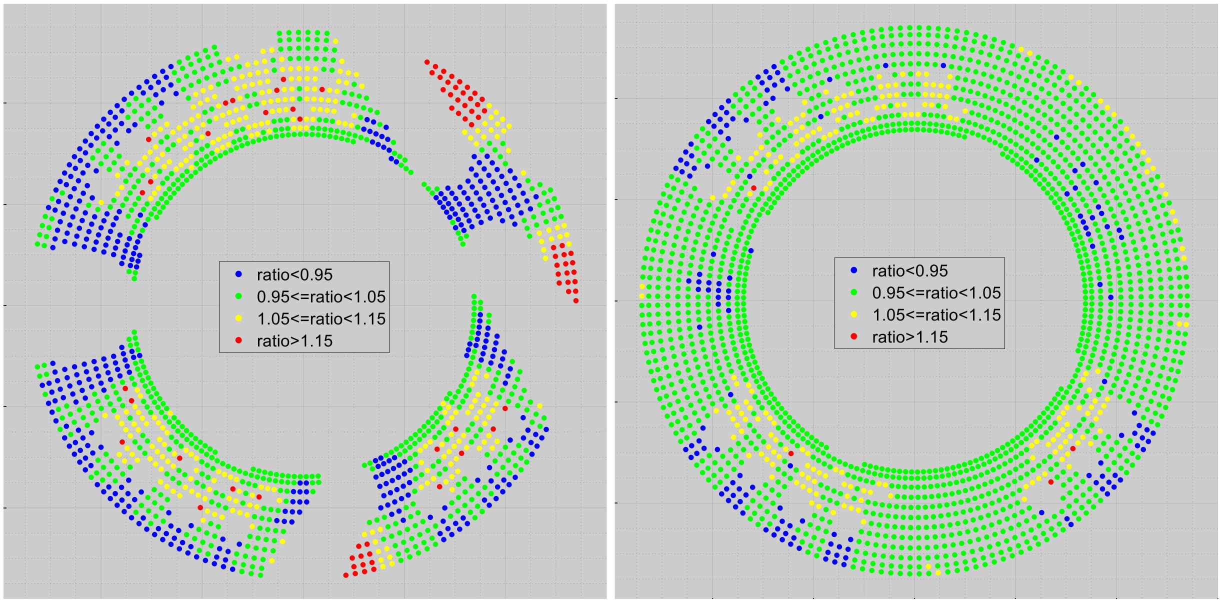

Figure A-7. Local-to-r-z ring average heat deposition rate ratio distribution for case with ^{238}Pu production targets in VXFs on core horizontal midplane (left) and core exit plane (right).